

FABRICATION AND INVESTIGATION OF EXTREMELY THIN CdTe  
ABSORBER LAYER SOLAR CELLS

A THESIS SUBMITTED TO  
THE GRADUATE SCHOOL OF NATURAL AND APPLIED SCIENCES  
OF  
MIDDLE EAST TECHNICAL UNIVERSITY

BY

AREZOO HOSSEINI

IN PARTIAL FULFILLMENT OF THE REQUIREMENTS  
FOR  
THE DEGREE OF DOCTOR OF PHILOSOPHY  
IN  
PHYSICS

FEBRUARY 2016





Approval of the Thesis:

**FABRICATION AND INVESTIGATION OF EXTREMELY THIN CdTe  
ABSORBER LAYER SOLAR CELLS**

submitted by **AREZOO HOSSEINI** in partial fulfillment of the requirements for the degree of **Doctor of Philosophy in Physics Department, Middle East Technical University** by,

Prof. Dr. Gülbin Dural Ünver  
Dean, Graduate School of **Natural and Applied Sciences**

\_\_\_\_\_

Prof. Dr. Mehmet T. Zeyrek  
Head of Department, **Physics**

\_\_\_\_\_

Prof. Dr. Çiğdem Erçelebi  
Supervisor, **Physics Dept., METU**

\_\_\_\_\_

Prof. Dr. Raşit Turan  
Co-Supervisor, **Physics Dept., METU**

\_\_\_\_\_

**Examining Committee Members:**

Prof. Dr. Macit Ahmet Özenbaş  
Metallurgical and Materials Eng. Dept., METU

\_\_\_\_\_

Prof. Dr. Çiğdem Erçelebi  
Physics Dept., METU

\_\_\_\_\_

Prof. Dr. Mehmet Parlak  
Physics Dept., METU

\_\_\_\_\_

Assoc. Prof. Dr. Nurdan Demirci Sankir  
Materials Science and Nanotechnology Eng. Dept., TOBB ETÜ

\_\_\_\_\_

Assoc. Prof. Dr. Savaş Sönmezoğlu  
Metallurgical and Materials Eng. Dept., KMU

\_\_\_\_\_

**Date: 05.02.2016**

**I hereby declare that all information in this document has been obtained and presented in accordance with academic rules and ethical conduct. I also declare that, as required by these rules and conduct, I have fully cited and referenced all material and results that are not original to this work.**

Name, Lastname: Arezoo HOSSEINI  
Signature :

## ABSTRACT

### FABRICATION AND INVESTIGATION OF EXTREMELY THIN CdTe ABSORBER LAYER SOLAR CELLS

Hosseini, Arezoo

Ph.D., Department of Physics

Supervisor: Prof. Dr. Çiğdem Erçelebi

Co-Supervisor: Prof. Dr. Raşit Turan

February 2016, 130 pages

Extremely thin absorber layer (ETA) solar cells aim to combine the advantages of using very thin and cheaply produced absorber layer on nano structured substrates with stability of all-solid-state solar cells. This type of photovoltaic devices use a nano structured interpenetrating heterojunction of thin light-absorbing layer at the interface between an n- and p-type semiconductors. N-type nano structured TiO<sub>2</sub> layer is deposited on a Transparent Conducting Oxide coated glass (TCO) substrate, following with the CdTe thin absorber layer deposition to cover the structured wide band gap semiconductor. Finally a void-filling ZnSnTe, optically transparent semiconductor, is deposited onto the absorber layer. This structure is followed by a metallic layer deposition to fulfill the ETA solar cell structure. These types of solar cells with nano structured n-type material and thin CdTe absorber layer have a higher absorption rate of light as compared to flat ones. The thickness of the absorber layer is an important parameter for both device operation and the ultimate cost of energy production of these structures. The aim of this thesis study is to investigate the fabrication and performance of different solar cell structures with extremely thin CdTe absorber layer.

In this study, a variety of nano structured TiO<sub>2</sub> layers were produced by different techniques and characterized as the n-type material for both two- and three-component ETA solar cells. The spin coated nano-porous, hydrothermally grown nanowire and electrochemically anodized nanotube TiO<sub>2</sub> layers were used as the substrate for sputtered and electrodeposited CdTe layer. It was observed that the sputtered TiO<sub>2</sub> layer should be present prior to the nanoporous TiO<sub>2</sub> layer formation in order to prevent the shorting between FTO and CdTe layers. Also, ZnTe layer was investigated as the p-type layer for three-component ETA solar cells but due to the high resistance value of this material, ZnTe was substituted with low resistance ZnSnTe layer.

Various novel two- and three-component ETA solar cells based on different nano structured TiO<sub>2</sub> with CdTe and ZnSnTe thin film layer deposited by sputtering and electrodeposition methods, were fabricated in the laboratory scale and characterized. The best efficiency and the device parameters were obtained for the two-component Glass/FTO/NWAs TiO<sub>2</sub>/Electrodeposited CdTe/ Cu-Au structure.

Both CdCl<sub>2</sub> surface treatment and post annealing of the CdTe surface, which were applied prior to the formation of the complete solar cell structure, are found to be essential for the efficiency improvement. The use of nano structured TiO<sub>2</sub> is also an important factor, which improves the light trapping in this structure. Also the use of electrodeposited CdTe absorber layer, which fills the pores of nano structured TiO<sub>2</sub> substrates, improves the efficiency when compared to the solar cell structure with the sputtered CdTe thin film layer.

**Keywords:** ETA, Solar Cell, Nanostructure, TiO<sub>2</sub>, Light Tapping, CdTe, ZnSnTe, Sputtering, Electrodeposition

## ÖZ

### ÇOK İNCE CdTe SOĞURUCU TABAKALI GÜNEŞ HÜCRELERİNİN ÜRETİMİ VE İNCELENMESİ

Hosseini, Arezoo

Doktora, Fizik Bölümü

Tez Yöneticisi: Prof. Dr. Çiğdem Erçelebi

Ortak Tez Yöneticisi: Prof. Dr. Raşit Turan

Şubat 2016, 130 sayfa

Çok ince emici tabakaya sahip güneş hücrelerinin amacı katı hal güneş hücrelerinde sağlanan kararlılık ile çok ince ve düşük maliyete sahip emici tabakanın nano-yapılandırılmış alüminyum oksit üzerinde kullanım avantajının bir araya getirilmesidir. Bu tip fotovoltaik aygıtlarda çok ince emici tabaka, n-tipi ve p-tipi iki yarı iletken arasında kullanılır. Bu yapıda, n-tipi nano-yapılandırılmış  $TiO_2$  katmanı, TCO kaplanmış cam alüminyum oksit üzerinde elde edilir ve ardından, CdTe ince emici tabaka, nano-yapılandırılmış geniş bant yapısına sahip bu yarıiletken tabaka üzerine kaplanır. Son olarak, boşlukları doldurabilen ZnSnTe geçirgen yarıiletken ince film, soğurucu tabaka üzerine kaplanır. ETA güneş hücresi yapısının tamamlanması için iletken metal kontak son katman olarak kullanılır. Nano-yapılandırılmış n-tipi ince film ve çok ince CdTe emici tabakaya sahip bu tip güneş hücreleri, düz yapılarla karşılaştırıldığında daha yüksek ışık soğurma oranına sahiptir. Emici tabakanın kalınlığı hem aygıtın verimli çalışması hem de nihai enerji üretim maliyeti açısından önemlidir. Tez çalışmasının amacı, çok ince CdTe emici tabakaya sahip güneş hücresi yapılarının üretimi ve performansının araştırılmasıdır.

Bu tez çalışmasında ikili ve üçlü ETA güneş hücreleri için, farklı nanoyapılı  $TiO_2$  tabakalar n-tipi materyal olarak üretilip karakterize edilmiştir. Spin kaplama yöntemi ile nano yapılı-gözenekli, hidrotermik yöntem ile nanotel, elektrokimyasal yöntem ile nanoçubuk yapılarında TCO kaplı cam tabanlar üzerine elde edilen  $TiO_2$  ince film tabakaları; saçtırma ve elektrokaplama yöntemleriyle üretilen CdTe ince film tabakaları için tutucu taban olarak kullanılmıştır. Spin kaplama öncesinde, saçtırma yöntemi ile kaplanan  $TiO_2$  tabakasının oluşturulmasının, FTO ve CdTe tabakaları arasında kısa devre yollarının oluşmasını engellediği gözlenmiştir. Ayrıca ZnTe tabakası ETA yapılarında p-tipi pencere tabakası olarak araştırılmış ancak direnç değerinin yüksek olmasından dolayı, aygıt üretiminde düşük direnç değerine sahip olan ZnSnTe ince film tabakası kullanılmıştır.

Saçtırma ve elektrokaplama yöntemiyle büyütülmüş CdTe ince film tabakaları, farklı nano yapılı  $TiO_2$  ve ZnSnTe tabakaları kullanılarak, çeşitli ikili ve üçlü katmanlı ETA güneş hücreleri laboratuvar ölçeğinde üretilerek incelenmiştir. Cam/FTO/nanorod  $TiO_2$ /elektrokaplama CdTe/Bakır-Altın yapısındaki aygıtlar en iyi verimlilik ve aygıt parametrelerine sahip olan ETA güneş pili yapıları olarak gözlenmiştir.

Güneş pili yapılarının tamamlanması öncesinde, CdTe ince film yüzeyine  $CdCl_2$  ve değişik sıcaklıklarda ve sürelerde tavlama işlemleri uygulanmasının verimin artması için gerekli olduğu sonucuna ulaşılmıştır. Nanoyapılı  $TiO_2$  tabakasının kullanılması soğurulan ışığın yapıda daha fazla hapsedilmesini sağlaması açısından önemlidir. Bununla birlikte, elektrokaplama yöntemiyle kaplanan CdTe ince film emici tabakanın, saçtırma yöntemi ile kaplanan CdTe ince film tabakasına göre nanoyapılı  $TiO_2$  ince film tabakasındaki gözenekleri daha fazla doldurarak verimin artmasına katkıda bulunduğu gözlenmiştir.

**Anahtar kelimeler:** ETA, Güneş Pili, Nanoyapı,  $TiO_2$ , Işığı Hapsetme, CdTe, ZnSnTe, Saçtırma Yöntemi, Elektrokaplama

To my family

## ACKNOWLEDGMENTS

First of all, I wish to express my sincerest gratitude to Prof. Dr. Çiğdem Erçelebi for her kind supervision, invaluable support, friendship and behaving like a mother during my study. I would like to thank Prof. Dr. Raşit Turan for giving me the opportunity to have him as my co-advisor for this research and giving me the opportunity to be a member of GÜNAM family. My sincere thanks belongs to Prof. Dr. Mehmet Parlak for his continuous encouragement and guidance throughout this research. I would like to thank Prof. Dr. Macit Özenbaş for giving me the opportunity to work in his lab for fabrication of porous TiO<sub>2</sub> film and all the guidance in this period. I am highly thankful to Dr. Selcuk Yerci for all his support during this research. Without their humor, positive attitude, this research would be tough. I will never forget your efforts and support.

I would like to express my appreciation to Dr. Karthik Shankar as my advisor in Alberta University, Canada for valuable comments and suggestions throughout the study by spending several hours to discuss all aspect of this structure. I would like to thank Dr. Piyush Kar as my co-advisor for all his helps and efforts regarding CdTe fabrication by electrodeposition method.

I attribute my PhD degree to all my mentioned tutors. Your helps will never be forgotten.

It is a great pleasure for me to offer sincere thanks to all people helping me during this research.

I would like to express my warm thanks to my colleague Hasan Hüseyin Güllü a brother here, I cannot describe his helps during this research. I owe him so many things. I am grateful to thank Seda Kayra Güllü and Özge Bayraklı and Emre Coskun for their presence as my close friends and pieces of productive discussions. Thanks to my good friends.



I wish to express my deep thanks to Zeynep Demirciođlu for her patience and kindness for the time she invested to format my thesis, It was really hard for me without her help.

I would like to extend my thanks to my friend, Cagatay Icli for training me the synthesis process of nanoporous TiO<sub>2</sub> layer and also providing me the solution demanded for spin coating process. I would also like to acknowledge my colleague Mehmet Koc for having shared with me his knowledge about the solar cell simulations.

GÜNAM would be a monotonous research center without my dear friends and colleagues; Hande Çiftınar, Hisham Nasser, Firat Es, Engin Özkol, Yasin Ergunt, Olgu Demirciođlu, Yusuf Kasap, Gülsen Baytemir, Emel Semiz, Mehmet Karaman, Idris Candan, Mustafa Ünal, Salar Habibpur Sedani, Gamze Kökbudak, Merve Pınar Kabukcuođlu, Wiria Soltanpoor, Mehmet Cem Sahiner and Makbule Terlemezođlu.

I have been blessed with a helpful group of friends in Alberta University. Special thanks to Abdelrahman Askar, Mourad Benlamri, Ahmad Adl, Yun Zhang, Najia Mahdi and Advaita Bhatnagar. My Special thanks to Arash Mohammadpour for his assistance in collecting I-V measurement datas, one of the most important steps in this study. I would also like to extend my great appreciation to Benjamin Wiltshire for training and providing me the Nanowire samples. My great thanks goes to Samira Farsinezhad for all assistance during the period I stayed in Canada, like a sister. Thank you so much for having such an incredible influence in my life.

I am grateful to GÜNAM Secretery; Yücel Eke, Nevzat Görmez, Tayfun Yıldız, Dursun Erdoğan for technical support and also to Harun Tanık, Tuncay Güngör and Buket Gökbakan for their support in administrative issues in GÜNAM.

My deep thanks goes to Eser Ünsaldı, Sanam Dehgan, Sara Razzagi, Mona Zolfaghari Borra, Saeede Shamei, Vessal Rasoulzadeh, Shirin Sepehri, Marjan Golbandi, Pantea Aurang and Shole Alaie for having shared with me many nice moments of the last years.

The financial support from the Scientific and Technological Research Council of Turkey (TUBITAK BİDEB-2215), natural Sciences and Engineering Research Council of Canada (NSERC) and Canadian Microelectronics Corporation (CMC) are highly acknowledged.

I am grateful to all members of my great family: my parents, my brother and my sisters for their continual encouragement and support in every stage of the entire of my life. I really thank my father Hassan and mother Kobra for their unconditional love, understanding, endless support and encouragement during my 'long student' life, "I love you". I owe a debt gratitude to my brother and his wife for all their helps. My special loves go to Sam my nephew, who is a piece of my heart. Thanks to my new family, it is great honor for me to be a part of your lovely family.

Finally, I want to dedicate my sincerest gratitude to my husband, the love of my life, Navid for his continual love and support. It would not be possible for me to achieve this goal without his patience, understanding and unconditional support.

## TABLE OF CONTENTS

ABSTRACT.....	v
ÖZ.....	vii
ACKNOWLEDGMENTS.....	x
TABLE OF CONTENTS.....	xiii
LIST OF TABLES.....	xvi
LIST OF FIGURES.....	xvii
NOMENCLATURE.....	xxii
CHAPTERS	
1 EXTREMELY THIN ABSORBER LAYER (ETA) SOLAR CELLS.....	1
1.1 Introduction.....	1
1.2 Photovoltaic Devices: Solar Cells.....	2
1.2.1 First Generation Solar Cells.....	3
1.2.2 Second Generation Solar Cells.....	4
1.2.3 Third Generation Solar Cells.....	5
1.2.3.1 The Dye-Sensitized Solar Cells (DSSC).....	6
1.2.3.2 Organic Solar Cells.....	7
1.3 Extremely Thin Absorber Layer (ETA) Solar Cells.....	8
1.3.1 General Information.....	8
1.3.2 Literature Survey.....	10
1.3.3 ETA Solar Cell P-I-N Model.....	12
1.3.3.1 Physical Description.....	12
1.3.3.2 Mathematical Modelling.....	14
1.4 Extremely Thin CdTe Absorber Layer Solar Cell Structures Investigated in the Thesis.....	20
1.4.1 Studied ETA Solar Cell Structures.....	20
1.4.2 Titanium Dioxide (TiO <sub>2</sub> ).....	23
1.4.3 Cadmium Telluride (CdTe), Zinc Tin Telluride (ZnSnTe).....	24
1.4.4 Outline of the Thesis Presentation.....	25

1.5	References.....	27
2	EXPERIMENTAL .....	33
2.1	General Description of Experimental Methods .....	33
2.2	Deposition Methods.....	34
2.2.1	Sol-Gel Method.....	34
2.2.2	Physical Vapor Deposition .....	35
2.2.3	Electrodeposition and Electrochemical Anodization Methods.....	35
2.2.4	Hydrothermal Method.....	37
2.3	Sample Preparation .....	38
2.3.1	Substrate Cleaning .....	38
2.3.2	TiO <sub>2</sub> Thin Film Deposition .....	39
2.3.2.1	Sputtered TiO <sub>2</sub> Thin Film.....	39
2.3.2.2	Spin Coated TiO <sub>2</sub> Thin Films .....	40
2.3.2.3	Electrochemical Anodization of TiO <sub>2</sub> Nanotube Arrays.....	41
2.3.2.4	Hydrothermal Growth of TiO <sub>2</sub> Nanowire Arrays .....	41
2.3.3	CdTe Thin Film Deposition .....	42
2.3.3.1	Sputtered CdTe .....	42
2.3.3.2	Electrodeposited CdTe.....	43
2.3.4	ZnTe and ZnSnTe Thin Film Deposition .....	44
2.4	General Description of the Characterization Methods .....	45
2.4.1	UV-Vis Spectroscopy .....	45
2.4.2	X-ray Diffraction .....	49
2.4.3	Atomic Force Microscopy .....	52
2.4.4	Scanning Electron Microscopy and Energy Dispersive Spectroscopy ...	54
2.4.5	Surface Profilometer .....	57
2.4.6	Electrical Measurements.....	57
2.4.6.1	The Metallic Evaporation System.....	57
2.4.6.2	Conductivity Measurements .....	58
2.4.6.3	Current- Voltage (I-V) Measurements.....	59
2.5	References.....	63
3	MATERIAL CHARACTERIZATION.....	67
3.1	Characterization of n-Type TiO <sub>2</sub> Layer .....	67

3.1.1	Sputtered TiO <sub>2</sub> Thin Film.....	67
3.1.1.1	Structural and Morphological Properties.....	67
3.1.1.2	Optical Properties .....	70
3.1.2	Spin Coated TiO <sub>2</sub> Films.....	72
3.1.2.1	Structural and Morphological Properties.....	72
3.1.2.2	Optical Properties .....	78
3.1.3	Electrochemically Anodized TiO <sub>2</sub> Nanotube Arrays (NTAs).....	80
3.1.3.1	Structural and Morphological Properties.....	80
3.1.3.2	Optical Properties .....	82
3.1.4	Hydrothermally Grown TiO <sub>2</sub> Nanowires .....	84
3.1.4.1	Structural, Morphological and Optical Properties.....	84
3.2	Characterization of CdTe Thin Film Absorber Layer.....	86
3.2.1	Sputtered CdTe Thin Film.....	86
3.2.1.1	Structural and Morphological Properties.....	86
3.2.1.2	Optical Properties .....	89
3.2.2	Structural, Morphological and Optical Properties of Electrodeposited CdTe Layer .....	91
3.3	Characterization of p-Type ZnTe and ZnSnTe Layers .....	95
3.3.1	Structural and Morphological Properties.....	95
3.3.2	Optical Properties .....	98
3.4	Conclusion.....	102
3.5	References .....	103
4	DEVICE CHARACTERIZATION AND FUTURE WORK.....	105
4.1	ETA Solar Cell Characterization.....	105
4.1.1	Devices with Sputtered CdTe Absorber Layer.....	105
4.1.2	Devices with Electrodeposited CdTe Layer.....	111
4.2	Structural, Morphological and Optical Characterizations of NWAs TiO <sub>2</sub> /Electrodeposited CdTe Junction .....	115
4.3	Future Work .....	119
4.4	References .....	122
5	CONCLUSIONS.....	123
	CURRICULUM VITAE.....	127

## LIST OF TABLES

### TABLES

Table 1. 1 The band gap energy, electron affinity and work function values of different layers of ETA cell structures studied in this work.....	21
Table 2. 1 The deposition parameters of sputtered TiO <sub>2</sub> thin films .....	39
Table 2. 2 The deposition parameters of spin coated TiO <sub>2</sub> thin films.....	40
Table 2. 3 The deposition parameters of the sputtered CdTe thin films .....	42
Table 2. 4 The ED parameters of CdTe thin films .....	44
Table 2. 5 Thickness values of ZnTe and SnTe (in the ZnSnTe) thin films .....	45
Table 3. 1 The roughness values of the coated films and glass substrate .....	76
Table 3. 2 Zn:Sn:Te ratios and resistance values of different ZnSnTe samples .....	97

## LIST OF FIGURES

### FIGURES

Figure 1. 1 Photovoltaic effect in a p-n junction solar cell .....	3
Figure 1. 2 The Schematic of CdS/CdTe thin-film solar cells .....	5
Figure 1. 3 (a) The schematic illustration of dye-sensitized solar cells (Hagfeldt, et al., 2010), (b) Working principle of a typical DSC employing an iodide/triiodide-based redox electrolyte and N719 as a sensitizer (Grätzel, 2009) .....	6
Figure 1. 4 (a) The schematic and (b) Idealized Band diagram of an ETA solar cell .	9
Figure 1. 5 Light trapping in the ETA cell.....	10
Figure 1. 6 Interfacial recombination processes (shown as red arrows) in an ETA cell.....	13
Figure 1. 7 Energy band diagram for ETA solar cell.....	15
Figure 1. 8 Energy levels of different materials employed for (a) FTO/TiO <sub>2</sub> /CdTe/Au (b) FTO/TiO <sub>2</sub> /CdTe/ZnSnTe/In devices .....	22
Figure 1. 9 Bulk unit cell of rutile (left) and anatase (right). Oxygen atoms are red coloured and titanium atoms are grey coloured.....	23
Figure 2. 1 The schematic of the two-electrode electrodeposition set up.....	37
Figure 2. 2 Various absorption processes in the semiconductors: (1) Band to band, (2) Interconduction band, (3) Intervalence band, (4) Donor to conduction band, (5) Acceptor to valance band, (6) Valance band to donor, (7) Acceptor to conduction band, and (8) Donor to acceptor transitions.....	46
Figure 2. 3 Illustration of (a) Direct band gap, and (b) Indirect band gap transitions.....	47
Figure 2. 4 Bragg diffraction of X-rays from parallel planes .....	51
Figure 2. 5 The schematic of the XRD system .....	52

Figure 2. 6 SEM images of AFM probe a) With Pyramidal probe b) With Conical high aspect ratio probe .....	53
Figure 2. 7 The schematic of an AFM setup .....	53
Figure 2. 8 The schematic of a typical Scanning Electron Microscope .....	56
Figure 2. 9 The schematic of the metal contact evaporation system.....	58
Figure 2. 10 The schematic of the current-voltage measurement setup .....	60
Figure 2. 11 The typical current-voltage variation of a solar cell in dark and under illumination .....	60
Figure 3. 1 XRD patterns of the sputtered TiO <sub>2</sub> films with different RF Powers .....	68
Figure 3. 2 SEM micrographs of one deposition run time sputtered TiO <sub>2</sub> film (P=120W) .....	68
Figure 3. 3 SEM micrographs of two deposition run time sputtered TiO <sub>2</sub> film (P=120W) .....	69
Figure 3. 4 AFM image of one deposition run time sputtered TiO <sub>2</sub> film (P=120W) .....	69
Figure 3. 5 (a) Transmittance spectra (b) Tauc plot of sputtered TiO <sub>2</sub> film.....	71
Figure 3. 6 XRD patterns of the TiO <sub>2</sub> powder, peak indicated by * is due to rutile phase.....	72
Figure 3. 7 XRD patterns of spin coated TiO <sub>2</sub> films deposited with the spin coating speeds of 2000, 5000 and (2000-5000) rpm.....	73
Figure 3. 8 XRD patterns of the one and two run deposition time spin coated TiO <sub>2</sub> films for different annealing environments and annealing temperatures .....	73
Figure 3. 9 SEM micrographs of spin coated TiO <sub>2</sub> films deposited with the spin coating speeds of (1) 2000, (2) 5000 and (3) (2000-5000) rpm .....	75
Figure 3. 10 AFM images of spin coated TiO <sub>2</sub> films deposited with the spin coating speeds of (1) 2000, (2) 5000 and (3) (2000-5000) rpm.....	77
Figure 3. 11 (a) Comparative transmittance spectra and (b) Tauc plot of spin coated TiO <sub>2</sub> films with one and two successive different spin rates.....	79



Figure 3. 12 (a) XRD pattern (b) SEM image of the TiO <sub>2</sub> NTAs.....	81
Figure 3. 13 (a) Transmittance spectrum and (b) Tauc plot of the TiO <sub>2</sub> NTAs.....	83
Figure 3. 14 (a) XRD pattern (b) and (c) SEM images (d) Tauc plot of NWAs .....	85
Figure 3. 15 XRD patterns of the sputtered CdTe films deposited with different substrate/annealing temperatures and deposition time (RF=70 W).....	87
Figure 3. 16 SEM images of the sputtered CdTe film (RF=70 W, t=60 min, T <sub>s</sub> =300 °C, T <sub>a</sub> =350 °C).....	88
Figure 3. 17 AFM image of the sputtered CdTe film (RF=70 W, t=60 min, T <sub>s</sub> =300 °C, T <sub>a</sub> =350 °C).....	88
Figure 3. 18 (a) Absorption and (b) Transmittance spectra of the sputtered CdTe thin films .....	90
Figure 3. 19 Tauc plot of the sputtered CdTe film (RF=70 W, t=60 min, T <sub>s</sub> =300 °C, T <sub>a</sub> =350 °C) .....	91
Figure 3. 20 XRD patterns of the CdTe films deposited on FTO coated glass substrates prepare with (a) Three-electrode (b) Two-electrode method.....	93
Figure 3. 21 (a) SEM image (b) Transmittance (c) Photoluminescence of CdTe film deposited on FTO coated glass substrates prepared with two-electrode method .....	94
Figure 3. 22 XRD patterns of the ZnTe films.....	95
Figure 3. 23 XRD patterns of the ZnSnTe films.....	96
Figure 3. 24 SEM micrographs of sputtered ZnTe films (a) as-grown (T <sub>s</sub> =300 °C) (b) annealed (T <sub>s</sub> =300 °C annealed at T <sub>a</sub> =350 °C).....	97
Figure 3. 25 SEM images of the ZnSnTe film a) as-grown and b) annealed for 5 minutes c) annealed for 30 minutes .....	98
Figure 3. 26 Transmittance spectra, absorption spectra and Tauc plot of sputtered ZnTe films.....	99
Figure 3. 27 (a) Transmittance spectra (b) Absorption spectra and (c) Reflection spectrum and Tauc plot of sputtered ZnSnTe films.....	100
Figure 3. 28 Tauc plots of sputtered ZnSnTe films .....	101

Figure 4. 1 J–V characteristics of Glass/FTO/TiO <sub>2</sub> /Sputtered CdTe/Au devices with (a) Sputtered TiO <sub>2</sub> (b) Spin coated TiO <sub>2</sub> at 5000 rpm spin rate (c) Spin coated TiO <sub>2</sub> at successive spin rates of 2000-5000 rpm.....	107
Figure 4. 2 J–V characteristics of Glass/FTO/TiO <sub>2</sub> /Sputtered CdTe/ZnSnTe/In devices with (a) Spin coated TiO <sub>2</sub> at successive spin rates of 2000-5000 rpm (b) Sputtered TiO <sub>2</sub> +spin coated TiO <sub>2</sub> at successive spin rates of 2000-5000 rpm...	108
Figure 4. 3 J–V characteristics of Glass/FTO/TiO <sub>2</sub> /Sputtered CdTe/Au devices with (a) Sputtered TiO <sub>2</sub> +spin coated TiO <sub>2</sub> at successive spin rates of 2000-5000 rpm (b) NTAs of TiO <sub>2</sub> (c) NWAs of TiO <sub>2</sub> .....	109
Figure 4. 4 J–V characteristics of Glass/FTO/TiO <sub>2</sub> /Sputtered CdTe/ZnSnTe/In devices with (a) Sputtered TiO <sub>2</sub> +spin coated TiO <sub>2</sub> at successive spin rates of 2000- 5000 rpm (b) NTAs of TiO <sub>2</sub> (c) NWAs of TiO <sub>2</sub> .....	110
Figure 4. 5 J–V characteristics of (a) FTO/NTAs of TiO <sub>2</sub> /Electrodeposited CdTe/Cu-Au (b) FTO/ NWAs of TiO <sub>2</sub> /Electrodeposited CdTe/Cu-Au solar cells annealed at 350 °C for 45 minutes.....	112
Figure 4. 6 J–V characteristics of FTO/ NWAs of TiO <sub>2</sub> /Electrodeposited CdTe/Cu- Au solar cell annealed at 350 °C for 15 minutes, followed by annealing at 400 °C for 15 minutes.....	113
Figure 4. 7 Dark and illuminated J–V characteristics of FTO/NWAs of TiO <sub>2</sub> /Electrodeposited CdTe/Cu-Au solar cell annealed at 350 °C for 60 minutes followed by annealing at 400 °C for 30 minutes.....	114
Figure 4. 8 SEM images of the (a),(b) Cross-sectional view of NWAs of TiO <sub>2</sub> /Electrodeposited CdTe solar cell (c), (d) Top images of NWAs of TiO <sub>2</sub> /Electrodeposited CdTe solar cell.....	116
Figure 4. 9 XRD pattern for electrodeposited CdTe on NWAs of TiO <sub>2</sub> .....	117
Figure 4. 10 (a) Transmittance spectra (b) Room temperature PL curves for FTO/Electrodeposited CdTe and FTO/NWAs TiO <sub>2</sub> /Electrodeposited CdTe structures.....	118
Figure 4. 11 Short circuit values versus CdTe layer thickness obtained using simulation of Glass/FTO/NWAs TiO <sub>2</sub> /Electrodeposited CdTe/ Au structure .....	119

Figure 4. 12 Absorption profile in Glass/FTO/NWAs TiO<sub>2</sub>/Electrodeposited CdTe/Au structure as a function of  $\lambda$  for 300-900 nm..... 121

## NOMENCLATURE

PV	Photovoltaic
ETA	Extremely Thin Absorber
C-Si	Monocrystalline Silicon
DSSC	Dye Sensitized Solar Cell
CdTe	Cadmium Telluride
CIS	Copper Indium Diselenide
CIGS	Copper Indium Gallium Diselenide
TiO <sub>2</sub>	Titanium Dioxide
ED	Electrodeposition
TCO	Transparent Conductive Oxide
FTO	Flourine Doped Tin Oxide
Pt	Platinum
Cu	Copper
I <sub>sc</sub>	Short Circuit Current
J	Current Density
J <sub>sc</sub>	Short Circuit Current Density
V <sub>oc</sub>	Open Circuit Voltage
EG	Ethylene Glycol
SEM	Scanning Electron Microscopy
AFM	Atomic Force Microscopy
XRD	X-ray Diffraction
FF	Fill Factor
EF	Efficiency
E <sub>g</sub>	Band Gap Energy
Hg	Mercury
V	Voltage
E	Electric field

SPD	Spray Pyrolysis Deposition
MOCVD	Metal Organic Chemical Vapor Deposition
ILGAR	Ion Layer Gas Reaction
VPE	Vapor-Phase Epitaxy
$L_c$	Carrier Collection Length
W	Absorber Layer Thickness



## CHAPTER 1

### EXTREMELY THIN ABSORBER LAYER (ETA) SOLAR CELLS

#### 1.1 Introduction

Today, energy has an important role in daily life and international relations. Due to human activities, both the global energy need and green house gases emissions (GHG) are growing. The projection of the energy demand submitted by the Energy Information Administration (EIA) of the U.S. Department of Energy in 2013 implies the expansion of the world energy use from 54% in 2010 to 65% in 2040 [1]. In order to overcome the global energy need, an increase in employing the clean coal besides the increase in progress of renewable energy sources is recommended.

Along with growing of energy need, climate change and global warming caused by burning of fossil fuels are important issues. To avoid the unhealthy rise of the GHG emissions, renewable energy sources should be investigated to become the permanent and lasting substitute of fossil fuels. Among the different energy sources, solar energy appears to be the best choice for the world energy demand since it is cheap, clean, sustainable, limitless and environment friendly [2]. Solar energy technologies developed from laboratory scale template to economically feasible power plant, which resulted a decrease in price. The photovoltaic (PV) conversion is the clean and efficient way for converting the solar energy into electricity. In fact due to all the restraints, both scientifically and politically, there is a huge interest towards the investigation, development and applications of photovoltaic (PV) cells with high efficiency. One of the most effective ways to harvest energy from the sun, which is the primary and renewable source of energy, is the use of photovoltaic (PV) effect in solar cells [3]. According to a report of EIA in 2016, the electricity generation from renewable sources is predicted to grow 9% [4].

The sun is a fusion reactor, which supplies the one-year energy demand of the world just in one minute. The amount of sun's radiation on the earth over a three-days period is identical to the stored energy in all fossil fuels [5]. To make the renewable energies to be compatible with fossil fuels, the production cost should be reduced and the efficiency must be increased. Regarding the fact that solar energy provides an incredible amount of energy demanded for earth; people from 18<sup>th</sup> century were trying to introduce the solar thermal collectors [5]. Horace de Saussure, was the first scientist who invented the solar thermal collector [6]. The electricity generation from the solar energy by the solar cells, which was discovered by Alexander Edmond Becquerel, French physicist, was the start of the solar energy technology [7].

## **1.2 Photovoltaic Devices: Solar Cells**

The solar cell is fundamentally a p-n junction diode, which converts sunlight into electricity. When semiconductors absorb light, photons with energy greater than the material band gap cause the creation of electron-hole pairs in the depletion region. Due to the internal electric field generated at the depletion region of a p-n junction, the created electrons and holes are drifted toward n-type and p-type side, respectively, which results a current flow. Solar cell efficiency depends on photon absorption and consequently generation of electron-hole pairs in the semiconductor material. In Figure 1.1 illustrates the typical operation for a p-n junction crystalline silicon (Si) solar cell, highlighting the charge separation path.

In general the solar cell structures are specified in three different groups. The "First generation" PVs include the monocrystalline Si (c-Si) wafer solar cells, which are the traditional single band gap solar cells with 31% "Shockley-Queisser", efficiency limit. Thin film technology known as "second generation" devices started to develop in 1980s. These classes of solar cells use thin film semiconductor absorber layers such as CdTe, GaAs, CIS instead of single crystalline Si wafers, which resulted a reduction in material costs. Since second generation solar cells yet stand on single band gap heterojunction, they do not exceed the Shockley-Queisser limit. "Third generation" solar cells, use the "second generation" materials, with different structures including quantum dots, p-i-n/n-i-p and multijunctions. Dye-sensitized (DSSC), organic polymer, and Extremely Thin Absorber (ETA) layer solar cell devices are also



included in the third generation solar cells. The efficiency values of these devices theoretically obey the Carnot thermodynamic limit, which means higher than the single band device limit.

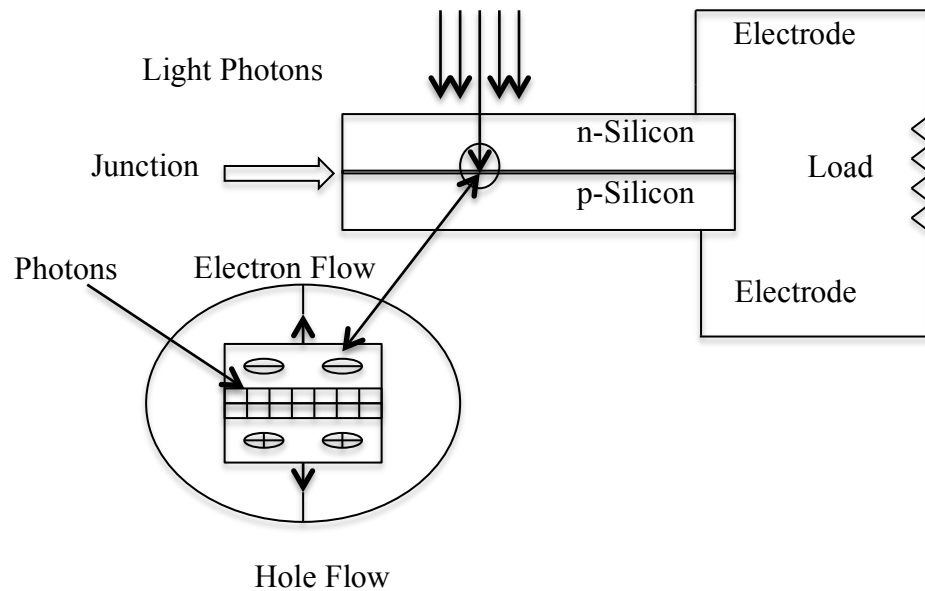


**Figure 1. 1** Photovoltaic effect in a p-n junction solar cell [8]

Different technologies of PVs for solar energy conversion have been progressed over the last 30 years. Even though crystalline Si solar cells play the most important role among PV technology marketing, the other two generation solar cells are promising candidates of future PV technology.

### 1.2.1 First Generation Solar Cells

First generation solar cells, which govern the total sale markets more than %90, generally use high purity silicon as the absorbing semiconductor material. This generation is the oldest and the more commonly used one due to the obtained high efficiencies. Despite the new technologies in fabrication of traditional c-Si p-n junction solar cells, most of them use the similar procedure presented for conventional

p-n junction given in Figure 1.1. Monocrystalline, polycrystalline and hybrid silicon solar cells are different types of Si-based solar cells depending on the type of silicon material used. Eventhough the efficiencies of c-Si solar cells are higher than the polycrystalline solar cells, the production of multycrystalline solar cells is easier and cheaper. The maximum efficiency of the first generation solar cells belongs to silicon heterostructures with value of 25.6% which was submitted by National Renewable Energy Laboratory (NREL) in 2015 [9]. Eventhough the efficiency of this generation is high compared to the others, it has some disadvantageous such as high cost of Si and complex fabrication processes.

### **1.2.2 Second Generation Solar Cells**

The idea behind the “second generation” photovoltaic devices is the use of direct band gap semiconductor materials instead of less efficient indirect band gap silicon. For “second generation” solar cells only a very thin layer of material is demanded to produce cells with efficiency comparable to Si cells. Second generation solar cells can also be named as thin-film solar cells due to the low thickness of layers used in this generation compared to the first generaion solar cells. The reduction of the demanded material makes this generation to be cost effective. Different materials such as cadmium telluride (CdTe), copper indium diselenide (CIS) and copper indium gallium diselenide (CIGS) are used in second generation solar cells. According to the results submitted by National Renewable Energy Laboratory (NREL) in 2015, CIGS and CdTe based solar cells reach the efficiencies of about 21.7% and 21.5% respectively, [9].

Here the typical CdTe solar cell is described as an example of the second geration solar cells which use the thin-film semiconductor materials as the absorber layer. CdTe thin films are promising candidate for PV applications with almost ideal optoelectronic properties. As the typical thin film p-n heterojunction structure, the schematic of n-CdS/p-CdTe (thickness < 4  $\mu\text{m}$ ) solar cell device is presented in Figure 1.2 for which, CdS thin film behaves as the window layer.

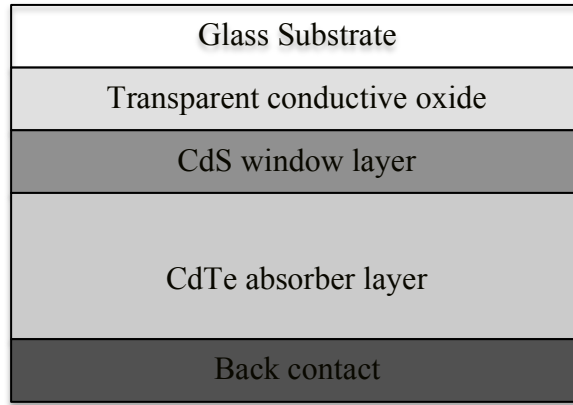


**Figure 1. 2** The Schematic of CdS/CdTe thin-film solar cells [10]

### 1.2.3 Third Generation Solar Cells

Third generation solar cells enhances the efficiency of thin film cells by keeping the module cost as low as second generation cells. In order to attain the high efficiency, the loss processes such as junction and contact resistance, thermalization and recombination losses should be minimized. Currently new types of solar cells such as tandem cells are being investigated for the realization of high efficiency solar cells, minimizing the mentioned losses. Although the maximum efficiency for third generation solar cells is reported as 12.6%, by National Renewable Energy Laboratory (NREL) in 2015 for inorganic cells [9], they have potential for having very high efficiency values around 30%. This generation has some advantages such as the ease of finding raw materials, easier fabrication processes compared to other two generations and low cost for polymer based solar cell devices. As their disadvantages, the high cost of both dye and platinum electrode for organic based third generation solar cells can be mentioned [5].

For the nano structured solar cells which use the advanced fabrication methods and solar cell geometries, the cost of raw materials is low due to the decrease of the amount of absorber material used in the fabrication. The nano structured materials enhance the light trapping and the solar-to-electric energy conversion for the solar cell applications. The organic solar cells, DSSCs and the ETA solar cells are examples for these types of solar cells.

### 1.2.3.1 The Dye-Sensitized Solar Cells (DSSC)

Michael Grätzel and Brian O'Regan evolved this type of solar cell in 1991 for the first time [11]. For the most common DSSC structure there are two heterojunctions such as  $\text{TiO}_2$  nanoparticles/visible light absorbing dye (not doped)/hole-conducting electrolyte. The charge separation appears at the interface between the wide band gap transparent material Titanium oxide ( $\text{TiO}_2$ ) and the conducting dye. Figure 1.3 illustrates the schematic of the general operation of classical DSSC structure. The photons passing through the transparent conductive oxide glass anode and  $\text{TiO}_2$  nanoparticle layer, are absorbed by the sensitizing dye. The electrons after being excited to the excited state of the dye ( $\text{S}^*$  in Figure 1.3) are injected to the conduction band of  $\text{TiO}_2$  layer. The electrons diffuse through the  $\text{TiO}_2$  layer, reach the anode and are directed through the external load. Simultaneously by the electron donation from an  $\text{I}^-$  ion in the electrolyte, the dye forming  $\text{I}^{\cdot-}$  goes back to its ground state and by the electron injection to the  $\text{TiO}_2$  layer the triiodide is reduced and finally the redox cycle at the cathode is fulfilled [12].

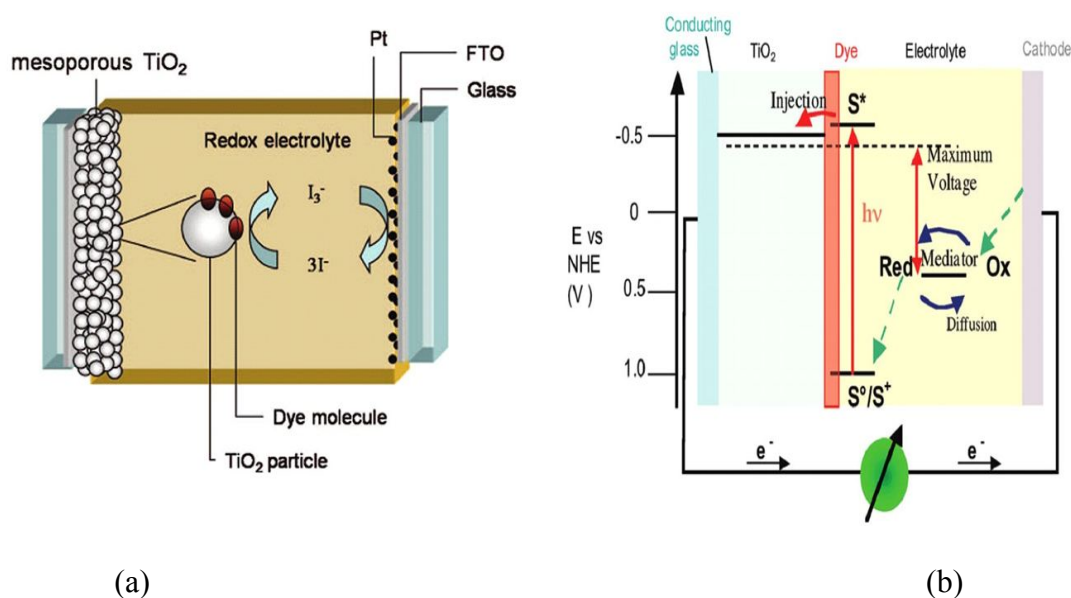


**Figure 1.3** (a) The schematic illustration of dye-sensitized solar cells (Hagfeldt, et al., 2010), (b) Working principle of a typical DSC employing an iodide/triiodide-based redox electrolyte and N719 as a sensitizer (Grätzel, 2009) [13]

The dominant benefit of these cells is the easy fabrication processes and the low cost of the cell materials. In spite of all the mentioned profits, these cells have some disadvantages such as the degradation of the liquid electrolyte under UV radiation, leakage of the electrolyte in the case not attached perfectly and the hopping diffusion mechanism of the electrons through TiO<sub>2</sub> nanoparticle layer which causes the recombination in the cell [13].

### **1.2.3.2 Organic Solar Cells**

The idea behind the operation of these cells developed at the end of the 1950s, while Kearns and Calvin were reported the PV effect and photoconductivity in a two-layer organic system [14]. Even though in organic solar cells a heterojunction is formed which acts like a p-n junction, there is a difference between organic solar cells and first generation single junction solar cells due to the charge transport mechanism which was clarified by Tang as the exciton diffusion in 1986 [15].

The light conversion mechanism in a conventional organic solar cell is as follows; the light is absorbed in an active layer which excites electrons to the conjugated polymers conduction band, leaving holes in the active layer. Thus excitons (electron-hole pairs) are created in the material [16]. The difference between the highest occupied molecular orbital (HOMO) level of the donor and the lowest unoccupied molecular orbital (LUMO) level of the acceptor makes chemical potential gradient in the donor-acceptor junction which cause a contribution to the field induced drift of the excitons. Later by moving the excitons to dissociation site they become separated due to the electric fields generated at the interface. In fact the current on the external load depends on the diffusion of the exciton to the dissociation site. Easy fabrication, low-cost and having vast structural properties are some of the advantageous of polymer-based solar cells but due to their low efficiencies they are not comparable to silicon or even thin-film solar cells.

## 1.3 Extremely Thin Absorber Layer (ETA) Solar Cells

### 1.3.1 General Information

Over the past few years, new designs have been proposed for photovoltaic devices which are expected to produce higher conversion efficiencies. ETA solar cell acts as a p-i-n structure where a very thin absorber layer is sandwiched between two interpenetrating transparent semiconductors ( $E_g > 3$  eV) [17,18]. ETA solar cells consist of a nano or micro structured layer which serves as an n-type window layer, an absorber layer ( $1.1 < E_g < 1.8$  eV) conformally deposited on n-type layer and a void filling p-type material with a metallic back contact. This structure use the highly structured substrate as the n-type material, which reduces the transport path for the excited charge carriers in the absorber layer and simultaneously increases the optical path for photon absorption. The absorber layer used in this structure is very thin, which reduces the probability of electron-hole recombination. ETA solar cells aim to combine the advantages of using very thin and cheaply produced absorber layers on nano structured substrates with stability of all-solid-state solar cells. In order to fulfill the ETA solar cell structure, a highly structured transparent layer is deposited on a conducting glass substrate, followed by the deposition of the thin absorber layer which covers the structured wide band gap semiconductor. Finally a void-filling transparent semiconductor and the reflecting metal layer as the back contact are deposited on the absorber layer.

The schematic and the band diagram of an ETA solar cell are presented in Figure 1.4. For this structure the incoming photons passing through both the transparent TCO and n-type layer, are absorbed in the absorber material and the electrons-hole pairs are generated. Due to the energy-band structure of ETA solar cell and also short transport path length in the absorber layer, the generated electrons and holes are transported to n-type and p-type layers respectively. In fact the band alignment of this structure should be such that electrons and holes can only transfer from the absorber to the n- and p-type materials respectively. This means that the electron and hole transfers are blocked to p- and n-type materials due to the large valence band and conduction band offsets.

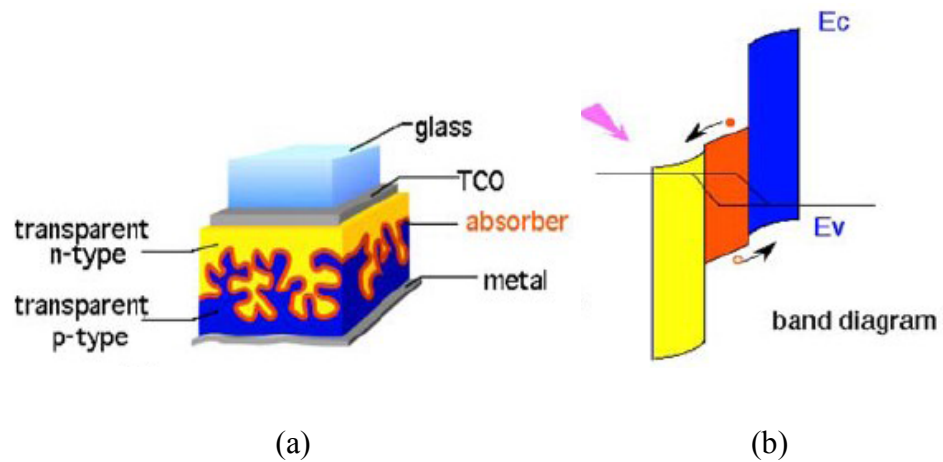


**Figure 1. 4** (a) The schematic and (b) Idealized Band diagram of an ETA solar cell [19,20]

When the absorber layer is a p-type conductor material with the desired electronic properties, the structure of ETA solar cell can be simplified by removing the transparent p-type hole conductor layer. This structure is named as a two-component ETA solar cell. Even in this case the thickness of the absorber layer must be kept in nanometer scale to preserve at least one of the conditions to be defined as ETA solar cell [21].

In ETA cells [22], due to the use of an absorber layer with a thickness of nanometers scale, collection probability is improved because of shorter transport path length for the excited charge carriers and also the probability of electron-hole recombination is reduced. One of the key factors of an ETA solar cell is the surface enlargement of the absorber layer films compared to flat ones. This highly structured p-n heterojunctions provides the sufficient absorption of the light [23]. It is found that a highly structured substrate can reduce the transport path for the excited charge carriers in the absorber material and simultaneously increase the optical path for photon absorption [19,20,24]. Due to the increased scattering and reflection at the internal interfaces of the structure and in the light absorbing material, the optical path through the sample increases, which causes an enhancement of the photon absorption [25]. The mentioned process is known as light-trapping and is presented in Figure 1.5 (The green arrows represent the possible path of a photon) [20]. The light-trapping concept in a solar cell structure was reported by David Redfield in 1974 to increase the efficiency of the cell.

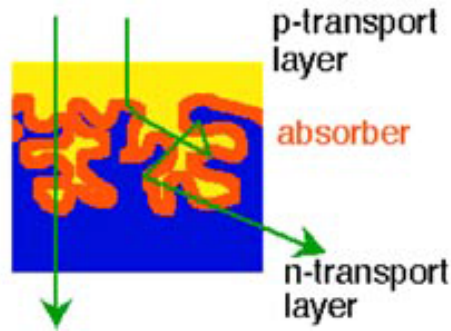


**Figure 1. 5** Light trapping in the ETA cell [18]

In order to get a good light-trapping of solar light, the window layer should have a structure with a typical length scale in the wavelength range of solar light. In fact, the local thickness of the absorber in ETA solar cell devices can be decreased compared to the planar thin film solar cells [18]. As it is mentioned above, the transport path of the charge carriers in the absorber layer decreases. The charge carrier collection probability is enhanced where it limits the electron-hole recombination probability in the absorber layer.

### 1.3.2 Literature Survey

As described in the previous sections, the solar cell structures with ETA layer, which would allow the use of less expensive materials and/or processes, consist of an extremely thin absorber, which is sandwiched between two interpenetrating transparent nano structured n- type and a void filling p-type semiconductors followed by a metallic back contact [17,26-31]. The concept of ETA solar cell is similar DSS cells, which use a dye for light absorption [32,33]. A review of the literature shows that different methods are proposed for the deposition of different layers in this structure. Till now the most frequently used materials as n-type window material for ETA solar cells have been porous  $\text{TiO}_2$  [34,35] and ZnO nanowire films [36–38]. As the absorber materials, CdTe [17,36], HgCdTe [39] CuInS<sub>2</sub> [40], a-Si:H [37] and Se [41] have been used. Finally as the void filling wide band gap p-type material, CuSCN [35,40,42] and ZnTe [41] were used.



The concept which can be thought as the basics of ETA cells was proposed by Green and Wenhams (1994) as a parallel multijunction silicon solar cell based on increasing the charge carrier collection probability [25]. Later, organic and inorganic material based solar cell structures such as the solid state DSSC were developed. Konekamp et al. in 1996 presented the ETA concept as a quantum dot heterojunction [43]. In 1997 Siebentritt et al. proposed the concept of fully-inorganic heterojunction solar cells as the ETA cell structure [44]. Tennakone et al. in 1998 proposed a fully inorganic nanoporous n-TiO<sub>2</sub>/Selenium/p-CuSCN solar cell [42], in which Se acts as a sensitizer for wide band gap n-type TiO<sub>2</sub>. Later in 1999 Rost et al, published the work on SnO/TiO<sub>2</sub>/CuSCN/Graphite p-n structure, which stated that the mentioned heterojunction could be considered for the fabrication structure of a p-i-n type ETA solar cells [23]. In 2000, Ernst et al. examined the suitability of II-VI compounds such as ZnTe and CdTe thin films by electrodeposition (100-200 nm thickness) method on porous TiO<sub>2</sub> substrates with minimum thickness of 2 μm. They observed that ZnTe layer can not fill the pores of nano structured TiO<sub>2</sub> layer as well as CdTe layer. In fact, ZnTe can be a good candidate of p-type top layer for ETA CdTe layer [41].

In 2001 Kaiser, et al. reported the studies on the effect of absorber thickness on the photocurrent density of TiO<sub>2</sub>/CuInS<sub>2</sub>/CuSCN solar cells [40]. In the same year, Konekamp et al. published the work on TiO<sub>2</sub>/CdS/CdTe ETA structure, in which CdTe and CdS were used as absorber and buffer layers respectively [17]. For the mentioned structure CdS thin film layer was coated with different thicknesses by two different deposition techniques, for which the electrodeposited CdTe layer was CdCl<sub>2</sub> treated, resulting better fill factor (FF) values. In 2002 the same group presented the results on the fabrication of the nano structured porous TiO<sub>2</sub> and columnar ZnO with cheap and large area deposition techniques such as spray pyrolysis and electrodeposition. They concluded that columnar ZnO films can be better candidate for device applications than porous layers [17]. In the same year another group worked on ZnO (several micrometers)/CdTe (40-75 nm) structure, and they observed that the vapor phase epitaxy deposited CdTe have an adaptable morphology with columnar ZnO films. This structure can be used for ETA solar cell applications by deposition of a wide band gap p-type material [36]. In 2003 Konekamp et al. worked on Glass/SnO<sub>2</sub>/microporous TiO<sub>2</sub>/CMT/Au structure, where they used

electrodeposited CdTe alloyed with mercury (Hg) as the absorber layer in order to reduce the band gap energy ( $E_g$ ) of the absorber layer. The reduction in the  $E_g$  value is expected to reduce the conduction band offset at the interface with  $TiO_2$ , which resulted an increase in the FF value [21]. In 2006, Anca Duta worked on fabrication of the dense and nanoporous  $TiO_2$  anatase films by spray pyrolysis deposition (SPD) technique. They showed that, by studying the precursors' concentration and deposition parameters; the morphology of  $TiO_2$  layers coated by SPD technique can be controlled [45]. Konenkamp et al in 1999 studied the  $SnO_2/TiO_2/CuSCN/graphite$  structure and observed that CuSCN is a promising p-type material in ETA structure, later in 2006 Claude Levy et al. studied CdSe thin film as the absorber layer in ETA solar cell structure with efficiencies of about 1.5%.

Different methods and materials were investigated to explore highly structured geometry to improve the charge transport in ETA cells. A review of the literature shows that there has been an increasing effort to get uniform deposition of the absorber on nano structured n-type materials by different techniques such as CdTe by electrochemical deposition [27], vapor-phase epitaxy (VPE) [31], metal organic chemical vapor deposition (MOCVD) [33]; a-Si:H by plasma-assisted chemical vapor deposition (CVD) [32] and  $CuInS_2$  by ion layer gas reaction (ILGAR) [23] methods. Nevertheless, to the best of our knowledge, there are limited numbers of published results for the complete ETA solar cell structures.

### **1.3.3 ETA Solar Cell P-I-N Model**

#### **1.3.3.1 Physical Description**

To have a highly efficient solar cell, two important criteria must be fulfilled. The carrier collection length ( $L_c$ ) in the solar cell must be greater than the thickness of the absorber layer,  $W$ , formulated as  $L_c/W > 1$ . Also the absorber thickness approximately must be the inverse of the light absorption coefficient  $\alpha$ ,  $W \cong \alpha^{-1}$ . The first factor ensures that the separated charge carriers in the absorber layer do not recombine before they are collected and the second one implies that the most of light passing through the cell is absorbed. As the result of the mentioned two criteria,  $L_c\alpha$  must be

greater than 1 for the standard solar cell,  $L_c\alpha > 1$ . In fact a high electronic quality material is demanded to ensure the diffusion length to be larger than the absorption thickness [22]. Because of the folded structure in ETA solar cell, its major factor  $L_c\alpha > 1$  can not be applied. In fact two important factors for ETA solar cells are  $L_c/W > 1$  where reducing  $W$  permits to use materials of low electronic quality and hence lower cost. As the other criteria,  $W_{tot}\alpha > 1$  must be satisfied where  $W_{tot}=NW$  is the total thickness of ETA solar cell established by  $\alpha$  [22]. These optical and the electronic properties of the heterostructure are advantages for photovoltaic applications.

Bulk and interfacial recombinations are two different mechanisms, which can occur in ETA solar cells. There is an optimum thickness as a function of roughness that minimizes both recombination processes [22]. Two different kinds of interfacial recombination mechanism are illustrated in Figure 1.6 with red arrows. Interfacial recombination in ETA solar cells subjected to the strong electric field is supposed to be the both trap-assisted and direct recombination (Zener tunneling), which are widely known aspects in a p-n junction [46,47].

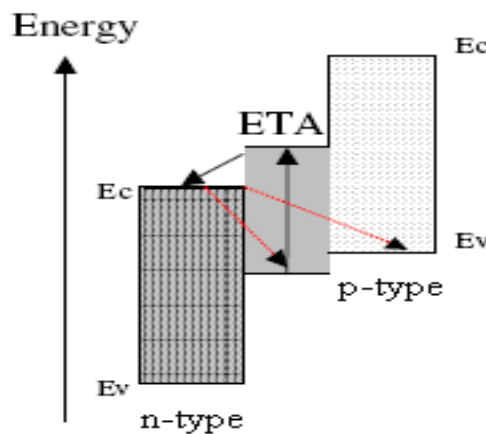


**Figure 1. 6** Interfacial recombination processes (shown as red arrows) in an ETA cell [22]

### 1.3.3.2 Mathematical Modelling

To our knowledge, there are not many works on the modeling of ETA solar cells. Grasso et al. in 2001 presented a model for TiO<sub>2</sub>/CdTe ETA solar cell using quantitative simulation program SCAPS-1D for thin film solar cells. This program is suitable for simulating the planar structure of semiconductor layers. Since application of this model to ETA solar cells neglects the optical and morphological structure present in the structure, they considered the total thickness of ETA cell as the effective absorber thickness in the planar model. By assuming that the conduction band offset of cell is about 0.7 eV and also considering the doping concentration and electron lifetime for both TiO<sub>2</sub> and CdTe, they simulate the experimentally measured S-shaped I(V) and QE( $\lambda$ ) curves. So, for the spectral behavior of the device both the material properties and the planar cell structure are demanded. The studies showed that; even though the optical path enhancement is a benefit of this cell structure, the transport properties are determined as the more important factor for obtaining higher collection efficiency [48].

Most of the theoretical modeling studies on current density-voltage characteristics of an ETA cell were done on a p-i-n junction structure composing of hole and electron conductor materials and intrinsic light absorber layer [22,49]. The model proposed by Taretto et al. is an improved model based on the work by Grasso et al. for a p-i-n junction [22], which applies both light trapping and enhanced tunneling recombination as two important factors present in ETA solar cell structure. This model is the best suitable theoretical modeling for ETA solar cell structure. The energy band diagram for ETA solar cell in thermodynamic equilibrium for absorber thickness W and band gap energy  $E_g$  is presented in Figure 1.7.

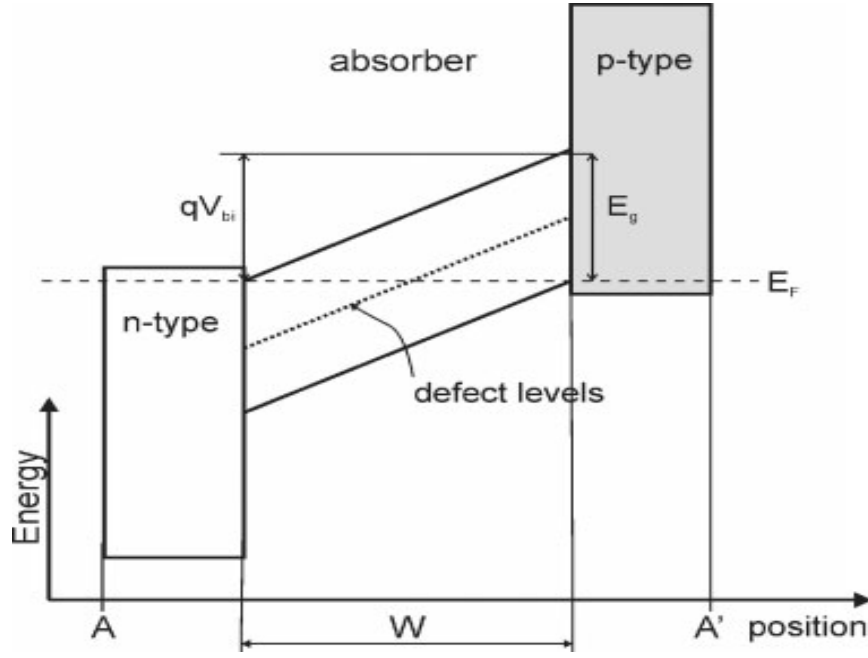


**Figure 1. 7** Energy band diagram for ETA solar cell [22]

According to the model proposed by Taretto et al. both drift and diffusion currents are considered and the continuity equation is solved resulting an expression for the J-V characteristics of the p-i-n type solar cells. The electron carrier concentration in the intrinsic absorber layer is given as;

$$G - \frac{n(x) - n_0(x)}{\tau} + D \frac{d^2 n(x)}{dx^2} + \mu E \frac{dn(x)}{dx} = 0 \quad (1.1)$$

Where  $G$ ,  $D$ ,  $\tau$ ,  $\mu$ ,  $E$  and  $\frac{n(x) - n_0(x)}{\tau}$  are the photogeneration rate, diffusion constant, recombination lifetime, charge mobility, electric field and the recombination rate.

In order to simplify this model some physical considerations must be applied such as;

- 1) It is assumed that the electric field in the intrinsic absorber layer is uniform;

$$|E| = \left| \frac{V - V_{bi}}{W} \right| \quad (1.2)$$

where  $V$  is the applied voltage,  $V_{bi}$  is the built-in voltage and  $W$  is the absorber thickness.

- 2) The  $J_{CR}$ , the critical current density, must satisfy the condition  $J < J_{CR}$ ;

$$j_{CR} = \frac{q\mu N_d E}{\exp\left(\frac{FV}{V_t}\right) - 1} \quad (1.3)$$

where  $q$  is the elementary charge,  $\mu$  is the carrier mobility and  $N_d$  is the doping density of the p- and n-layers.  $N_d$  is used to determine the built-in voltage as  $V_{bi}$ , by  $N_d = n_i \exp\left(\frac{V_{bi}}{2V_t}\right)$  where  $n_i$  is the intrinsic carrier concentration of the absorber,  $V_t$  given by  $V_t = \frac{kT}{q}$  is the thermal voltage. In this expression  $k$  is Boltzmann's constant, and  $T$  is the absolute temperature [29].

- 3) The photogeneration rate in the intrinsic absorber layer is homogeneous. The mean generation rate is calculated as;

$$\bar{G} = \frac{1}{NW} \int_{E_g}^{h\nu_{max}} \Phi_{sun}(h\nu) A(h\nu) d(h\nu) \quad (1.4)$$

$\Phi_{Sun}$  is the solar photon flux between the bandgap of the absorber layer  $E_g$  and the maximum solar flux energy  $h\nu_{max}$ . Also,  $A$  is the absorbance which depends on the wavelength.

- 4) The carrier mobility ( $\mu$ ) and lifetime ( $\tau$ ) is assumed to be the same for electrons and holes. The recombination time, which occur via defect levels in the band gap is given by;

$$\tau = \frac{\tau_0}{1+\Gamma} \quad (1.5)$$

Where  $\tau_0$  is the nominal lifetime.  $\tau_0$  defines the carrier trapping properties of the defect level, related to the nominal diffusion length  $L_0$  by;

$$L_0 = (D\tau_0)^{1/2} \quad (1.6)$$

where  $D$  is the diffusion coefficient of the charge carriers.

$\Gamma$  is the field-effect function due to the tunneling-enhanced recombination, given by;

$$\Gamma = \frac{\Delta E_{n,p}}{KT} \int_0^1 \exp\left(\frac{\Delta E_{n,p}}{KT} u - K_{n,p} u^{3/2}\right) du \quad (1.7)$$

where,  $\Delta E_{n,p}$  is the energy difference between the valance or conduction band respectively for holes-electrons and the defect level.  $K_{n,p}$  is presented as the following equation;

$$K_{n,p} = \frac{3}{4} \frac{\sqrt{2m_{tun}\Delta E_{n,p}^3}}{q\hbar|F|} \quad (1.8)$$

Where  $\hbar$  is the reduced Planck's constant and  $m_{tun}$  is the effective tunneling mass.

$\Gamma$  is strongly dependent on the  $F$  or  $\Delta E_{n,p}$  but not the  $m_{tun}$ , so one can presume that  $m_{tun}=m_0$  where  $m_0$  is the free electron mass [47].

Following these four criteria's, Taretto et al. formulated a model for  $j(D, \tau, W, S, G, V_{bi}, V)$ , where  $S$  is the recombination velocity of the minority carriers at the absorber interfaces. The steady-state continuity equation for electrons as minority carriers can be written in the dimensionless form;

$$G_s + \exp(-V_{S0}x_s) - n_s(x_s) + L_s^2 V_s \frac{dn_s}{dx_s} + L_s^2 V_s \frac{dn_s}{dx_s} + L_s^2 \frac{d^2 n_s}{dx_s^2} = 0 \quad (1.9)$$

the above equation is solved to find the following expression;

$$n_s(x_s) = G_s + n_s^0 \exp(-V_{S0}x_s) + C_1 \exp(\lambda_1 x_s) + C_2 \exp(\lambda_2 x_s) \quad (1.10)$$

Where  $G_s = \frac{G\tau}{n_{p0}}$  is the scaled photogeneration rate,  $n_{p0}$  is thermal equilibrium electron concentration for the p-layer,  $V_{S0} = \frac{-V_{bi}}{V_t}$  and  $V_s = \frac{V-V_{bi}}{V_t}$  is the scaled potential drop. Also  $n_s^0$  is given by  $n_s^0 = \frac{1}{1+(V_s-V_{S0})L_s^2 V_{S0}}$ .  $x_s$ ,  $n_s$  and  $L_s$  are respectively the scaled distance, scaled electron concentration and scaled diffusion length, which are given by  $x_s = \frac{x}{W}$ ,  $n_s = \frac{n}{n_{p0}}$ ,  $L_s = \frac{L_0}{W}$ .

$C_1$  and  $C_2$  constants were found out using the boundary conditions and the two eigenvalues  $\lambda_1$  and  $\lambda_2$  are defined as  $\lambda_{1,2} = \pm \sqrt{\left(\frac{W}{L_0}\right)^2 + \left(\frac{V-V_{bi}}{2V_t}\right)^2} - \frac{V-V_{bi}}{2V_t}$ .

The first boundary condition is defined for the charge transport in the pin-junction, which the drift and diffusion currents are considered to be equal.

$$S_s(n_s(0) - 1) = V_s n_s(0) + \frac{dn_s}{dx_s} \Big|_{x_s=0} \quad (1.11)$$

In this equation the scaled recombination current yielded by the scaled surface recombination velocity  $S_s = \frac{SW}{D}$  is regarded to be equal with drift current at  $x_s=0$ .

For the second boundary condition, electron concentration values at  $x_s = 1/2$  is used,

and for  $x \leq x_C$ ,  $E_{Fn}$  is assumed to be constant. It is expressed as;

$$n_s \left( \frac{1}{2} \right) = \left( \frac{n_i}{n_{p0}} \right) \exp \left( \frac{V}{2V_t} \right) \quad (1.12)$$

$C_1$  and  $C_2$  constants are solved using these two boundary equations and determined to be as;

$$C_1 = \frac{-\exp(-\lambda_2/2)}{A_s} [A_1(\lambda_2 + S_s) + A_2 \exp(\frac{\lambda_1}{2})] \quad (1.13)$$

and

$$C_2 = \frac{-\exp(-\lambda_2/2)}{A_s} [A_1(\lambda_1 + S_s) + A_2 \exp(\frac{\lambda_2}{2})] \quad (1.14)$$

where,  $A_1 = n_s \left( \frac{1}{2} \right) - G_s - n_s^0 \exp \left( -\frac{V_{s0}}{2} \right)$ ,  $A_2 = n_s^0 (S_s + V_s + V_{s0}) - S_s + G_s (S_s - V_s)$ ,  $A_3 = -\lambda_2 - S_s + (\lambda_1 + S_s) \exp \left( \frac{\lambda_1 - \lambda_2}{2} \right)$ .

The scaled current density is obtained by integrating the generation–recombination term for the interval of  $x = 0$  to  $x = W/2$  and adding the current density due to the surface recombination, finally multiplying by two to account for considering both electrons and holes. The integration is performed over the scaled coordinate  $x_s$ , which results the scaled total current density as;

$$J_s = 2S_s(n_s(0) - 1) + 2 \int_0^{1/2} \frac{n_s(x_s) - \exp(-V_{s0}x_s) - G_s}{L_s^2} dx_s \quad (1.15)$$

by replacing the  $n_s(x_s)$  from the Equation 1.9 in Equation 1.14 and integrating it, the scaled current density  $J_s$  becomes;

$$J_s = 2S_s(C_1 + C_2 + G_s + n_s^0 - 1) + \frac{1}{L_s^2} \left[ \frac{C_1 \exp(\lambda_2/2) - 1}{\lambda_2/2} - \frac{1 - C_2 \exp(\lambda_1/2)}{\lambda_1/2} - \frac{(n_s^0 - 1)(1 - \exp(V_{s0}/2))}{-\frac{V_{s0}}{2}} \right] \quad (1.16)$$

Later the current density  $J$  is defined by  $j = \frac{qn_{p0}D}{W} J_s$  where the multiplied factor of  $J_s$  results from the scaling transformations. In order to specify the different terms of the current density equation, a variety of assumptions must be applied, which helps to



access different hypothetical limits such as the minimum absorber thickness for ETA cell. One characteristic of this cell is the scattering of light in the cell which causes the increased absorption by changing the absorbance  $A(h\nu)$  expression in Equation 1.4.

Taretto et al. explored two different models for the absorbance and present the impact of the models on both the current density equation and the maximum absorber thickness. As the first model for absorbance, a cell with a non-reflecting front contact but a perfectly reflecting back contact (no light-trapping) is concerned. The Beer's law gives the absorbance as;

$$A_{BL}(h\nu) = 1 - \exp[-2\alpha(h\nu)NW] \quad (1.17)$$

where  $\alpha(h\nu)$  is the absorption coefficient of the absorber as the function of the photon energy and N is the number of nanojunctions.

As another model for absorbance by Taretto et al., light trapping was considered in the cell, which results the following equation for the absorbance:

$$A_{LT}(h\nu) = \frac{1 - \exp[-4\alpha(h\nu)NW]}{1 - (1 - n^{-2})\exp[-4\alpha(h\nu)NW]} \quad (1.18)$$

Where n is the refractive index of the intrinsic absorber material. For the direct band gap materials with photon energies which is not much more than the absorber band gap  $E_g$ , absorption coefficient is considered as;

$$\alpha(h\nu) = \alpha_0 \left( \frac{h\nu - E_g}{kT} \right)^{1/2} \quad (1.19)$$

Where  $\alpha_0$  is the characteristic absorption coefficient specified as;

$$\alpha_0 = \alpha(h\nu = E_g + kT) \quad (1.20)$$

Combining these two equations for absorbance models and the equation presented for the absorption coefficient in the J-V model, useful parameters of the ETA solar cell such as the overall cell efficiency can be found;

$$\eta = \frac{V_{mpp}J_{mpp}}{P_{Sun}} \quad (1.21)$$

Where  $V_{mpp}$  and  $J_{mpp}$  are respectively the voltage and current at the maximum power

point. Also the  $P_{\text{Sun}}$  is the power density of the sun's radiation.

## **1.4 Extremely Thin CdTe Absorber Layer Solar Cell Structures Investigated in the Thesis**

In this thesis study, different ETA solar cell structures were investigated including the preparation and characterization of materials and devices. All thin film material layers in the device structures were obtained separately and characterized in detail. The ETA solar cell structures studied in this work are: Glass/TCO/TiO<sub>2</sub>/Sputtered CdTe/Au, Glass/TCO/TiO<sub>2</sub>/Electrodeposited CdTe/Cu-Au and Glass/TCO/TiO<sub>2</sub>/Sputtered CdTe/ZnSnTe/In. The ETA solar cell structures and the properties of the individual layers in ETA structures are described in detail in the following sections.

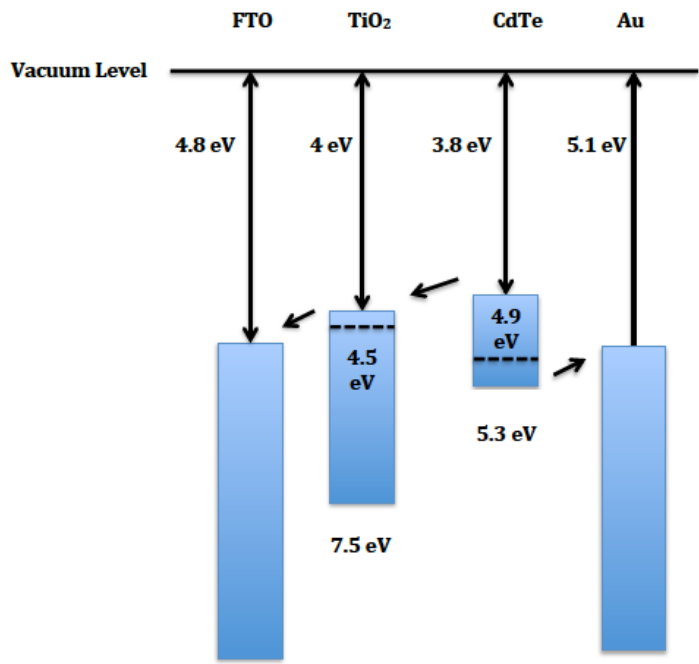
### **1.4.1 Studied ETA Solar Cell Structures**

The studied two and three layered cells have similar structure with DSSC, where CdTe and ZnSnTe have the role of dye absorber and iodide/triiodide electrolyte. The energy levels (band gap energy, electron affinity and work function) of different materials and band diagram presentation of the two- and three-component ETA solar cells studied in this thesis are given in Table 1.1 and Figure 1.8 respectively.

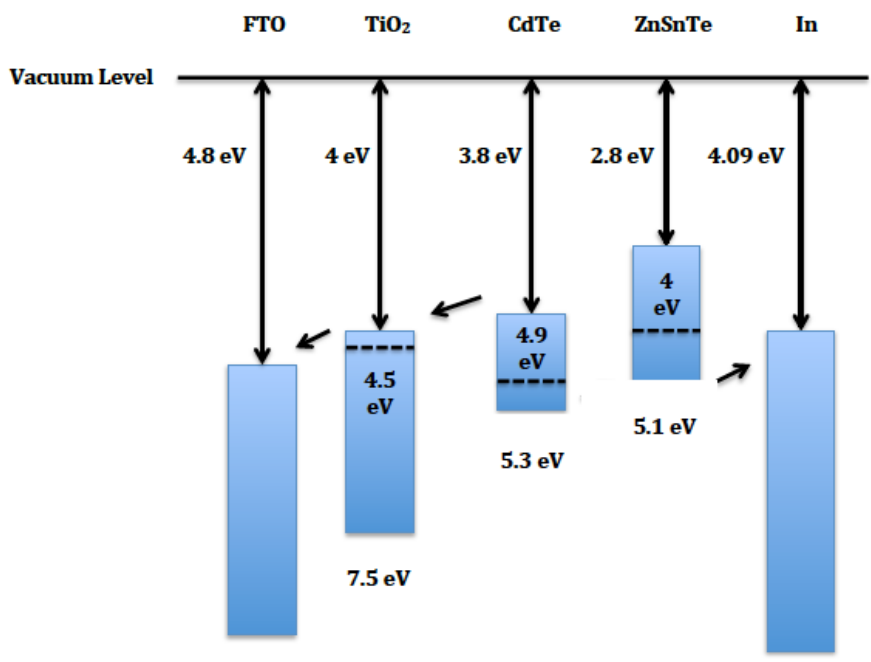
The band alignments between the materials combined in two- and three-component ETA structures have great importances. Depending on the band gap, electron affinity [50] and work function [50] of materials, different charge carrier transports are observed. As it is described in Section 1.3.1, the values for different energy levels are such that the electron transfer takes place from the absorber to n-type material where hole transfer is blocked due to the large valence band offset. Also the hole transfer can occur from the absorber to the p-type material where the electron transfer is forbidden.

**Table 1. 1** The band gap energy, electron affinity and work function values of different layers of ETA cell structures studied in this work

	Band gap eV	Electron affinity eV	Work function eV
FTO	-	-	4.8[51]
TiO <sub>2</sub>	3-3.5 [52,33]	4[53]	4.5[53]
CdTe [54]	1.5	3.8	4.9
ZnTe [55]	2.3	2.8	4
Au	-	-	5.1[51]
In	-	-	4.09[56]
Al	-	-	4.28 [57]



(a)



(b)

**Figure 1. 8** Energy levels of different materials employed for (a) FTO/TiO<sub>2</sub>/CdTe/Au (b) FTO/TiO<sub>2</sub>/CdTe/ZnSnTe/In devices

## 1.4.2 Titanium Dioxide (TiO<sub>2</sub>)

Titanium dioxide is a high band gap semiconductor that has various useful applications due to its photo-conversion properties in the UV spectrum range. It has three crystalline phases: anatase (tetragonal), rutile (tetragonal), and brookite. Both anatase and rutile are more common phases than the brookite and have wide commercial applications. From literature rutile has a direct bandgap of 3.06 eV and an indirect bandgap of 3.10 eV [58], whereas anatase exhibits only an direct bandgap around 3.5 eV [52,59]. Rutile phase, which is especially observed for high temperature annealing [60], is generally used in gas sensors because of being the most stable phase [61]. On the other hand, anatase is a metastable phase of TiO<sub>2</sub> and it has attracted attention for photocatalytic activity [60]. Both rutile and anatase phases of TiO<sub>2</sub> have tetragonal bulk unit cell. In this cell, titanium ions are placed at the center of the octahedron of six oxygen atoms, which the distortion inside this octahedron makes these two phases different from each other [43]. As observed from the unit cell of the two phases presented in Figure 1.9, the average distance between titanium ions and titanium-oxygen ions are respectively greater and smaller for anatase phase compared to rutile, which caused anatase phase to be less stable in bulk form thermodynamically. For anatase phase, where the grains are smaller than 14 nm in diameter, better stable form was observed compared to rutile thermodynamically [36].

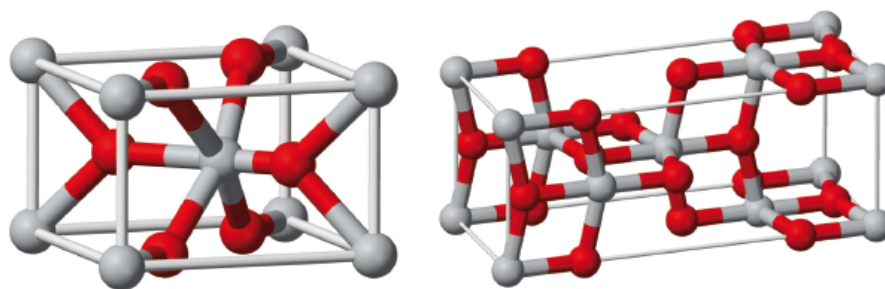


**Figure 1. 9** Bulk unit cell of rutile (left) and anatase (right). Oxygen atoms are red coloured and titanium atoms are grey coloured[62]

TiO<sub>2</sub> films have been used for various useful applications such as gas sensors [61,63,64] and photocatalysis [65-67] due to the strong dependency of its electrical conductivity on oxygen partial pressure and porosity. High refractive index, excellent optical transmittance in the visible range and chemical inertness makes the TiO<sub>2</sub> film a suitable candidate for many optical applications. In photovoltaics, it is used as an electrode for high electron injection, which leads to a higher efficiency [68]. Low charge recombination rates and incomparable transport properties of TiO<sub>2</sub>, as the n-type semi-conducting electron transport layer, cause widespread use of TiO<sub>2</sub> in ETA solar cells.

Various methods to prepare TiO<sub>2</sub> films exist such as chemical vapor deposition (CVD) [69], physical vapor deposition (PVD) [60,70], thermal [71] or oxidation of titanium [72], electron beam vacuum deposition [73], ion sputtering [74] and the sol-gel method [75-77]. Magnetron sputtering deposition of TiO<sub>2</sub> films has also been widely used [78,79] because of better adhesion, higher density layers.

### **1.4.3 Cadmium Telluride (CdTe), Zinc Tin Telluride (ZnSnTe)**

The II–VI semiconductor compounds such as cadmium telluride (CdTe) and zinc telluride (ZnTe) due to their direct energy bandgap, electrical and optical properties, which makes them suitable for the optoelectronic and solar cell fabrication, attracted much attentions for vastly use in the device application for the last few decades.

CdTe is one of the II-VI semiconductors which is used as the absorber layer in ETA solar cell structure due to its ability to absorb visible light ( $1.1 < E_g < 1.8$  eV). Highly resistive CdTe with zincblende structure has an optical band gap around 1.4 eV at 300K [80], close to the optimal absorber band gap, which makes it a good candidate for ETA layer. CdTe thin films are deposited onto different substrates by using different methods such as electrodeposition which is a low cost and large area deposition process with low deposition rate. Deposition from the vapor phase at high temperatures is one of the expensive methods, but it can be preferred for some applications due to the high deposition rates attained [81]. Even though less than 2 μm thick CdTe layer is sufficient for the absorption of solar light, in general thicker CdTe thin film is used as the absorber layer to obtain pinhole free absorber layer and consequently to avoid the shorting to the back contact. For very thin CdTe films the

photoconversion efficiency of the device is reduced because of the short minority carrier diffusion length.

ZnTe is a material with cubic structure, which intrinsically shows p-type conductivity. It has direct transition wide band gap around 2.26 eV at room temperature [82]. Polycrystalline ZnTe has a low electron affinity 3.53 eV [83] and a high absorption coefficient in the order of  $10^4 \text{ cm}^{-1}$  [84]. ZnTe has different applications such as solar cells, photodetectors and light emitting diodes [85,86], these applications make ZnTe a material worths to investigate. Various techniques are reported for ZnTe film preparation such as thermal vacuum evaporation [87] and electrodeposition [88-91]. In order to obtain low resistance ZnTe thin film, it can be doped with such elements like tin (Sn) and copper (Cu), silver (Ag) [92,93]. The novel inorganic low resistance candidate of p-type semiconductor used in this research is ZnSnTe. The ZnSnTe material is prepared by doping ZnTe with sputtering method using SnTe as the dopant.

#### **1.4.4 Outline of the Thesis Presentation**

In this thesis study, different two- and three-component CdTe based ETA layer solar cell structures such as Glass/TCO/TiO<sub>2</sub>/CdTe/Au, and Glass/TCO/TiO<sub>2</sub>/CdTe/ZnSnTe/In were investigated including the preparation and characterization of materials and devices. All thin film material layers in the device structures were obtained separately and characterized in detail. The general description of the experimental methods accompanied with sample fabrication and deposition and characterization techniques are given in Chapter 2. The results of the deposition and characterization of different layers of ETA solar cells including n-type TiO<sub>2</sub> window layer, CdTe absorber layer and p-type ZnSnTe layer fabricated with different deposition techniques are introduced in Chapter 3. The results of the investigation of the complete two- and three-component Glass/FTO/TiO<sub>2</sub>/CdTe/Au and Glass/FTO/TiO<sub>2</sub>/CdTe/ZnSnTe/In ETA solar cell structures accompanied with the simulation results for the best efficient two-component ETA solar cell are given in Chapter 4. The conclusions are presented in Chapter 5.

It should be mentioned that all hydrothermally and electrochemically anodized TiO<sub>2</sub> layers, electrochemically deposited CdTe layers and the solar cells with

electrodeposited CdTe layer were produced and characterized at the University of Alberta. The rest of the research was carried out at Physics Department and Center for Solar Energy Research and Applications (GÜNAM) of Middle East Technical University.



## 1.5 References

- [1] Energy Information Administration. International Energy Outlook 2013. December 2013
- [2] A. Luque, S. Hegedus, Handbook of photovoltaic science and engineering. John Wiley & Sons
- [3] R. Eisenberg, D.G. Nocera, Inorg. Chem., 44 (2005), p. 6799
- [4] Energy Information Administration. Short-Term Energy Outlook 2016. January 2016
- [5] M. TawheedKibria, A. Ahammed, S. M. Soy, F. Hossain, Sh. Islam, Proceedings of 5th International Conference on Environmental Aspects of Bangladesh, (2014), p.51
- [6] A review: Solar cell current scenario and future trends by Recent Research in Science and Technology 2012, 4(8): 99-101, ISSN: 2076-5061
- [7] Solar Cell Research Activities at Plasma & Material Processing group-A. Creatore, R. Sanden, E. K. J. Palmans, I. Dogan, S. Hanssen, S. Smit, B. Loo, B. Macco, S. Bordihn, H. Knoop, D. Garcia-Alonso, K. Sharma, Technische Universiteit Eindhoven- University of Technology
- [8] P. J. Reddy, Science and technology of photovoltaics, BS: 2010
- [9] National Renewable Energy Laboratory, Best Research-Cell Efficiencies 2015. August 2015
- [10] MA. Green, Third generation photovoltaics: Advanced solar energy conversion. Springer; 2003
- [11] B. O'Regan, M. Gratzel, Nature, 353(6346) (1991), p. 737
- [12] M. Grätzel, Journal of Photochemistry and Photobiology C: Photochemistry Reviews, 4(2) (2003), p.145
- [13] X. Gao et al., Enhancing the Light Harvesting Capacity of the Photoanode Films in Dye-Sensitized Solar Cells. InTech: (2013), p.169
- [14] D. Kearns, M. Calvin, J Chem Phys., 29(4) (1958), p. 950
- [15] CW. Tang, Appl Phys Lett, 48(2) (1986), p.183
- [16] S. Gunes, H. Neugebauer, NS. Sariciftci, Chem Rev, 107(4) (2007), p.1324

- [17] K. Ernst, R. Engelhardt, K. Ellmer, C. Kelch, H.-J. Muffler, M.C. Lux-Steiner, R. Könenkamp, *Thin Solid Films*, 382 (2001), p. 26
- [18] K. Ernst, A. Belaïdi, R. Könenkamp, *Semicond. Sci. Technol.* 18 (2003), p. 475
- [19] K. Ernst, M.C. Lux-Steiner, R. Könen K. Ernst, M.C. Lux-Steiner kamp, *Proc. 16th Eur. Photovoltaic Solar Energy Conf. (Glasgow, UK) (2000)*, p. 63
- [20] H.W. Deckman, C.R. Wronski, H. Witzke, E. Yablonovitch, *Appl. Phys. Lett.*, 42 (1983), p.968
- [21] A. Belaidi, R. Bayon, L. Dloczik, K. Ernst, M.Ch. Lux-Steiner, R. Konenkamp, *Thin Solid Films* 431 –432 (2003), p. 488
- [22] K. Taretto, U. Rau, *Prog. Photovoltaics: Res. Appl.*, 12 (2004), p. 573
- [23] C. Rost, S. Sieber, K. Ernst, S. Siebentritt, M.Ch. Lux-Steiner, R. Könenkamp, *Appl. Phys. Lett.* 75 (1999), p. 692
- [24] E. Yablonovitch, G.D. Cody, *IEEETrans.Electron Devices*, 29 (1982), p.300
- [25] M. Green, S. Wenham, *Appl Phys Lett.* 65 (23) (1994), p.2907
- [26] K. Tennakone, G.R.R.A. Kumara, I.R. Kottegoda, V.P.S. Per-era, G.M.L. Aponsu, *J. Phys, D. Appl. Phys.*, 31 (1998), p. 2326
- [27] A. Wahi, R. Könenkamp, *Proc. 11<sup>th</sup> Photovoltaic Solar Energy Conf. (Montreux, Switzerland, 1992) (Harvard Academic Publishers) (1993)*, p.714
- [28] K. Ernst, M.C. Lux-Steiner, R. Könen K. Ernst, M.C. Lux-Steiner kamp, *Proc. 16th Eur. Photovoltaic Solar Energy Conf. (Glasgow, UK) (2000)*, p. 63
- [29] A. Luque, A. Marti, *Phys. Rev. Lett*, 76 (1997), p. 5014
- [30] B. O'Regan, M. Gratzel, *Nature*, 353 (1991), p. 8720
- [31] K. Ernst, A. Belaïdi, R. Könenkamp, *Semicond. Sci. Technol.* 18 (2003), p. 475
- [32] K. Tennakone, G.R.R.A. Kumara, A.R. Kumarasinghe, K.G.U. Wijayantha, P.M. Sirimanne, *Semicond. Sci. Technol.* 10 (1998), p. 583
- [33] B. O'Regan, D.T. Schwartz, *Chem. Mater.* 10 (1998), p. 1501
- [34] R. Könenkamp, L. Dloczik, K. Ernst, C. Olesch, C. *Physica E (Amsterdam)*, 14 (2002), p. 219
- [35] R. Könenkamp, K. Ernst, C.H. Fisher, M.C. Lux-Steiner, C. Rost, *Phys. Status Solidi (A)*, 182 (2000), p. 151
- [36] C. Lévy-Clément, A. Katty, S. Bastide, F. Zenia, I. Mora, V. Muñoz-Sanjosé, *Physica E (Amsterdam)*, 14 (1) (2002), p. 229

- [37] R. Könenkamp, K. Boedecker, M.C. Lux-Steiner, M. Poschenrieder, F. Zenia, C. Lévy-Clément, S. Wagner, *Appl. Phys. Lett.*, 77 (2000), p. 2575
- [38] R. Tena-Zaera, A. Katty, S. Bastide, C. Lévy-Clément, B. O'Regan, V. Muñoz-Sanjosé, *Thin Solid Films*, 486 (2005), p. 372
- [39] A. Belaïdi, R. Bayon, L. Dloczik, K. Ernst, M.C. Lux Steiner, R. Könenkamp, *Thin Solid Films*, 488 (2003), p. 431–432
- [40] I. Kaiser, K. Ernst, C.H. Fischer, M.C. Lux Steiner, R. Könenkamp, *Sol. Ener. Mat. Sol. Cells*, 67 (2001), p.89
- [41] K. Ernst, I. Sieber, M. Neumann-Spallart, M.C. Lux-Steiner, R. Könenkamp, *Thin Solid Films*, 361–362 (2000), p. 213
- [42] K. Tennakone, G.R.R.A. Kumara, I.R. Kottegoda, V.P.S. Perera, G.M.L. Aponsu, *J. Phys. D. Appl. Phys.*, 31 (1998), p. 2326
- [43] R. Könenkamp, P. Hoyer, A. Wahi, *J Appl Phys.* 79 (9) (1996), p.7029
- [44] S. Siebentritt, K. Ernst, Ch.-H. Fischer, R. Könenkamp, M.Ch. Lux-Steiner, *Proc. 14<sup>th</sup> Eur. Photovoltaic Solar Energy Conf. (Barcelona, Spain) (1997)*, p. 1823
- [45] A. Duta, *Thin Solid Films* 511–512 (2006), p.195
- [46] J. Wienke, M. Krunk, F. Lenzmann, *Semiconductor Science and Technology*, 18(9) (2003), p.876
- [47] G.A.M. Hurkx, D.B.M. Klaassen, M.P.G. Knuvers, *Electron Devices, IEEE Transactions on*, 39(2) (1992), p.331
- [48] M. Nanu, J. Schoonman and A. Goossens, *Chem. Vap. Deposition*, 10 (2004), p. 45
- [49] K. Tennakone, A.R. Kumarasinghe, P.M. Sirimanne, G.R.R.A. Kumara, *Thin Solid Films*, 261 (1995), p. 307
- [50] A.G. Milnes and D.L. Feucht, *Heterojunctions and Metal-Semiconductor Junctions*. London: Academic Press, INC. (1972)
- [51] I. Mora-Sero, *Nat Commun.*, 4 (2013)
- [52] A. E. Jiménez González, S. G. Santiago, *Semicond. Sci. Technol.*, 22 (2007), p. 709
- [53] W. Hsu, *Scientific Reports*, 5 (2015), p. 16028
- [54] S. Girish Kumar, K. S. R. Koteswara Rao, *Energy Environ. Sci.*, 7 (2014), p. 45
- [55] C. T. Cheng et al., *J. Mater. Chem.*, 15 (2005), p. 3409

- [56] Work function. n.d. In Wikipedia, Retrieved November 19, 2015 from [https://en.wikipedia.org/wiki/Work\\_function](https://en.wikipedia.org/wiki/Work_function)
- [57] S. Gupta, D. Patidar, N. S. Saxena, K. Sharma, *Chalcogenide Letters*, 6 (12) (2009), p.723
- [58] A. Welte, Ch. Waldauf, CH. Brabec, P. J. Wellmann, 516 (2008), p. 7256
- [59] M. Singh, D. Pathak, A. Mahajan, R. K. Bedi, *J. Optoelectron Adv M.*, 14(2012), p. 624
- [60] S. Sankar, K. G. Gopchandran, *Cryst. Res. Technol.*, 44(9) (2009), p. 989
- [61] F. Hossein-Babaei, M. Keshmiri, M. Kakavand, T. Troczynski, *Sensor Actual B-Chem.*, 110 (2005), p. 28
- [62] Wikipedia, <http://www.wikipedia.org>
- [63] Y. Xu, X. Zhou, O. T. Sorensen, *Sensor Actual B-Chem.*, 65 (2000), p. 2
- [64] L. Francioso, D.S. Presicce, A.M. Taurino, R. Rella, P. Siciliano, A. Ficarella, *Sensor Actual B-Chem.*, 95 (2003), p. 66
- [65] C.H. Ao, S.C. Lee, J.Z. Yu, J.H. Xu, , *Appl. Catal. B: Environmental*, 54 (2004), p. 41
- [66] S.B. Kim, S.C. Sung Chang Hong, *Appl. Catal. B: Environmental*, 35 (2002), p. 305
- [67] J. Yu, J.C. Yu, W. Ho, Z. Jiang, *New J. Chem* 26 (2002), p. 607
- [68] K. Kei Murakoshi, R. Kogure, Y. Wada, S. Yanagida, *Sol Energ Mat Sol C.*, 55 (1998), p. 113
- [69] J.P. Lu, J. Wang, R. Raj, *Thin Solid Films*, 204 (1991), p. L13
- [70] S. Schiller, G. Beister, W. Sieber, G. Schrmer, E. Hacker, *Thin Solid Films* 83 (1981), p.239
- [71] N. Nabavi, S. Doeuff, C. Sanchez, J. Livage, *Mater. Sci. Eng. B* 3 (1989), p. 203
- [72] B. Morris Henry, U.S. Patent, (1978), 4200474
- [73] M. Lottiaux, C. Boulesteix, G. Nihoul, F. Varnier, F. Flory, R. Galindo, E. Pelletier, *Thin Solid Films*, 170 (1989), p. 107
- [74] M.H. Suhail, G. Mohan Rao, S. Mohan, *J. Appl. Phys.*, 71(3) (1992), p. 1421
- [75] H. Schroder, ed. By G. Hass and R. E. Thun, in *Physics of Thin Films*, Academic, New York (5) (1969), p. 87
- [76] B.E. Yoldas, T.W. O'Keefe, *Appl. Opt.*, 18 (1979), p. 3133
- [77] A. Hosseini, K.C. Icli, H.H. Gullu, *TJST.*, 8 (2013), p. 69

- [78] E. Ritter, *Phys. Thin Films*, 8 (1975), p. 1
- [79] H.K. Pulker, *Elsvier Science Publishers B.V.*, (1984), p. 311
- [80] R.H. Bube, *Phys. Rev.*, 98(2) (1955), p. 431
- [81] C. Lepiller, P. Cowache, J.F. Guillemoles, N. Gibson, E. Özsan, D. Lincot, *Thin Solid Films*, (361–362) (2000), p. 118
- [82] M. Nishio, K. Hayashida, Q. Guo, H. Ogawa, *Appl. Surf. Sci.*, 169 (2001), p. 223
- [83] A. Pistone, A. S. Arico, P. L. Antonucci, D. Silvestro, V. Antonucci, *Sol. Energy Mater. Sol. Cells.*, 57 (1998), p. 255
- [84] J. M. Pawlikowski, *Thin Solid Films*, 127 (1985), p. 39
- [85] J. D. Merchant, M. Cocievera, *J. Electrochem. Soc.*, 143 (1996), p. 4054
- [86] T. Ota, and K. Takahashi, *Solid-State Electron.*, 16 (1973), p. 1089
- [87] K. N. Raju, R. P. Vijayalakshmi, R. Venugopal, D. R. Reddy, B. K. Reddy, *Mater. Lett.*, 13 (1992), p. 336
- [88] M. Neumann-Spallart, C. Königstein, *Thin Solid Films*, 265 (1995), p. 33
- [89] B. Bozzini, C. Lenardi, N. Lovergine, *Mater. Chem. Phys.*, 66 (2000), p. 219
- [90] Y. Jun, K. J. Kim, D. Kim, *Met. Mater.*, 5 (1999), p. 279
- [91] A. S. Arico, D. Silvestro, P. L. Antonucci, N. Giodano, V. Antonucci, *Adv. Perform. Mater.*, 4 (1997), p.115
- [92] J. W. L. Yim, D. Chen, G. F. Brown, J. Junaqiao, *Nano Res.*, 2 (2009), P.937
- [93] A. K. S. Aqili, A. J. Saleh, Z. Ali, S. Al-Omari, *J. Alloys Compd.*, 520 (2012), p.83



## CHAPTER 2

### EXPERIMENTAL

#### 2.1 General Description of Experimental Methods

As the first step of the fabrication of Glass/TCO/TiO<sub>2</sub>/CdTe/Au and Glass/TCO/TiO<sub>2</sub>/CdTe/ZnSnTe/In ETA solar cells; the thin film, nanoporous, nanowire and nanotube TiO<sub>2</sub> layers were deposited on the surfaces of bare glass and fluorine doped tin oxide (FTO) substrates. Different methods were used for TiO<sub>2</sub> deposition such as sputtering, spin coating, electrochemical anodization and hydrothermal methods. As the conformal ETA semiconductor layer, void filling CdTe thin film was coated by sputtering and electrodeposition methods onto glass and FTO/TiO<sub>2</sub> substrates. The complete two-component Glass/FTO/TiO<sub>2</sub>/CdTe/Au device structure was fabricated and characterized by thermal evaporation of Au on the structure. For some of the devices a 10 nanometer copper (Cu) metal was evaporated prior to the Au evaporation. As the final step for the three-component ETA solar cells, wide band gap p-type ZnSnTe layer was deposited on Glass/FTO/TiO<sub>2</sub>/CdTe structures and bare glass substrates by sputtering method. The deposition of In back contact was performed by vacuum evaporation onto ZnSnTe layer. The complete laboratory scale ETA solar cell devices of Glass/FTO/TiO<sub>2</sub>/CdTe/Au and Glass/FTO/TiO<sub>2</sub>/CdTe/ZnSnTe/In were produced and characterized to investigate the solar cell structures.

At each step, the relevant thin film materials coated on glass substrates were investigated and characterized to optimize the deposition and material properties for ETA solar cell application. The deposited thin film materials were investigated by thickness measurement, optical, electrical and morphological characterizations, which were conducted by Scanning Electron Microscopy (SEM), Atomic Force Microscopy (AFM), UV-Vis Spectrometer, BET, X-ray Diffraction (XRD) and dark I-V measurement techniques.

In this chapter different deposition methods used for the deposition of n-type, p-type and absorber layers such as nanowire, nanotube and nanoporous TiO<sub>2</sub>, CdTe, ZnTe and ZnSnTe layers in ETA solar cell structures will be presented. Also the details of the optical, electrical and structural characterization techniques used for the material characterization as well as the device characterization methods will be given.

## **2.2 Deposition Methods**

The p-i-n junction ETA solar cell contains different thin film semiconductor layers in the structure. In the following sections the different deposition techniques used for deposition of the different thin film layers in ETA structure will be presented.

### **2.2.1 Sol-Gel Method**

The sol-gel method, which is developed in 1960s can be defined as a method for metal oxide fabrication by polycondensation reactions of a molecular precursor in a liquid. This method uses the charge-stabilized nanoparticulate suspension (sol) to form an integrated network of particles (gel). A sol is a stable dispersion of amorphous or crystalline particles in a solvent and a gel is a three dimensional network, made up from agglomeration of collidal particles, which encircles the liquid phase. Since some of particles do not react even after the gel formation, aging of the gel is a very important factor in sol-gel process. The gel can be dried by using evaporation or under supercritical conditions. For the first drying condition the gel network will collapse with a shrinkage resulted from capillary forces and for the second condition the gel network can be retained which results the existence of large pores.

In fact the sol-gel synthesis is the process which dissolves the compound in a liquid phase to yield a final solid with a controlled manner. Various forms of materials such as thin films and porous structures can be prepared using sol-gel method.

The oxide paste can be coated onto different substrates such as glass and transparent conductive glass (TCO) by spin coating technique. Using different spin rates, layers with high porosity and nanoparticulate nature can be achieved. The coated gel is dried on hot plate (125 °C) and later the dried gel is fired and annealed at 450 °C for particle sintering. As a result, nanoporous conductive oxide film with high surface area, which



is appropriate for solar cell design and fabrication, is produced.

### **2.2.2 Physical Vapor Deposition**

Physical vapor deposition method (PVD) includes the physical procedures such as plasma sputtering and high temperature vacuum evaporation on different substrate surfaces.

Sputtering has been widely used to deposit thin films due to deposition of layers even at low temperatures with better adhesion and higher density. It is also a two direction top-down process for target and substrate. The high-energy sputtered ions ejected from the solid target, due to the present gas atoms, travel in straight or random way and finally they condensate on the substrates. The sputtering gas usually is an inert gas like argon; for having effective momentum transfer the atomic weight of the sputtering gas should be close to that of the target. Infact sputtering take places due to collision between the ions and the atoms of material and consequently the momentum transfer between them. It should be noted that to have an efficient momentum transfer, the atomic weight of the target and sputtering gas should be close to each other. Sometimes sputtering systems contain magnetron in order to use magnetic field in addition to the electric field to restrict the charged plasma particles near to the surface of target.

The main parameter of the sputtering deposition technique is the applied electric field between the target and the substrate. The DC and RF sputtering are suitable for the deposition of the conductive and non-conductive materials respectively. For non-conductive materials deposition, the RF sputtering is used because of the charge accumulation on the surface of the material.

### **2.2.3 Electrodeposition and Electrochemical Anodization Methods**

Electrodeposition (ED) is the process of deposition of a substance on the working electrode in an electrochemical cell using electricity as an external source. The schematic of the two-electrode ED set up is given in Figure 2.1. It is constituted of a reaction vessel with two electrodes, where the FTO substrate as working electrode is cathode and the platinumium (Pt) or graphite as counter electrode is anode. For the two-

electrode system the adjusted current directs the reaction in the chemical to deposit the substance. For three-electrode ED system a reference electrode is also included, which conducts the potential of the working electrode and the deposition is performed by adjusting the current during the potential scan. The reaction in ED system is conducted by Faraday's laws. The Faraday's first law declares that the amount of mass changed on the electrode during electrolysis is proportional to the amount of electricity transmitted from electrode. The second law of Faraday's declares that the chemical equivalent weight of each substance is proportional to the released mass of that substance at the electrode.

ED is a non-vacuum method, which has control over the parameters such as bath temperature, pH, electrolyte concentration, deposition potential and deposition time. In ED, the substrate must be conductive with a very low sheet resistance, which is the most important disadvantage of this method.

Electrochemical anodization is a common way to form an oxide layer on aluminium (Al) or Titanium (Ti) substrate due to its reliability, simplicity, low cost and high controllability. This process is called anodizing since the material which should be treated is anode. The electrochemical anodization set up is similar to electrodeposition, where the Ti coated FTO substrate is anode and the platinumium (Pt) or graphite is cathode.

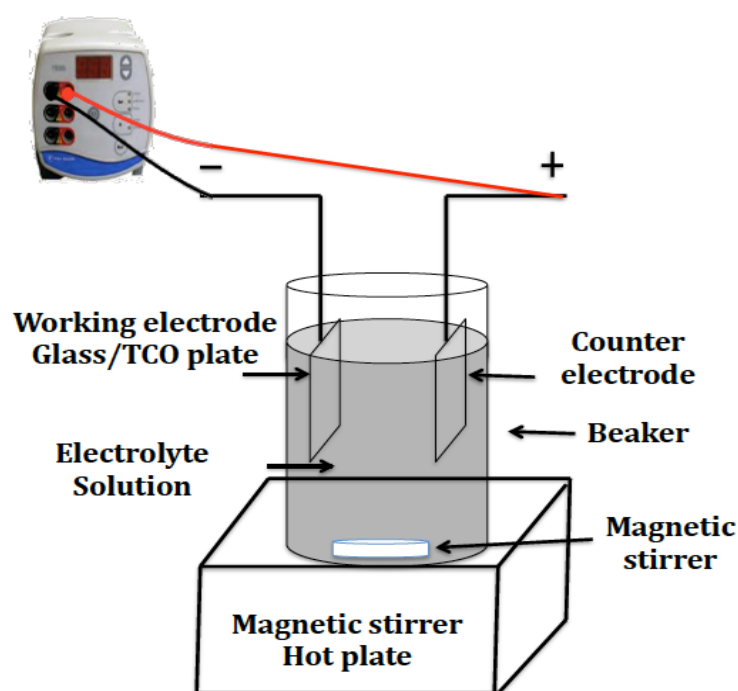


**Figure 2. 1** The schematic of the two-electrode electrodeposition set up

#### 2.2.4 Hydrothermal Method

The hydrothermal method can be used for synthesis of the materials. The key factors to conduct the hydrothermal process are solvent, temperature, pressure and chemical composition of precursors. As a self-evident word, “hydro” and “thermal” mean water and heat respectively. There are plenty of definitions recommended by different scientists for hydrothermal method. As the general description, hydrothermal growth means any heterogeneous chemical reaction in existence of aqueous or nonaqueous solvent where the temperature is kept above room temperature and higher than 1 atm in a closed system. Different properties are observed for hydrothermal solvents at above 100 °C and 1 atm and at critical point, so it is important to know the different properties of the used solvent under hydrothermal conditions.

As the advantage of this method, one can mention the large area good-quality sample production with a good control over their composition. Hydrothermal method also has some disadvantages such as the use of overpriced autoclaves.

In addition to the above mentioned deposition techniques some other methods are also used to deposit different layers of the ETA solar cells. Atomic layer deposition is a common method for  $\text{CuInS}_2$ ,  $\text{Al}_2\text{O}_3$  and  $\text{In}_2\text{S}_3$  compounds [1]. Electrodeposition is almost used for all layers in ETA solar cells such as  $\text{CuSCN}$  [2,3,4],  $\text{CdHgTe}$  [5],  $\text{CdSe}$  [6],  $\text{ZnTe}$  [7],  $\text{ZnO}$  [8-10] and  $\text{CdTe}$  [11]. Ion layer gas reaction is a good alternative method for  $\text{CdS}$ ,  $\text{In}_2\text{S}_3$ ,  $\text{Cu}_2\text{S}$  and  $\text{CuInS}_2$  deposition. Chemical bath deposition technique is used for the majority of chalcogenides such as  $\text{CdS}$ ,  $\text{CdSe}$ ,  $\text{PbS}$ , and chalcopyrite materials like  $\text{CuInSe}_2$ . For  $\text{TiO}_2$  [12] and  $\text{ZnO}$  [13] compact layers on the TCO prior to the n-type nano structured layers, spray pyrolysis can be used in order to avoid the short circuit between TCO and p-type layer.

## **2.3 Sample Preparation**

The details of the preparation procedures of each thin film layers used in the ETA structures investigated in this study are introduced in the following sections.

### **2.3.1 Substrate Cleaning**

The glass slides used as the substrates for the thin film layer deposition, were first cleaned by detergent solution in order to remove the coarse dirt off the surface. Later, in order to clean the remained detergent solution on the glass substrates they were rinsed in distilled water. As the second step, to get rid of the organic materials existent on the glass surface, a boiling solution of diluted  $\text{H}_2\text{O}_2$  30% in water was used which causes the organic dirt's to be converted to water-soluble compounds. Finally the substrates were rinsed in hot boiled water. All these steps were performed in ultrasonic cleaner environment and the cleaned glass substrates were kept in methanol. FTO coated transparent glass substrates were cleaned by detergent and acetone solution successively. Later to remove the spots remained on the surface, the

substrates were cleaned by methanol or ethanol solution. Finally the FTO substrates were immersed and kept in isopropanol solution to remove the dirtiness remained on the surface. All these steps were done in ultrasonic cleaner environment each for ~15 minutes. Before the deposition process, the substrates were dried with blowing nitrogen gas.

## 2.3.2 TiO<sub>2</sub> Thin Film Deposition

### 2.3.2.1 Sputtered TiO<sub>2</sub> Thin Film

The TiO<sub>2</sub> thin films were deposited by using the sputtering system, with 2-inch diameter target and 10 cm target-substrate distance, for 2 hours run time with different RF powers (50 W, 60 W, 80 W, 100 W and 120 W) while the substrate temperature was kept at 200 °C. Ar gas was introduced into the deposition chamber as the sputtering gas and evacuated through the end of the chamber. TiO<sub>2</sub> films were deposited onto glass and FTO coated glass substrates with successive runs using the same parameters in order to have thicker films. It is observed that each run increases the thickness of the film only in the range of 5-10 nm. The deposition parameters for different sets of sputtered TiO<sub>2</sub> are given in Table 2.1.

**Table 2. 1** The deposition parameters of sputtered TiO<sub>2</sub> thin films

Sputtered TiO <sub>2</sub>	Power (Watt)	Time (minutes)	Deposition Temperature
Set 1 (single run)	50 W	120 min	200 °C
Set 2 (single run)	60 W	120 min	200 °C
Set 3 (single run)	80 W	120 min	200 °C
Set 4 (single run)	100 W	120 min	200 °C
Set 5 (single run)	120 W	120 min	200 °C
Set 6 (successive run)	120W/120W	120min/120min	200 °C

### 2.3.2.2 Spin Coated TiO<sub>2</sub> Thin Films

Spin coated nano-porous TiO<sub>2</sub> films were deposited using a low viscous paste composed of terpineol, ethyl cellulose and a commercial TiO<sub>2</sub> dispersion “Degussa VP Disp CE 2730X (30% wt. TiO<sub>2</sub> in isopropanol)”. Ethyl cellulose was first dissolved in isopropanol and mixed with the TiO<sub>2</sub> dispersion. This mixture was homogenized by a magnetic stirrer and subsequently ultrasonic treatment was applied using an ultrasonic bath for 15 minutes. After addition of terpineol and repeating homogenization, isopropanol was evaporated by a rotary evaporator at 40 °C and the final paste was stirred for three days for further homogenization. Ratios of the ingredients are fixed for every deposition which is 2:1:28 for TiO<sub>2</sub>, ethyl cellulose and terpineol, respectively. This formulation is a modified screen printing paste used for mostly dye sensitized solar cells [14]. Resulting low viscous paste is used for spin coating on bare glass and TCO coated glass substrates at 2000, 5000, 8000, 2000/5000, 2000/8000 and 5000/8000 rpm for 1 min and only for 1 run time in the clean room environment. The coating at the spinning rate of 2000/5000 was done first at 2000 rpm proceeded by 5000 rpm each for 30 sec and total time of 1 min. After drying the substrates at 120 °C for 5 minutes, these films were heat-treated for 30 min in an oven at 450 °C to obtain the anatase phase of TiO<sub>2</sub>. The deposition parameters of the spin coated TiO<sub>2</sub> thin films are given in Table 2.2

**Table 2. 2** The deposition parameters of spin coated TiO<sub>2</sub> thin films

Spin Coated TiO <sub>2</sub>	Time (minutes)	Drying (Time/Temperature)	Heat-treatment (Time/Temperature)
2000 rpm	1 min	5 min/120 °C	30 min/450 °C
5000 rpm	1 min	5 min/120 °C	30 min/450 °C
8000 rpm	1 min	5 min/120 °C	30 min/450 °C
2000/5000 rpm	30sec-30sec	5 min/120 °C	30 min/450 °C
2000/8000 rpm	30sec-30sec	5 min/120 °C	30 min/450 °C
5000/8000 rpm	30sec-30sec	5 min/120 °C	30 min/450 °C

### **2.3.2.3 Electrochemical Anodization of TiO<sub>2</sub> Nanotube Arrays**

TiO<sub>2</sub> nanotube arrays (TNAs) were prepared by subjecting a titanium metal to electrochemical anodization process. When a 500 nm sputtered Ti film was subjected to anodization in a highly conductive electrolyte, 0.3% NH<sub>4</sub>F in ethylene glycol (EG) + 4% H<sub>2</sub>O, with anodization voltage about 40 V, a drop in current was observed in the first several seconds. This drop in current is due to the rapid creation of passivating oxide layer named barrier layer. In fact the nanotube formation is initiated with formation of the barrier layer by field-assisted oxidation. The following step is the pit formation due to the dissolution of field-assisted oxide. The pores grow deeper in Ti film due to the strong electric field at the pore bottoms. The metal-oxide interface moves into Ti film due to equilibrium between the field-assisted oxidation and field-assisted oxide dissolution at the metal/oxide interface and the oxide/electrolyte interface respectively. By penetrating the barrier layer deeper in Ti, the strong electric field affects the un-anodized metal layer, which exists in the walls and as the result due to the oxidation and dissolution processes the nanotubes grow [15]. The as-anodized TNAs are amorphous. In order to have the semiconductor properties the TNAs must be annealed in an oxygen environment up to temperatures around 500 °C for one hour.

### **2.3.2.4 Hydrothermal Growth of TiO<sub>2</sub> Nanowire Arrays**

TiO<sub>2</sub> NWs were synthesized on FTO substrates by hydrothermal growth method. Vertically oriented small diameter NWAs were grown with solution containing 5ml DI water, 2.5 ml HCl, 2.5 ml acetic acid and 0.2 ml titanium butoxide, where the solution lacking acetic acid generates separated large diameter NWAs. The solution was kept into a teflon vessel and the FTO substrates were placed with angle in the vessel. Later this vessel was placed into a metallic container to tolerate the high pressures. This set up was put in an oven for 4 hours at a temperature of around 180 °C. The obtained rutile TiO<sub>2</sub> NWAs were rinsed with water and methanol and dried with nitrogen flow [15].

### 2.3.3 CdTe Thin Film Deposition

#### 2.3.3.1 Sputtered CdTe

The RF sputtering conditions and parameters used for the deposition of the CdTe thin films are given in Table 2.3. CdTe target source of 99.999% purity with 3-inch in diameter was used. The target and the substrate distance was 15 cm. As the first run, sputtered CdTe thin films were prepared with RF Power of 70 Watt and the substrate temperature of 100 °C for two different deposition times of 45 and 60 minutes. Later another set of CdTe films were deposited at the substrate temperature of 200 °C, which were post annealed at 300 °C for 30 minutes to have better crystalline structure. CdTe thin films were also coated at a substrate temperature of 300 °C (P=70 W, and t= 60 min deposition time), which was also post annealed at 350 °C for 30 minutes. Thicker CdTe films were coated with the same deposition parameters for 110 min. For some of the samples the CdCl<sub>2</sub> treatment of 5 second immersion of the as-deposited samples in a saturated CdCl<sub>2</sub>/methanol solution was applied.

**Table 2. 3** The deposition parameters of the sputtered CdTe thin films

CdTe	Power (Watt)	Time (minutes)	Deposition T (°C)	Annealing time (30 minutes) T (°C)
Set1	70 W	45 min	100 °C	-
Set2	70 W	60 min	100 °C	-
Set3	70 W	60 min	200 °C	300 °C
Set4	70 W	60 min	300 °C	350 °C
Set5	70 Watt	110 min	300 °C	350 °C



### 2.3.3.2 Electrodeposited CdTe

The electrodeposition of CdTe on FTO/TiO<sub>2</sub> was carried out in aqueous and non-aqueous solutions. For aqueous solution different recipes were examined with three-electrode ED method, which is given in Table 2.4. The reference electrode such as Ag/AgCl may cause problems such as leakage of the Ag<sup>+</sup> ions into the solution bath, which reduces the efficiency of solar cells. Due to the mentioned reason, two electrode ED system was used in this study for device preparation.

The non-aqueous solution was prepared by solving Cadmium Solphate (0.5M) and TeO<sub>2</sub> (0.02 M) in EG using magnetic stirrer in two-electrode ED method, where FTO/TiO<sub>2</sub> and platinum are working and counter electrodes respectively. Hydrochloric acid was added to the solution to adjust the PH value to 1.5. The solution was kept at 140°C and the voltage was varied between 1.5 and 6 V such that for thicker underlayer films higher voltages were applied. It was followed by CdCl<sub>2</sub> treatment of 5 second immersion of the as-deposited samples in a saturated CdCl<sub>2</sub>/methanol solution. Finally heat treatment was applied to the CdTe layer, which resulted a better interfacial intermixing of CdTe absorber with n-type TiO<sub>2</sub> layers. Both CdCl<sub>2</sub> treatment and annealing increases the grain size by eliminating the defects and discontinuities, which result the lower recombination probability or charge carriers trapping.

**Table 2. 4** The ED parameters of CdTe thin films

Recipe 1	CdSO <sub>4</sub> 0.5 M	TeO <sub>2</sub> 0.5 mM	Annealed at 350 °C	Without CdCl <sub>2</sub> Treatment
Recipe 2	CdSO <sub>4</sub> 0.5 M	TeO <sub>2</sub> 0.5 mM	Annealed at 350 °C	With CdCl <sub>2</sub> Treatment
Recipe 3	Cd(NO <sub>3</sub> ) <sub>2</sub> 0.5 M	TeO <sub>2</sub> 0.5 mM	As-Grown	Without CdCl <sub>2</sub> Treatment
Recipe 4	Cd(NO <sub>3</sub> ) <sub>2</sub> 0.5 M	TeO <sub>2</sub> 0.5 mM	Annealed at 350 °C	Without CdCl <sub>2</sub> Treatment
Recipe 5	Cd(NO <sub>3</sub> ) <sub>2</sub> 0.5 M	TeO <sub>2</sub> 0.5 mM	Annealed at 350 °C	With CdCl <sub>2</sub> Treatment
Recipe 6	CdSO <sub>4</sub> 0.5 M	TeCl <sub>2</sub> 0.5 mM	As-Grown	Without CdCl <sub>2</sub> Treatment
Recipe 7	CdSO <sub>4</sub> 0.5 M	TeCl <sub>2</sub> 0.5 mM	Annealed at 350 °C	Without CdCl <sub>2</sub> Treatment
Recipe 8	Cd(NO <sub>3</sub> ) <sub>2</sub> 0.5 M	TeCl <sub>2</sub> 0.5 mM	Annealed at 350 °C	With CdCl <sub>2</sub> Treatment

### 2.3.4 ZnTe and ZnSnTe Thin Film Deposition

Different sets of sputtered ZnTe thin film were sputtered on FTO/TiO<sub>2</sub>/CdTe and glass substrates, where the ZnTe target of 3-inch in diameter with 99.999% purity and was used. The target and the substrate distance was 15 cm. The sputtering RF power, substrate temperature and deposition time were applied as P=75 W, T=300<sup>0</sup> and 60 min respectively. The samples were annealed at T=350 °C for 30 minutes to improve the crystallinity.

As mentioned in Section 1.4.3, in order to enhance the conductivity of ZnTe it was doped with SnTe. Using a three magnetron DC/RF sputtering system, ZnSnTe films were sputtered by sequential sputtering from compound targets of SnTe and ZnTe to decrease the resistivity of ZnTe samples. The ZnSnTe deposition was done in argon

atmosphere at the substrate temperature of about 300 °C and DC and RF powers of 25 W and 75 W respectively, for SnTe and ZnTe on FTO/TiO<sub>2</sub>/CdTe and glass substrates. Finally the films were annealed at T=350 °C to enhance the crystallinity of the ZnSnTe films. The thickness values for ZnTe and SnTe in ZnSnTe sample are given in Table 2.5.

**Table 2. 5** Thickness values of ZnTe and SnTe (in the ZnSnTe) thin films

Sample thickness	ZnTe thin film	SnTe thin film
	360 nm	11 nm

## 2.4 General Description of the Characterization Methods

The different thin film layers deposited with different deposition techniques, for the two-component Glass/FTO/TiO<sub>2</sub>/CdTe/Au and three-component Glass/FTO/TiO<sub>2</sub>/CdTe/ZnSnTe/In ETA solar cell devices were characterized using UV-Vis absorption/transmittance, XRD, SEM, AFM and BET measurements. The solar cell structures were characterized by dark and illuminated I-V measurements.

### 2.4.1 UV-Vis Spectroscopy

Through the interaction between the semiconductors and light, various processes occur such as absorption, reflection, transmission and scattering. Optical measurements are contactless and non-destructive techniques. Different optical characterization methods exist such as optical microscopy, optical absorption, photoluminescence and raman spectroscopy. Optical transmission, absorption and reflection are the most used techniques for determining the band structure of samples. The absorption happens through different transitions such as band to band, inter conduction/inter valence band, valence to donor, acceptor to conduction band, donor to conduction/acceptor to conduction band and donor to acceptor transitions. The

mentioned transitions, which are shown in Figure 2.2, [16] give information about the absorption coefficient ( $\alpha$ ).

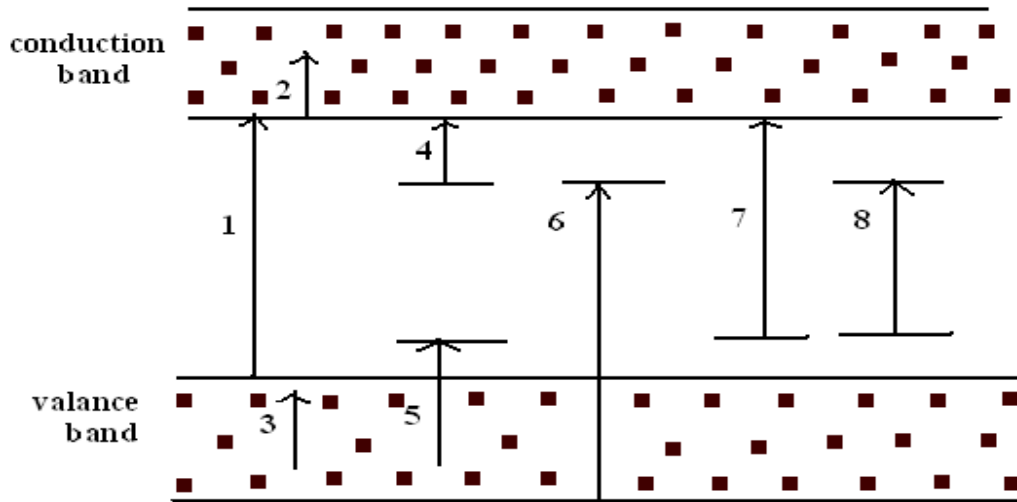


**Figure 2. 2** Various absorption processes in the semiconductors: (1) Band to band, (2) Interconduction band, (3) Intervalence band, (4) Donor to conduction band, (5) Acceptor to valance band, (6) Valance band to donor, (7) Acceptor to conduction band, and (8) Donor to acceptor transitions [16]

The energy of the incident photon specifies the kind of absorption. If this energy is greater than the band gap of the material, then the electron will excite from the valance band to the empty states of the conduction band, which is called the fundamental absorption and significantly affects the absorption coefficient. For photon energies lower than the band gap energy the absorption occurs by excitons (electron-hole bound pairs) between the conduction/valance band states (band states), acceptor/donor states (impurity or defect states). For low energy inter band transitions, continuous absorption takes place.

Depending on the position of the minima and maxima of the conduction and valance band in brillouin zone, the band-to-band transition is categorized as direct and indirect absorption respectively. For both direct and indirect transitions, the momentum conservation law must be conserved as it is illustrated in Figure 2.3 [17]. The maxima and minima of the conduction and valance band are at the same momentum vector ( $kr$ )

value for direct band gap semiconductor (direct transition) and if the maximas are not in the same wave vector and a phonon is a part of this momentum conservation it is named the indirect band gap semiconductor (indirect transition). Indirect transitions because of accompanying the phonons ( $q$ ) result weak absorptions compared to direct ones [18].

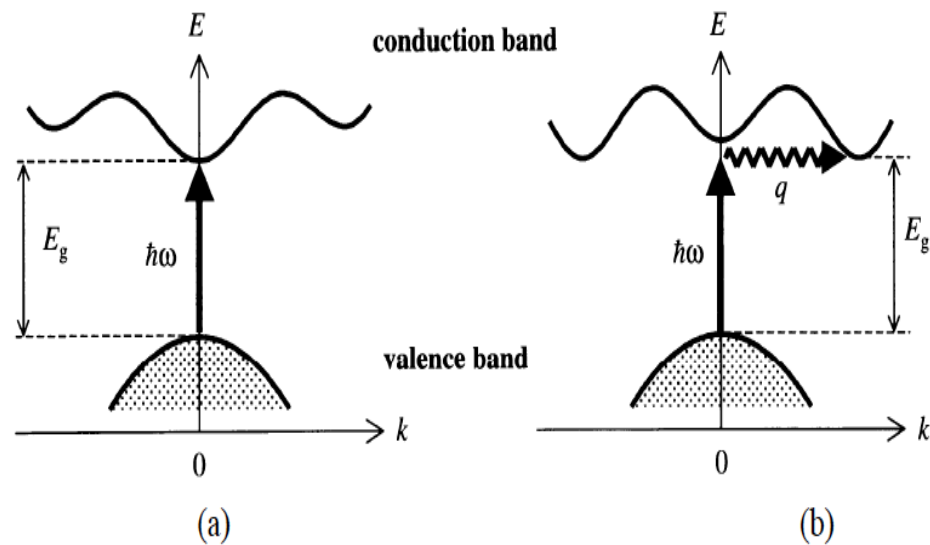


**Figure 2. 3** Illustration of (a) Direct band gap, and (b) Indirect band gap transitions [17]

One can find the absorption coefficient from;

$$\alpha(h\nu) = A \sum p_{if} n_i n_f \quad (2.1)$$

where  $A$ ,  $P_{ij}$ ,  $n_i$  and  $n_f$  are constant, transition probability from initial to final state, density of electrons in initial states and density of empty states in the final states respectively. The energy of electron in conduction band and holes in valance band can be found by;

$$E_e = \frac{\hbar^2 k^2}{2m_e^*}, \quad E_h = \frac{\hbar^2 k^2}{2m_h^*} \quad (2.2)$$

the direct transition is given by;

$$h\nu - E_g = \frac{\hbar^2 k^2}{2m_e^*} + \frac{\hbar^2 k^2}{2m_h^*} = \frac{\hbar^2 k^2}{2m_r^*} \quad (2.3)$$

where the reduced effective mass is given by  $m_r^* = \frac{m_e^* m_h^*}{m_e^* + m_h^*}$ . Also the density of states is given by;

$$N(E)dE = (2\pi^2 \hbar^3)^{-1} (2m^*)^{3/2} E^{1/2} dE \quad (2.4)$$

Using the above two equations, one can find the absorption coefficient of the direct transition as;

$$\alpha(h\nu) = A(h\nu - E_g)^{1/2} \quad (2.5)$$

Where A is the constant and  $E_g$  is the band gap energy of the sample material [18,19]. For indirect transition, phonon absorption or emission is contributed and the total absorption coefficient for  $h\nu > E_g + E_p$  can be found by;

$$\alpha(h\nu) = \alpha_a(h\nu) + \alpha_e(h\nu) \quad (2.6)$$

where  $\alpha_a(h\nu)$  and  $\alpha_e(h\nu)$  are respectively the absorption coefficient for the phonon absorption and phonon emission cases.

For phonon absorption case the absorption coefficient is given by [20]

$$\alpha_a(h\nu) = \frac{A(h\nu - E_g + E_p)^2}{\exp\left(\frac{E_p}{K_B T}\right) - 1} \quad (2.7)$$

And for the phonon emission case, the absorption coefficient is expressed as;

$$\alpha_e(h\nu) = \frac{A(h\nu - E_g - E_p)^2}{1 - \exp\left(\frac{E_p}{K_B T}\right)} \quad (2.8)$$

where  $E_p$ , T and  $K_B$  are respectively the phonon energy, absolute temperature and boltzman constant.

Also by using the transmission (T) and reflection spectra, the absorption coefficient ( $\alpha$ ), is calculated by;

$$T = \frac{(1 - R)^2 \exp(-\alpha d)}{1 - R^2 \exp(-2\alpha d)} \quad (2.9)$$

where I, d and  $I_0$  are light intensity, thickness of the sample material and incident light intensity respectively. For the large ( $\alpha d$ ) values, the expression is clarified as:

$$T = (1 - R)^2 \exp(-\alpha d) \quad (2.10)$$

By neglecting the reflection term, the expression is simplified as:

$$T = \exp(-\alpha d) \quad (2.11)$$

The room temperature transmission measurements were performed for the optical characterization of the films deposited on glass substrates to determine the absorbance, transmittance and band gap of the deposited films. The absorption coefficient is calculated by using the relation;

$$\alpha = -\left(\frac{1}{d}\right) \ln\left(\frac{I}{I_0}\right) \quad (2.12)$$

Where d, I and  $I_0$  are respectively the thickness, intensity of transmitted light and intensity of the incident light perpendicular to the surface of the sample [21]. For a direct band gap, the absorption coefficient  $\alpha$ , according to the following formula is related to the light frequency;

$$\alpha h\nu = A(h\nu - E_g) \quad (2.13)$$

where A is an energy-independent constant and  $E_g$  is the forbidden band gap energy [18,22]. Therefore, from the plot of  $(\alpha h\nu)^2$  versus  $h\nu$  (Tauc plot) the band gap values can be defined by extrapolation of the straight line on the energy axis.

#### 2.4.2 X-ray Diffraction

X-ray diffraction (Rigaku Miniflex system) equipped by Cu- $K_\alpha$  radiation with an average wavelength of 1.54059 Å was used to determine the crystallinity (crystalline,

polycrystalline or amorphous), the phases present in the structure, crystallographic orientation, lattice parameters and also detecting the defects and stress, which exist in the structure of the deposited films. Scan parameters included a 2°/min scan speed and typical 2θ scan range between 10°-70°/90°.

The X-ray region is supposed to be in the 0.1-100 Å range of the electromagnetic spectrum, so the best way to have information about the crystal structure of the deposited films is to use X-ray having the wavelength comparable to atomic distances. X-ray electromagnetic waves with energies between 200 eV-1MeV are used for structural parameter identification by interacting with sample material. X-rays can be absorbed, emitted and reflected through interaction with material and as the result of interaction the diffraction patterns are formed. The falling monochromatic X-ray beams onto the deposited film must have the same phase in the direction, to be observed. Crystals are made from unit cells with dimensions named lattice parameters. X-ray radiation causes diffraction inside the sample in different directions, which is an evident of periodic atomic structure of the crystals in the samples. The incident beam of X-rays before leaving the crystal will interfere with the atomic planes of the crystal. This interference can be constructive or destructive in accordance with their phase difference.

Different condition must be satisfied to have diffraction patterns in the way that the angle of incident and diffracted beams with reflecting planes be equal. As another condition the Bragg law must be satisfied. Using Bragg's Law it is possible to identify the lattice parameter of crystalline. Bragg's law proposes that the constructive interference happens only for phase difference comparable to wavelength multiplied by an integer [23]. The maximum beam diffraction by atomic planes are given by the Bragg equation as:

$$n\lambda = 2d\sin\theta \quad (2.14)$$

where n is the positive integer and express the order of reflection maximum. Physical parameters  $\lambda$ , d,  $\theta$  are respectively the wavelength of incoming X-rays, distance between the lattice planes in crystal and the angle between the incident wave and scattering planes expressed as the angle of reflection. Diffraction happens only for constructive interference condition of Bragg's law since for the destructive condition



case the waves negate each other. The Bragg diffraction pattern is presented in Figure 2.4.

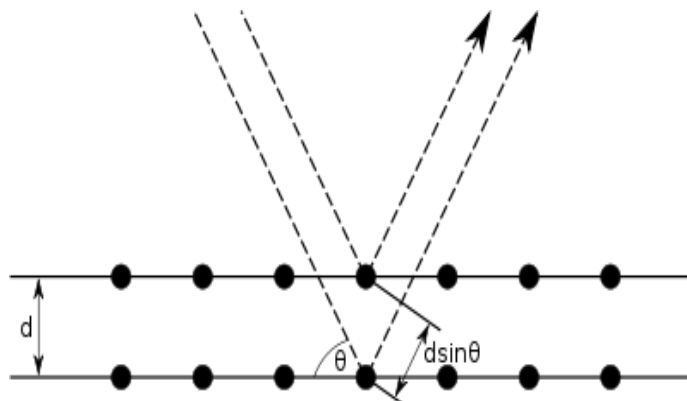


**Figure 2. 4** Bragg diffraction of X-rays from parallel planes

The obtained XRD patterns (peak positions, intensity, peak-width and shape) were interpreted by a computer-based software with ICDD database including the well known diffraction patterns of  $\text{TiO}_2$ , CdTe, ZnTe and SnTe. This comparison of the peaks was done by considering the relative intensities of peaks and the peak positions at  $2\theta$  values. Powder phase identification was done by comparing the peak positions and inter-planar spacing with the standards JCPDS (joint committee on powder diffraction standards), which is provided by XRD suppliers. The XRD system schematic is shown in Figure 2.5.

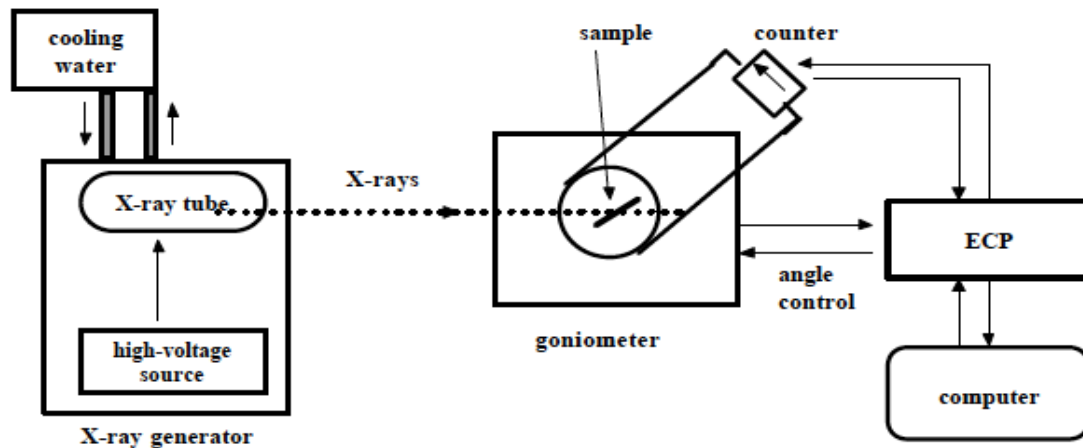


**Figure 2. 5** The schematic of the XRD system [24]

The average microcrystalline grain size  $D$  was estimated from the powder XRD pattern using Scherrer's formula [25] expressed as;

$$D = \frac{K\lambda}{\beta \cos\theta} \quad (2.15)$$

where  $K$  is the shape factor equal to 0.94 [26],  $\lambda$  is the wavelength of X-rays,  $\beta$  is defined as the diffraction peak width at half height maximum (FWHM) and  $\theta$  is the diffraction angle (Figure 2.4).

### 2.4.3 Atomic Force Microscopy

Another method to study the surface of the thin film sample is the Atomic Force Microscopy, which can give the high-resolution images of surface topography such as surface roughness. To scan the surface of the thin film sample, AFM is equipped with a fine probe made from silicon, silicon nitride and silicon oxide placed at the end of the cantilever, which is illustrated in Figure 2.6 [27].

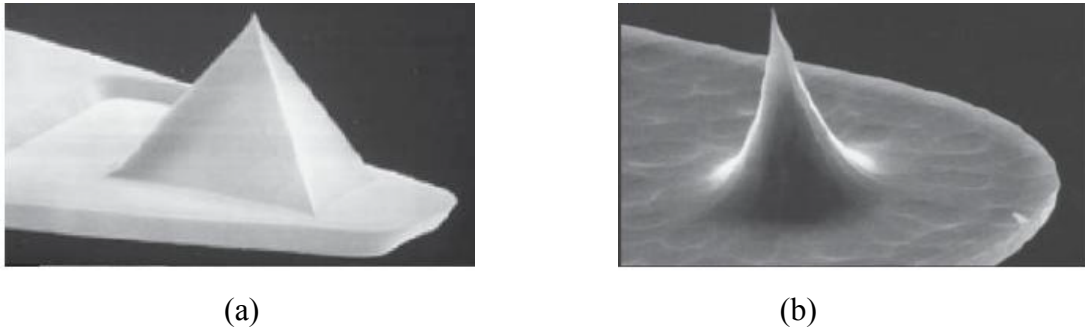


**Figure 2. 6** SEM images of AFM probe a) With Pyramidal probe b) With Conical high aspect ratio probe [28]

Based on the usage of AFM, either the sample or cantilever can be fixed and the other one is moved. While the cantilever is scanned through the sample, a reflective laser with a layer of gold or aluminum, which is localized at the backside of the cantilever, is used to monitor the movement of cantilever. As the sample is scanned, the data is recorded by reflection of the laser onto different parts of the photodiode and so the picture is constructed. In Figure 2.7 an example of the schematic of an AFM setup is illustrated.

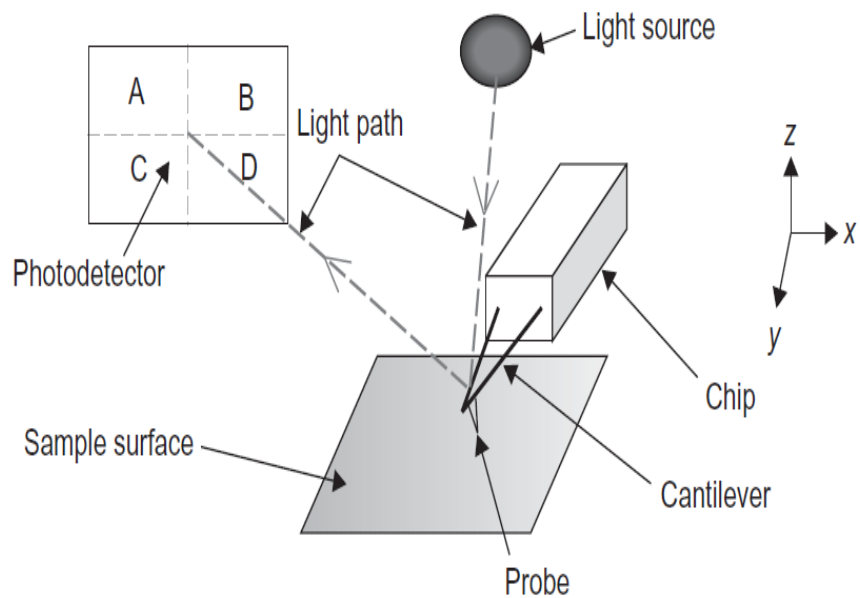


**Figure 2. 7** The schematic of an AFM setup [26]

In AFM measurements, the cantilever can be scanned through the surface of the samples by different modes like contact, non-contact and a combination of these two modes. For contact mode the tip is pulled over the surface, which may work good for some samples while for others due to the adhesion force between the sample and tip may damage both the tip and sample. For the non-contact mode, where there is not any contact between the surface of the sample and tip, the van der Waals force is the reason of displacing the cantilever. In this mode, low-resolution image will be obtained since the van der Waals force causes weak interaction. In the other method named tapping mode, which is the combination of these two, the cantilever is oscillated around its natural frequency near the surface.

#### **2.4.4 Scanning Electron Microscopy and Energy Dispersive Spectroscopy**

Common used microscopy techniques to characterize the samples are optical microscopy, electron microscopy and scanning probe microscopy [18]. Scanning electron microscopy and transmission electron microscopy are the most common routes to provide morphological, structural, compositional properties and defects in the structure of the sample. SEM gives images of samples with higher magnification than traditional optical microscopes. Optical microscopy does not need to have vacuumed environment and it also has some other advantages such as easy sample preparation [18]. SEM system can give magnification up to 100,000X, while the optical microscopes are confined to about 1,500X magnifications. Since the wavelength of electrons is much smaller compared to the wavelength of photons ( $\lambda_{\text{electron}} = 0.01\text{nm}$ ,  $\lambda_{\text{photon}} = 400\text{ nm}-700\text{ nm}$ ), where this can cause having much higher depth of field for SEM systems compared to optical microscopes.

The morphology of the film, the surface uniformity, composition of the regions from the film surface, structural, physical and compositional properties and also the grain size of the films can be measured by SEM system. Also using the cross-section image of the device sample, the thickness of different layers, the condition of interfaces and the quality of the layers can be investigated. Scanning probe microscopy (SPM) gives high quality images of the sample surface on the atomic scale. The image is the result of the interaction between mechanically moved fine probe and the sample surface.

A schematic of a typical SEM setup is illustrated in Figure 2.8, which is mainly

composed of the electron gun (to provide electron beam), sample chamber (to provide interaction between the electron beam and sample), scanning coils, lens system, electron collector and cathode ray tube (CRT) display [27]. In the Scanning electron microscopy, a focused accelerated high energetic electron beam ( $\sim 0.1$  nm) is sent to the surface of the material. The electron beam can be provided by the long lasting bright source such as lanthanum hexaboride ( $\text{LaB}_6$ ) source or by a field-emission gun. Different interactions happen between this electron beam and the nuclei or also the electrons of the film. The interaction volume have inverse ratio with atomic number of the sample material [29]. There are number of lenses and scanning coils over the path of electron beam through the sample which as the result of this interaction, scattering gradually decreases the energy of incident electrons. Both elastic and inelastic scattering diverts the incoming electrons path by nuclei of atoms calling backscattered electrons and produces various indications such as emitting secondary electrons, Auger electrons, characteristic X-rays and electron-hole pairs [18]. Even though generally the secondary electrons are identified and used for figuring out an image, also the x-rays and backscattered electrons can be used to have information around the image of the sample. Finally the secondary electrons are repelled through the detector and photomultiplier, driving the CRT to have the image of the sample. The secondary electron, X-rays and back scattered electrons provided by the interaction between the incident electrons and sample give information about the surface morphology, elemental analysis and composition contrast respectively. The energy of the incident electron given by the accelerating voltage, affects the penetration depth. In fact the high-magnification SEM images are formed by the emission and collecting of the secondary electrons originated by the coming electron beam on the surface of the deposited film, this is called secondary emission mode.

SEM measurements were performed by using a FEI Quanta 400 FEG model scanning electron microscope, which is supplied with energy dispersive X-ray analysis (EDX) component. The beam of energetic electrons inelastically scatters and ionizes the inner shell atoms by giving the required amount of energy, critical ionization energy, to remove an atomic electron. This is called the microanalization mode of SEM. By measuring X-rays energies emitted from the excited sample, which is caused by changing the speed of the bombarded electrons, the elemental composition of the material was recognized for the measured region. In fact by measuring the intensity of

the characteristic X-rays, the elements present in the material were found, where for finding the elemental constituent of material the whole sample area must be scanned. In this technique only those elements with atomic number greater than eleven are determined. Energy dispersive spectroscopy was used in conjunction with SEM to identify the presence of the Zn, Sn and Te elements in the deposited thin ZnSnTe films.

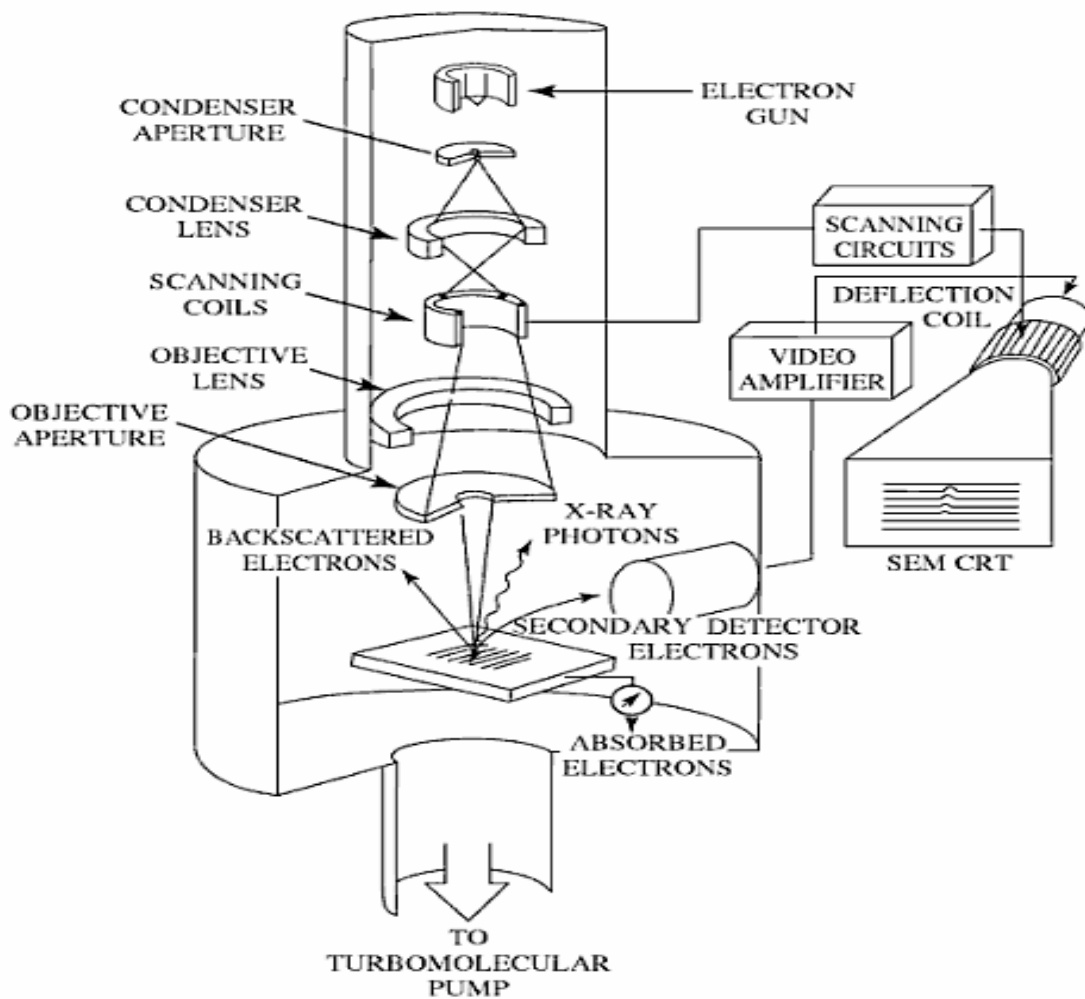


**Figure 2. 8** The schematic of a typical Scanning Electron Microscope [27]

### **2.4.5 Surface Profilometer**

The thicknesses of the CdTe and ZnSnTe thin films deposited onto glass substrates were measured by DEKTAK 3030ST profilometer with resolution about 10 to 20 Angstrom. The measurements were performed by scanning the stylus over the glass substrates to the deposited film surface for different film regions in order to see whether the film is homogeneous or not. It measures the surface texture and film thickness respectively below 10's of nm and up to 131 microns. This DEKTAK system has stylus with 12.5 micron diameter and a camera in order to locate the stylus on the region, where the thickness measurements were done. The stylus is moved electromechanically on the surface of the film with a force in the range of 1-50 mg [24].

### **2.4.6 Electrical Measurements**

#### **2.4.6.1 The Metallic Evaporation System**

PVD techniques include some deposition techniques such as the sputtering and evaporation. The evaporation systems consist of different parts such as holder, heating source and shutter. Heating source can be electron or laser beam and thermally heated crucible. Metallic aluminium, indium and gold contacts were evaporated on device structures as metallic contact. The mask used for the metallic contact evaporation has the point circle contact geometries with an area of (1mm) x (1mm).

The Nanotech thermal evaporation system for metallic contact evaporation has the bell-jar body illustrated in Figure 2.9. The lowest pressure to start the deposition was  $10^{-5}$  Torr through the turbo pump. The metal piece for evaporation was placed in tungsten spiral or molybdenum boat and was manually heated by a self-restrained variac. The distance between the spiral or boat and sample substrate Cu holder was around 10 cm. Finally to evaporate the moisture on the surface of contacts, they were annealed under nitrogen flow at 100 °C for 30 minutes.

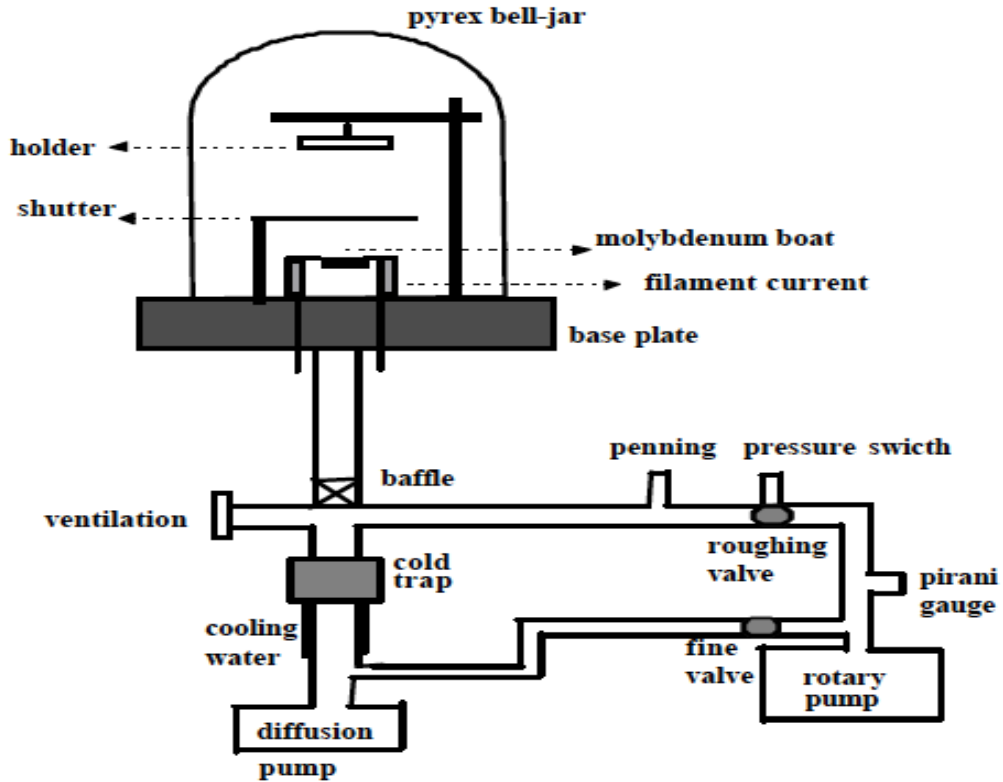


Figure 2. 9 The schematic of the metal contact evaporation system [24]

#### 2.4.6.2 Conductivity Measurements

One of the important techniques to identify the film quality is the conductivity measurement. The conductivity of the deposited thin films depends on both structural characteristics and crystallinity. The room temperature dark conductivity measurement of TiO<sub>2</sub>, CdTe and ZnSnTe thin films were performed by applying the voltage V to two dot metal contact electrodes and so the resulting electrical current passing through the film was measured. Also for the photoconductivity measurements, the thin film samples were illuminated by the solar simulator with AM 1.5 solar radiation.

The conductivity values were calculated using the following formula:

$$\sigma = \frac{I w}{V l d} \quad (2.16)$$



where the slope of the I-V graph gives the resistance of the films ( $R=V/I$ ),  $w$  is the distance between two metallic dot contact electrodes,  $d$  is the thickness of the deposited thin film and  $l$  is the diameter of the electrodes. For simplicity of the calculations the current density was accepted to be uniform over the whole cross section.

The reliability of these measurements strongly depends on the ohmic behavior of the metal contacts in order to omit the parasitic impedance on the structure. The ohmic behavior of the contacts was controlled by the linear variation of the I-V characteristics.

Owing to high electrical conductivity values of TCOs, which is almost near-metallic conductivity, they are suitable to be used as the wide band gap current collectors in solar cells.

#### **2.4.6.3 Current- Voltage (I-V) Measurements**

To study the electrical properties of the Glass/TCO/TiO<sub>2</sub>/CdTe/Au and Glass/TCO/TiO<sub>2</sub>/CdTe/ZnSnTe/In devices, room temperature dark current-voltage characteristics were measured to consider the rectifying behavior of different layers. Current-voltage measurements were also used to have fundamental information about the performance of a solar cell. The schematic of a measurement set up is illustrated in Figure 2.10.

A constant voltage was applied between the back and front contacts of the device structure and the current flow across the device was measured by a Keithley 2400 electrometer. The performance of the solar cell device in dark and under standard light intensity of 100 mW/cm<sup>2</sup> with an air-mass 1.5 (AM1.5) light spectrum is measured by the similar set-up. A typical current-voltage characteristic for a solar cell in dark and under illumination is given in Figure 2.11. One can observe a shift for the illuminated case due to the amount of generated photocurrent. In order to determine the basic PV parameters like the solar cell efficiency ( $\eta$ ), fill factor (FF), open circuit voltage ( $V_{oc}$ ), short circuit current density ( $J_{sc}$ ) and output power [30-58], the I-V data were fed into a Labview programme.

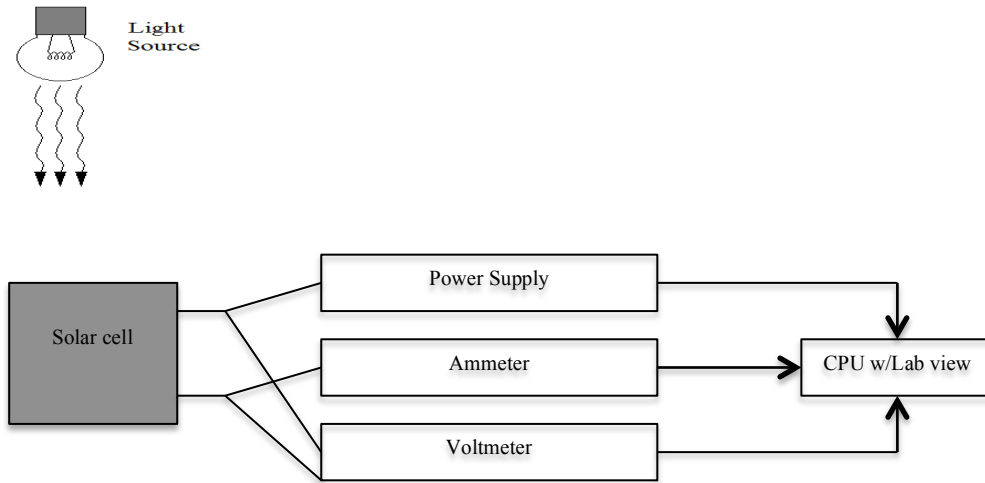


**Figure 2. 10** The schematic of the current-voltage measurement setup

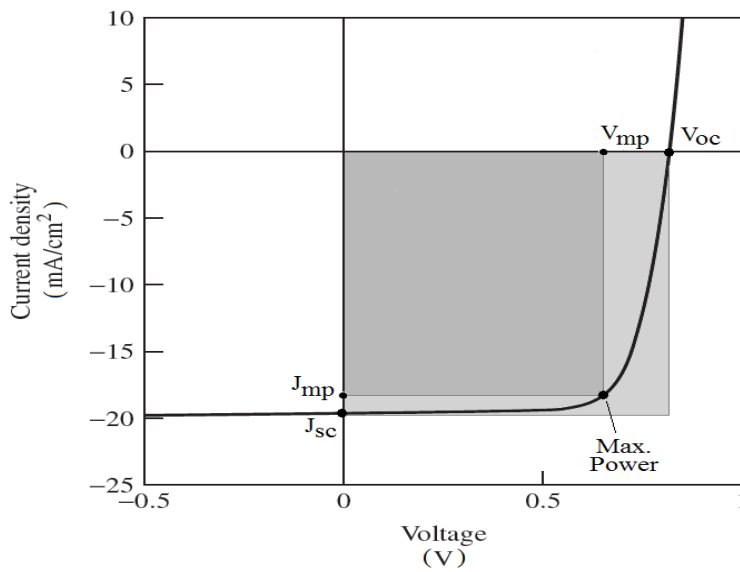


**Figure 2. 11** The typical current-voltage variation of a solar cell in dark and under illumination

Short circuit current ( $I_{sc}$ ) is the current through the junction under illumination without applying any external bias. Short circuit current is proportional to both the intensity of illumination and the material properties and also the minority carrier lifetimes and diffusion lengths. The open-circuit voltage ( $V_{oc}$ ) is defined as the voltage

across the illuminated junction when the photo current value is zero. At both  $I_{sc}$  and  $V_{oc}$  values no power is delivered from the cell to the load and consequently no power is obtained. The maximum output power can be found by the condition  $\frac{\partial P}{\partial V} = 0$  [59] at any point between  $J_{SC}$  and  $V_{oc}$  which the output power is obtained. The  $J_{MP}$  and  $V_{MP}$  are current and voltage values at the maximum output power point. Fill Factor is the ratio of the maximum output power to the product of  $V_{oc}$  and  $J_{SC}$ , which is the “squareness” of the J-V curve expressed as;

$$FF = \frac{(V_{MP})(J_{MP})}{(V_{OC})(J_{OC})} \quad (2.17)$$

The cell efficiency is the ratio of the maximum power of the solar cell to the incident power due to solar radiation which can be found from;

$$\eta (\%) = \frac{(V_{OC})(J_{SC})(FF)}{P_{IN}} \times 100\% = \frac{\text{max power out}}{\text{max power in}} \quad (2.18)$$

The dark current for ideal p-n junction solar cell can be obtained by the Shockley diode equation [60] given as;

$$J = J_0 \left[ \exp\left(\frac{qV}{nkT}\right) - 1 \right] \quad (2.19)$$

where  $J$ ,  $J_0$ ,  $q$ ,  $V$ ,  $k$ ,  $T$  and  $n$  are respectively the current density, saturation current density, electronic charge, applied voltage, Boltzman constant, temperature and ideality factor [60]. By applying the illumination to the cell the light generated current  $J_L$  will be added to the Equation 2.19 as;

$$J = J_0 \left[ \exp\left(\frac{qV}{nkT}\right) - 1 \right] - J_L \quad (2.20)$$

For all the devices series resistance  $R_s$  and shunt resistance  $R_{sh}$  affect the photovoltaic performance of the cell.  $R_s$  is due to the both bulk material and the contacts of the device, where  $R_{sh}$  is due to leakage in the cell such as presence of pinholes. The  $R_s$  and  $R_{sh}$  values are respectively 0 and  $\infty$  for the ideal cell. The  $R_s$  and  $R_{sh}$  are introduced to Equation 2.20 as;

$$J = J_0 \left[ \exp\left(\frac{q(V-JR_s)}{nkT}\right) - 1 \right] + \frac{(V-JR_s)}{nR_{sh}} - J_L \quad (2.21)$$

The ideality factor also called diode factor ( $n$ ), which has the value of unity for ideal junction, which indicates the ideality of the junction. The ideality factor can be larger than unity due to the dominating current transport mechanisms. The value of  $n$  can be extracted from Equation 2.19, which can be expressed as;

$$\ln J = \ln J_0 + \frac{qV}{nkT} \quad (2.22)$$

The  $n$  and  $J_0$  values are extracted from the slope and intercept of the  $\ln J$  versus  $V$  variation for the forward bias. For the above equation the effect of the  $R_s$  and  $R_{sh}$  is neglected.

In general,  $n = 1$  corresponds the pure thermionic emission mechanism, where  $n > 1$  shows the presence of the other conduction mechanisms in junction region to the carrier transport such as recombination and tunneling [61-64].

## 2.5 References

- [1] M. Nanu, J. Schoonman and A. Goossens, *Chem. Vap. Deposition*, 10 (2004), p. 45
- [2] K. Ernst, A. Belaïdi, R. Könenkamp, *Semicond. Sci. Technol.* 18 (2003), p. 475
- [3] B. O'Regan, D.T. Schwartz, *Chem. Mater.* 10 (1998), p. 1501
- [4] K. Tennakone, A.R. Kumarasinghe, P.M. Sirimanne, G.R.R.A. Kumara, *Thin Solid Films*, 261 (1995), p. 307
- [5] M. Neumann-Spallart, G. Tamizhmani, A. Boutry-Forveille and C. Lévy-Clément, *Thin Solid Films*, 169 (1988), p. 315
- [6] M. Skylas-Kazavos and B. Miller, *J. Electrochem Soc.*, 127 (1980), p.869
- [7] M. Neumann-Spallart and Ch. Königstein, *Thin Solid Films*, 265 (1995), p.33
- [8] R. Könenkamp, K. Boedecker, M.C. Lux-Steiner, M. Poschenrieder, F. Zenia, C. Lévy-Clément, S. Wagner, *Appl. Phys. Lett.*, 77 (2000), p.2575
- [9] C. Lévy-Clément, R. Tena-Zaera, MA. Ryan, A. Katty, G. Hodes, *Adv Mater.*, 17(12) (2005), p.1512
- [10] S. Peulon and D. Lincot, *J. Electrochem. Soc.*, 145 (1998), p. 864
- [11] M.P.R. Panicker, M. Knaster and F.A. Kröger, *J. Electrochem. Soc.*, 125 (1978), p. 566–572
- [12] L. Kavan and M. Grätzel, *Electrochim. Acta*, 40 (1995), p.643–652
- [13] B. O'Regan, D.T. Schwartz, S.M. Zakeeruddin and M. Grätzel, *Adv. Mater.*, 12 (2000), p.1263
- [14] S. Ito, T. N. Murakami, P. Comte, P. Liska, C. Grätzel, M. K. Nazeeruddin, M. Grätzel, *Thin Solid Films.*, 516 (2008), p. 4613
- [15] A. Mohammadpour, *Synthesis and Characterization of TiO<sub>2</sub> Nanowire and Nanotube Arrays for Increased Optoelectronic Functionality*, Ph.D. Thesis, University of Alberta, 2014
- [16] P. K. Basu, *Theory of Optical Process in Semiconductors*. Oxford Science Publications, Oxford University Press, 2005
- [17] M. Fox, *Optical Properties of Solids*. Oxford University Press, 2001
- [18] B. G. Yacobi, *Semiconductor Materials: An Introduction to Basic Principles*. Kluwer Academic/Plenum Publishers, London 2002

- [19] H. Karaağaç, Structural, Electrical and Optical Characterization of Ge- implanted GaSe Single Crystal Grown By Bridgman Method, Ms Thesis, Middle East Technical University, 2005
- [20] J. I. Pankove, Optical Process in Semiconductor. Prentice-Hall, London, 1971
- [21] S. M. Sze, Physics of Semiconductor Devices. New York: John Wiley & Sons, 1981
- [22] N. F. Mott and E. A. Davis, Electronic Process in Non-Crystalline Materials Clarendon-Press, Oxford, 1971
- [23] W. H. Bragg and W. L. Bragg, Proceedings of the Royal Society of London. Series A, 88 (1913), p. 428
- [24] K. Yilmaz, Investigation OF InSe Thin Film Based Devices, Ph.D. Thesis, Middle East Technical University, 2004
- [25] B. D. Cullity, Elements of X-ray diffraction, Addison-Wesley Pub, USA, 1956.
- [26] J. I. Langford and A. J. C. Willson, J. Appl. Cryst., 11 (1978), p. 102
- [27] D. K. Schroder, Semiconductor material and device characterization, 3rd ed. ed. [Piscataway, NJ]: IEEE Press Wiley, 2006
- [28] W. R. Bowen and N. Hilal, Atomic force microscopy in process engineering an introduction to AFM for improved processes and products, 1st ed. ed. Burlington, Mass.: Butterworth-Heinemann, 2009
- [29] S. L. Flegler, J. W. Heckmen, K. L. Klomparens, Scanning and Transmission Electron Microscopy, An introduction, Oxford University Press. Oxford, 1993
- [30] K.L. Chopra, S.R. Das, Thin Film Solar Cells, Plenum Press, New York, 1983.
- [31] J. Volger, Phys. Rev., 9 (1950), p.1023
- [32] R.L. Petritz, Phys. Rev., 104, (1956), p.1508
- [33] J.Y.W. Seto, J. Appl. Phys., 46 (1975), p. 5247
- [34] C.H. Seager and G.E. Pike, J. Appl. Phys. Lett., 40 (1982), p. 471
- [35] M.V. Garcia -Cuence, J.L. Morenza and J. Esteve, J. Appl. Phys., 56 (1984), p. 1738
- [36] J.G. Simmons, J. Appl. Phys., 34 (1963), p. 1793
- [37] R. Dalven, Introduction to Applied Solid State Physics, Plenum Press, New York, 1980
- [38] T.J. Coutts, Active and Passive Thin Film Devices, Academic Press, New York, 1978

- [39] D. A. Neamen, Semiconductor Physics and Devices, The Mc-Graw Hill Inc., Chicago, 1997
- [40] E.H. Putley, The Hall Effect and Semiconductor Physics, Dover Publications, New York, 1960
- [41] R.H. Bube, Photoelectronic Properties of Semiconductors, Cambridge Univ. Press, New York, 1992
- [42] D.K. Schroder, Semiconductor Material and Device Characterization, Wiley-Interscience, New York, 1990
- [43] V.K Mathur and R.P. Dahiya, Solid State Electronics, 17 (1974), p. 61
- [44] A. Rose, RCA Rev., 12 (1951), p.362
- [45] J.G. Simmons, DC Conduction in Thin Films, Milk and Boon Ltd., London, 1971
- [46] M.A. Lampert and P. Mark, Current Injection in Solids, Academic Press, New York, 1970
- [47] H.A. Bethe, MIT Radiation Lab. Report, 43-12, 194
- [48] W. Schottky, Naturwiss., 26 (1938), p.843
- [49] C.R. Crowell and S.M. Sze, Solid State Electronics, 9 (1966), p. 1035
- [50] A.S. Grove, Physics and Technology of semiconductor Devices, John Wiley and Sons, New York, 1967
- [51] B.L. Sharma, Metal-Semiconductor Schottky Barrier Junctions and Their Applications, Plenum Press, New York, 1984
- [52] A.M. Goodman, J. Appl. Phys., 34 (1963), p. 329
- [53] B.L. Sharma and R.K. Purohit, Semiconductor Heterojunctions, Pergamon Press, New York, 1974
- [54] U. Dolega, Z. Naturf.,18a (1963), p. 653
- [55] R.H. Rediker, S. Stopek and J.H.R. Ward, Solid State Electron., 7 (1964), p. 621
- [56] P.C. Newman, Electronic Letters, 1 (1965), p. 265
- [57] H.S. Rauschenbach, Solar Cell Array Design Handbook, Van Nostrand Reinhold Comp., New York, 1980
- [58] A.L. Fahrenbruch and R.H. Bube, Fundamentals of Solar Cells, Academic Press, New York, 1983
- [59] K.L. Chopra and I. Kaur, Thin Film Device Applications, Plenum Press, New York, 1984
- [60] A. L. Fahrenbruch and R. H. Bube, Fundamentals of Solar Cells, 1st ed.,

Academic Press, London, (1983)

[61] P. Paul Ramesh, *Materials Lett.*, 34 (3-6) (1998), p.217

[62] Ji-B. Yoo, A. L. Fahrenbruch, R. H. Bube, *J. Appl. Phys.* 68 (1990), p.4694

[63] S. K. Das, *Thin Solid Films*, 226 (2) (1993), p.259

[64] B. L. Sharma, R. K. Purohit, *Semiconductor Heterojunctions* (Oxford: Pergamon), 1974



## CHAPTER 3

### MATERIAL CHARACTERIZATION

As the n-type window layer for the ETA solar cell presented in this study, the spin coated nano-porous, sputtered thin film, hydrothermally grown nanowire and electrochemically anodized nanotube TiO<sub>2</sub> layers are used. The n-type wide band gap TiO<sub>2</sub> layer is covered by the sputtered or electrodeposited CdTe layer followed by the void-filling hole-conducting p-type sputtered ZnTe or ZnSnTe layers. In this structure, the visible light is absorbed by CdTe layer, for which the photons with energy  $h\nu \geq E_g$  excite the electrons to the CdTe conduction band. Later the excited electrons are conducted to the n-type electron conductor TiO<sub>2</sub> layer and holes to the electrode through CdTe and ZnSnTe for two-component and three component ETA solar cells respectively to contribute to the photo generated current.

In the following sections the results of the structural, morphological, optical and electrical characterization of the deposited thin film layers used for the ETA solar cell structure formation, will be presented and discussed. The complete device structure will be discussed in Chapter 4.

#### 3.1 Characterization of n-Type TiO<sub>2</sub> Layer

##### 3.1.1 Sputtered TiO<sub>2</sub> Thin Film

###### 3.1.1.1 Structural and Morphological Properties

Different deposition runs were performed to deposit the sputtered TiO<sub>2</sub> thin films to optimize the parameters of compact layer used as the nano-porous n-type material. The XRD measurements of TiO<sub>2</sub> films coated onto glass substrates with different RF Powers, which are illustrated in Figure 3.1, show amorphous behaviour [1,2] which can be attributed to the low thickness of the films.

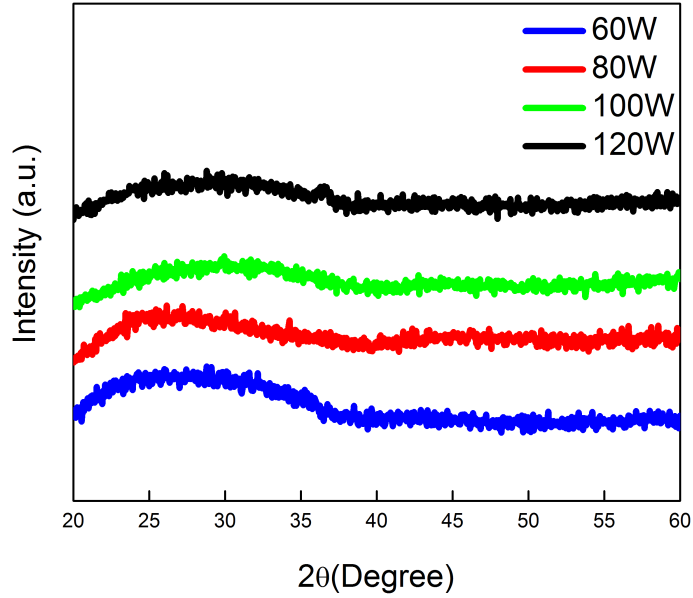


**Figure 3. 1** XRD patterns of the sputtered TiO<sub>2</sub> films with different RF Powers

High-resolution SEM images of sputtered thin film for one and two deposition run times are given in Figure 3.2 and 3.3, which shows that uniform and pin hole free layers are fabricated. Cross-sectional images reveal that the second run time does not have significant impact on the thickness of the produced film compared to one run time sputtered TiO<sub>2</sub> film for the same RF Power, it is worth to mention that increasing the RF power results the thicker sputtered TiO<sub>2</sub> films.

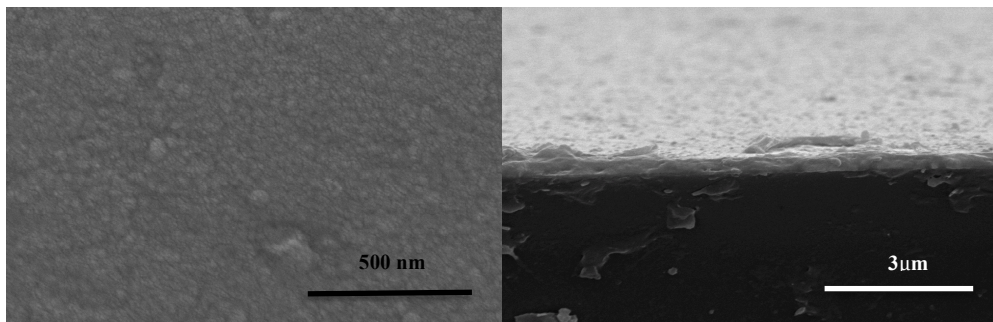


**Figure 3. 2** SEM micrographs of one deposition run time sputtered TiO<sub>2</sub> film (P=120W)

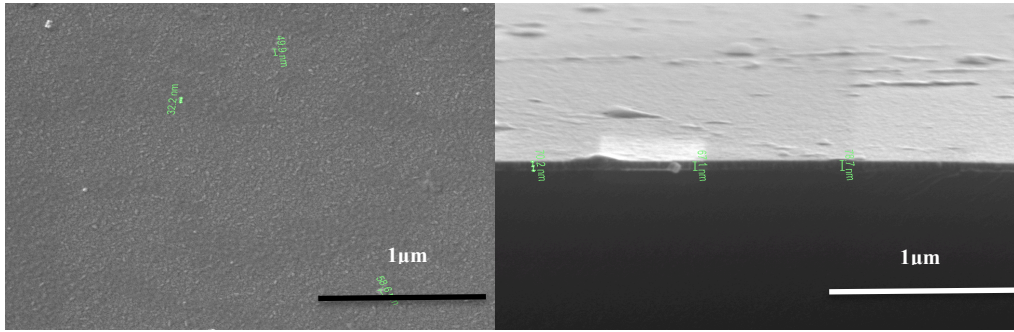


**Figure 3. 3** SEM micrographs of two deposition run time sputtered TiO<sub>2</sub> film (P=120W)

The AFM image of the sputtered film given in Figure 3.4 shows an average roughness of 22 nm for the sputtered TiO<sub>2</sub> film; this high value can be due to the non uniformity of the film in contrast with SEM images.

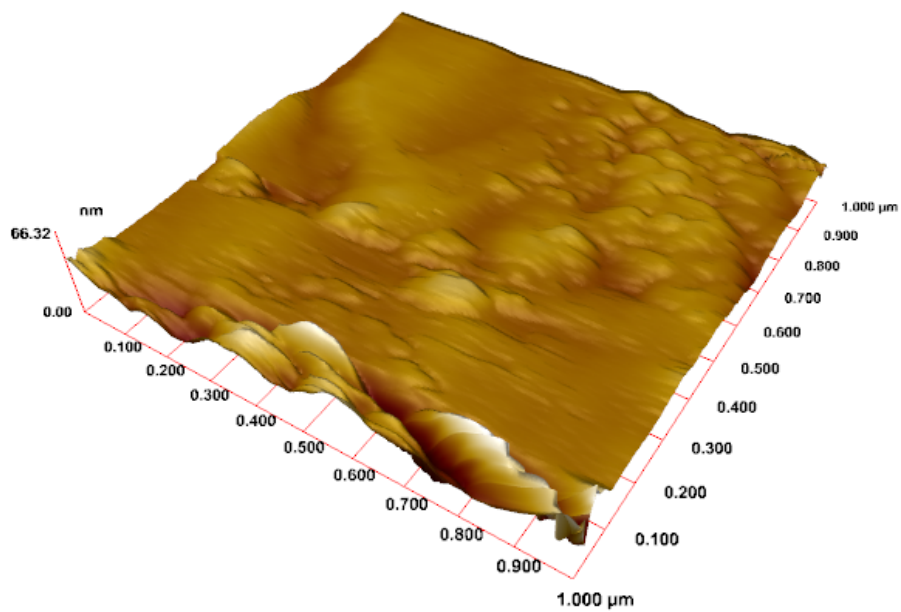
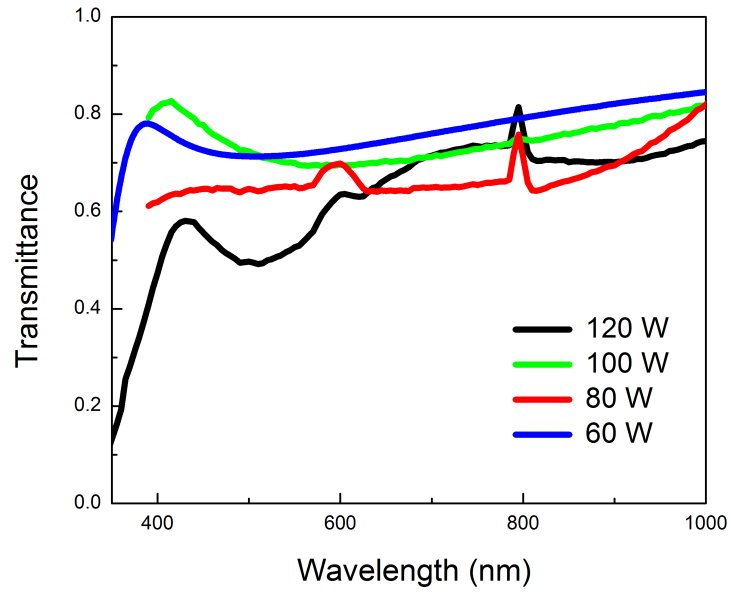


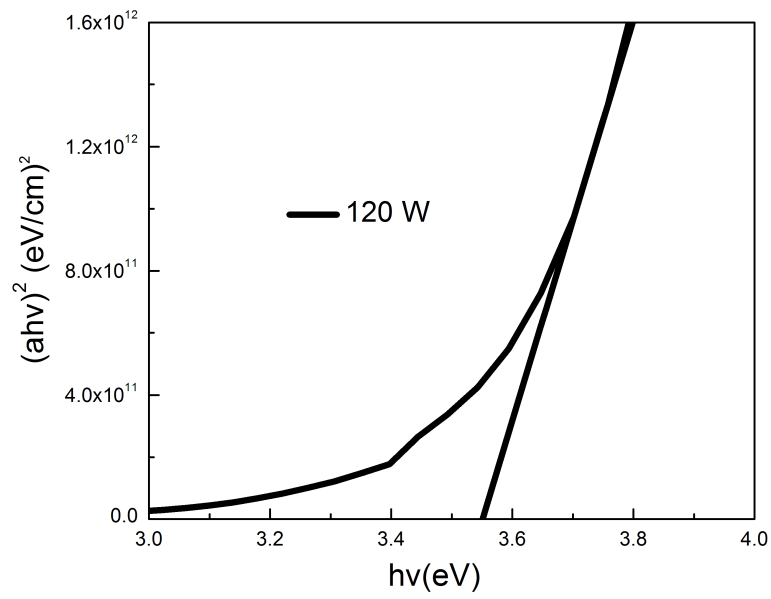
**Figure 3. 4** AFM image of one deposition run time sputtered TiO<sub>2</sub> film (P=120W)

### 3.1.1.2 Optical Properties

The transmittance spectra and Tauc plot for sputtered TiO<sub>2</sub> are given in Figure 3.5. It is observed that the films have maximum transmittance about 80% at the wavelength interval of around 375-600 nm for high energy levels [1]. The films have the band gap value  $E_g$  around 3.5 eV [2,3]. Both the transmittance and band gap values are suitable for the material properties to be used as the wide band gap n-type material for the ETA solar cells. In this study the deposition time for sputtered TiO<sub>2</sub> as the n-type window layer and compact layer used for nano-porous TiO<sub>2</sub> layer were determined as 120 min and 20 min respectively. The other deposition parameters of the sputtered TiO<sub>2</sub> were found as the substrate temperature of 200 °C and RF power of 120 W for both TiO<sub>2</sub> layers.



(a)



(b)

**Figure 3. 5** (a) Transmittance spectra (b) Tauc plot of sputtered TiO<sub>2</sub> film

### 3.1.2 Spin Coated TiO<sub>2</sub> Films

#### 3.1.2.1 Structural and Morphological Properties

XRD measurements were performed to determine the diffraction patterns, phases and orientations of the spin coated TiO<sub>2</sub> films on glass substrates. The XRD analysis of the powder is given in Figure 3.6. The comparative XRD study of the TiO<sub>2</sub> films coated with single and two successive different spin rates on glass substrates is illustrated in Figure 3.7. Also the effect of different annealing environments on the spin coated TiO<sub>2</sub> films on glass substrates is given in Figure 3.8.

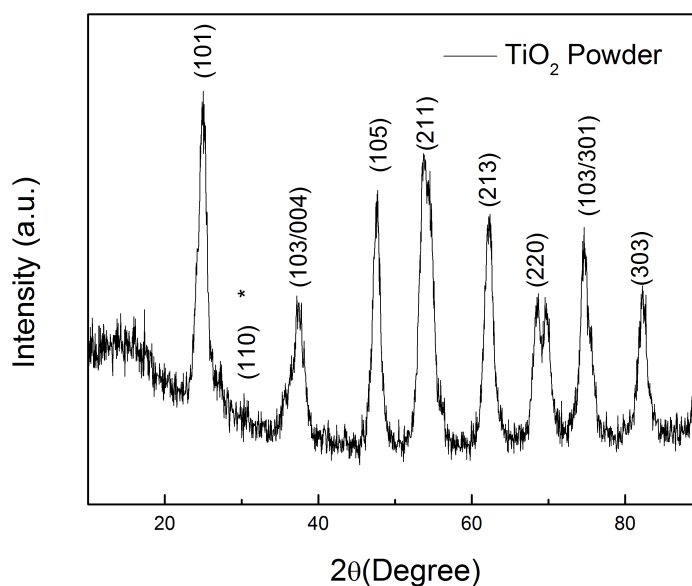


**Figure 3. 6** XRD patterns of the TiO<sub>2</sub> powder, peak indicated by \* is due to rutile phase

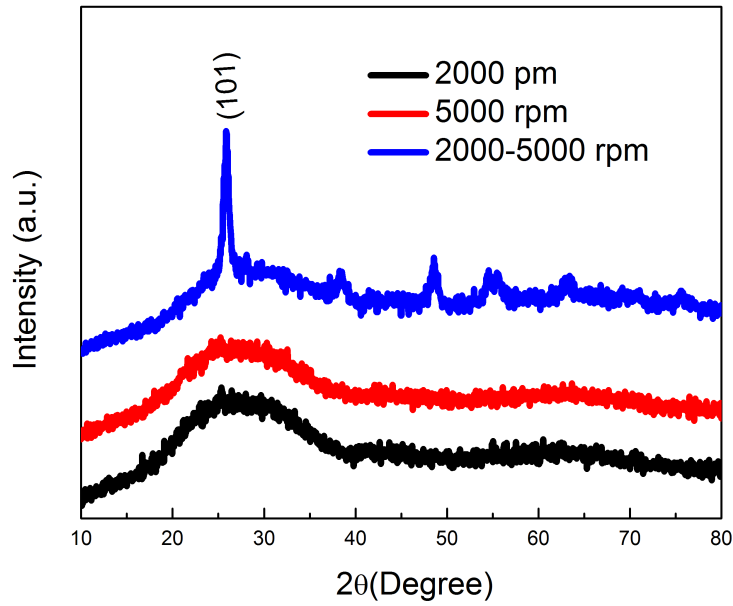


**Figure 3. 7** XRD patterns of spin coated TiO<sub>2</sub> films deposited with the spin coating speeds of 2000, 5000 and (2000-5000) rpm

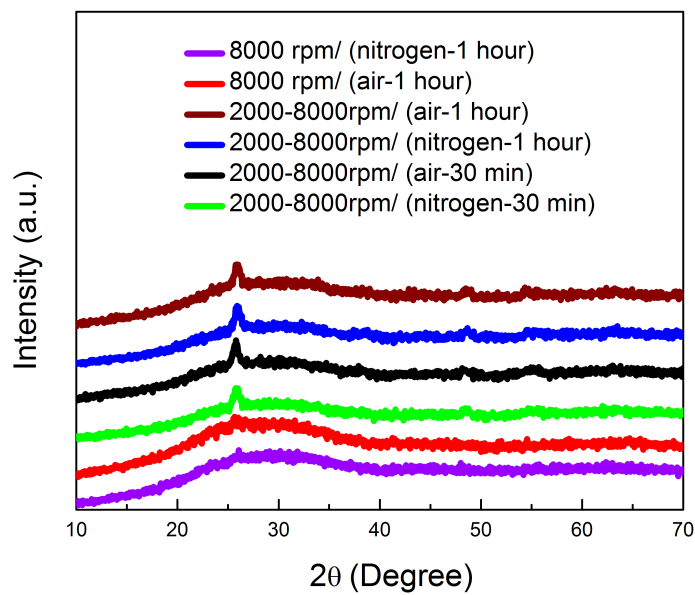


**Figure 3. 8** XRD patterns of the one and two run deposition time spin coated TiO<sub>2</sub> films for different annealing environments and annealing temperatures

According to Figure 3.6, the powder had nano-particle structure and showed crystalline anatase phase (JCPDS 21-1272 Anatase) with preferred orientation along (101) plane with diffraction angle  $2\theta$  of about  $25^\circ$  [4]. Although the anatase is the desirable form of  $\text{TiO}_2$  for solar cell applications, a weak peak for the rutile phase is also detected (JCPDS 73-1765 Rutile) in the structure, which is negligible. XRD patterns of one run time  $\text{TiO}_2$  films coated on glass substrates by spin coating deposition technique show that the deposited films are amorphous in nature. For the  $\text{TiO}_2$  films with two successive different spin rates, the films showed crystalline phases with preferred orientation along (101) plane and diffraction angle  $2\theta \sim 25^\circ$  [5]. In fact the thickness of spin coated  $\text{TiO}_2$  films affected the formation of the crystalline or amorphous structure of the films. The effect of different annealing times and environments were investigated, which showed that there was not any obvious change in the structure and the only important factor is the thickness value of the spin coated films.

The average microcrystalline grain size  $d$  of powders calculated from the XRD pattern using Equation 2.15 is about 24 nm. Specific surface area of the powders used in this work is  $108 \text{ m}^2/\text{g}$  calculated from the BET gas adsorption measurements with an average pore size of 17 nm. This degree of specific surface area is suitable for nano-crystalline and solar cell applications. Assuming spherical particles, the average particle size [6] was calculated from the expression;

$$D = \frac{6000}{S_{sp} \cdot \rho_a} \quad (3.1)$$

In Equation 3.1,  $D$  is the particle size in nm,  $S_{sp}$  is the specific surface area of the powders in  $\text{m}^2/\text{g}$  and  $\rho_a$  is the density of  $\text{TiO}_2$  ( $4.23 \text{ g}/\text{cm}^3$ ). The calculated value of about 48 nm of BET measurement is twice the crystalline size obtained from XRD measurements; this difference is attributed to the slightly agglomerated nature of the powder in BET measurement.

High-resolution SEM images of spin coated films are given in Figure 3.9. Films are in the form of a network of high porosity inter-connected nano particles, which approximately have a pore size ranging between 50 and 100 nm, and the particle size of around 20 nm. These results confirm that the films have high porosity and high surface area, which are critical factors for most nano-crystalline solar cell structures demanding binding sites for absorber layers and open pores providing enough space for the penetration of the absorber layer.



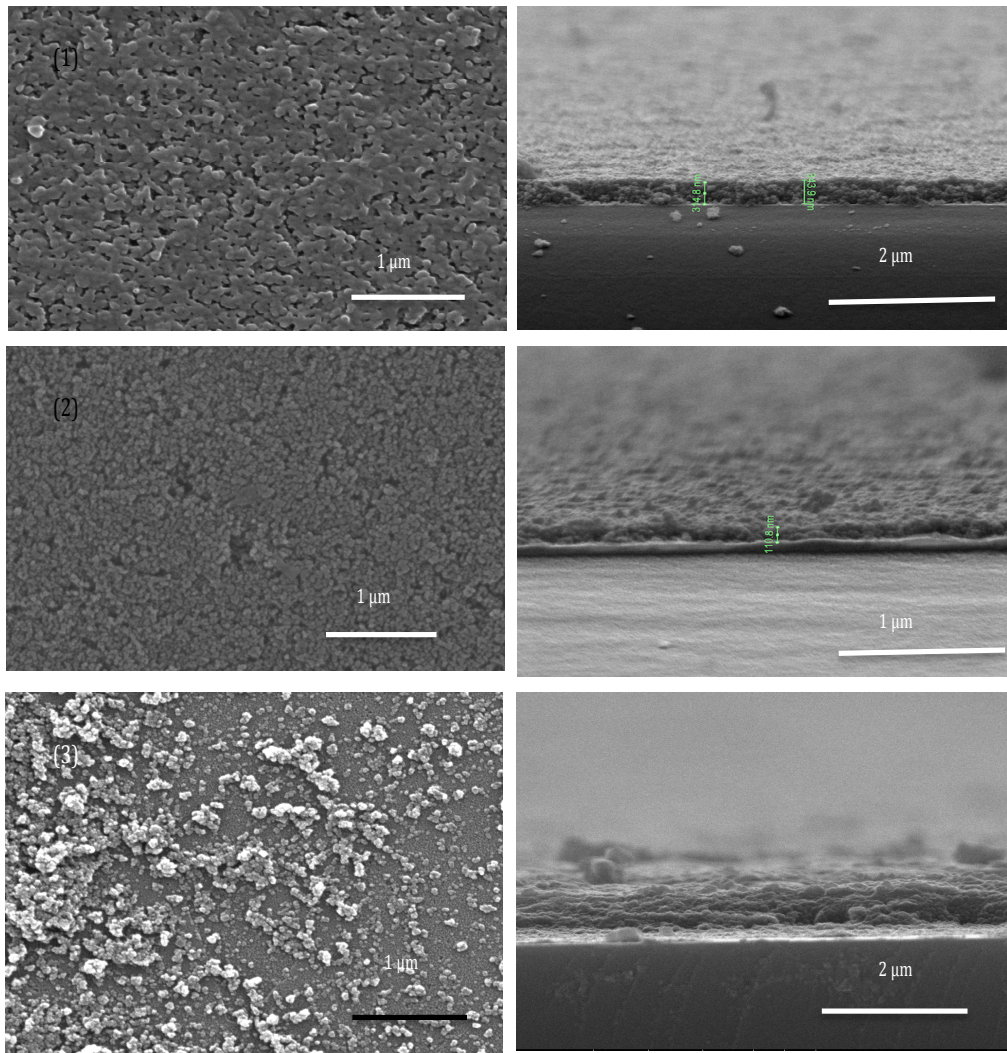


**Figure 3. 9** SEM micrographs of spin coated TiO<sub>2</sub> films deposited with the spin coating speeds of (1) 2000, (2) 5000 and (3) (2000-5000) rpm

Cross-sectional images reveal that by changing the spin rate, simply it is possible to obtain thin films with different thicknesses down to 80 nm and up to micrometer value. Films were homogeneous and crack free on the entire surface. Also there were no visible agglomerates on the surface, which shows a proper homogenization of the paste used in this study. For the films obtained with one run time the existence of some pores were observed, which resulted in the shorting between the absorber layer and anode. Although no significant difference was noticed regarding the morphology of the films on glass substrates at different spinning rates;

it is observed that a better crystallinity and increase in the grain size was observed using XRD and SEM results for the thicker two run time TiO<sub>2</sub> films. For example the films deposited with 2000-5000 rpm successive spinning rate had better crystalline structure compared to the films spin coated with single run at 2000 and 5000 rpm spin rates [5].

The results of the AFM measurements are shown in the Figure 3.10 and Table 3.1 summarizes the roughness values of the films. A high-resolution AFM images revealed the results which are consistent with the SEM results, films are porous and have a nano-particulate structure. Particle sizes for the films deposited with single run time were around 25-30 nm and pore sizes are around 50-100 nm. There are no large voids or deviations in the homogeneity of the films as indicated by the roughness values, which were around 18 nm for all samples. The AFM images show that there is no obvious dependence of roughness value on the spinning rates and reproducible results can be obtained for different thickness values. The obtained roughness value both for one and two successive different spin rates are around 18 nm, which means a high surface area between TiO<sub>2</sub> and CdTe absorber layer.

**Table 3. 1** The roughness values of the coated films and glass substrate

Sample	Glass substrate	TiO <sub>2</sub> (2000) rpm	TiO <sub>2</sub> (5000) rpm	TiO <sub>2</sub> 8000) rpm	TiO <sub>2</sub> (2000-5000) rpm
Roughness value	1.61 nm	18.9 nm	17.1 nm	18 nm	18.7 nm

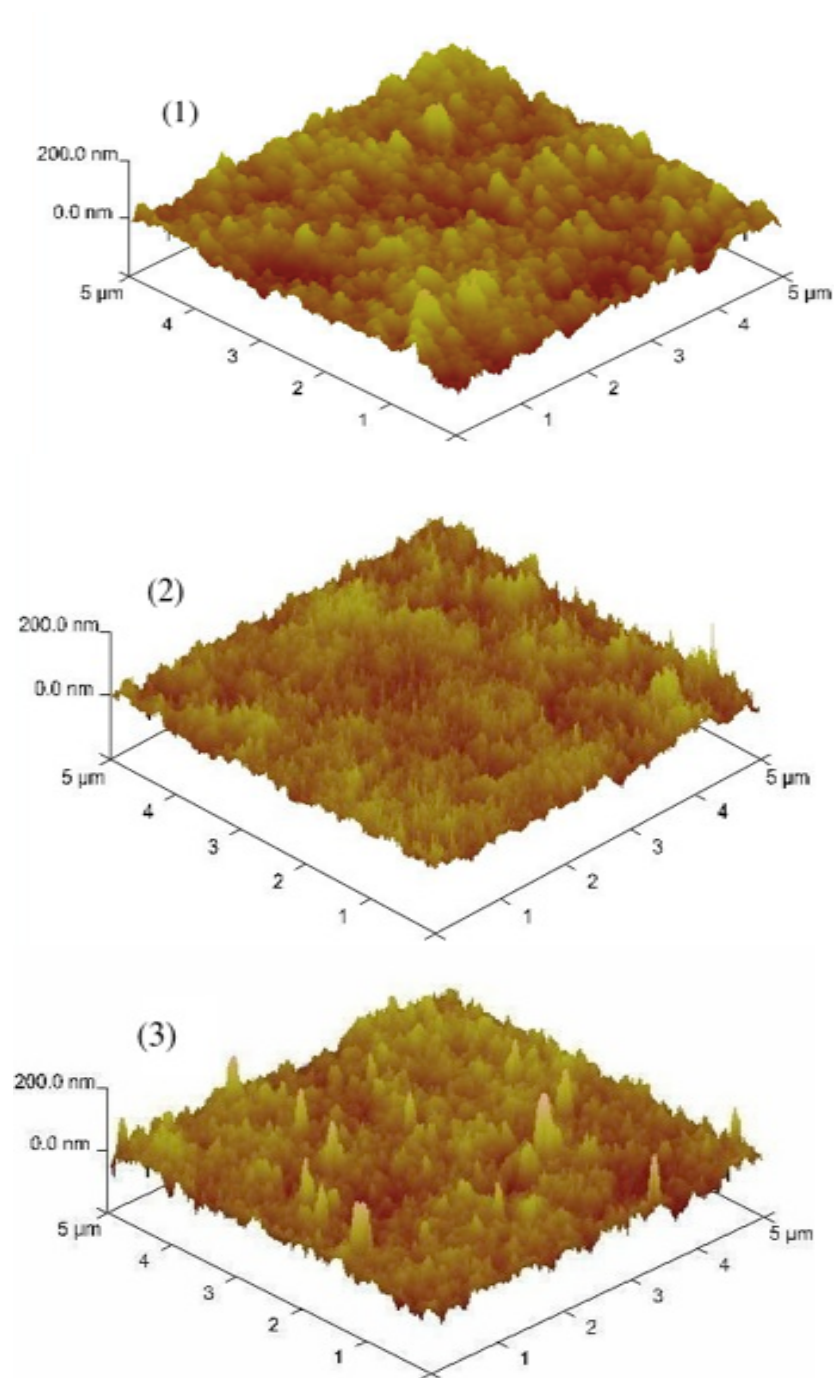
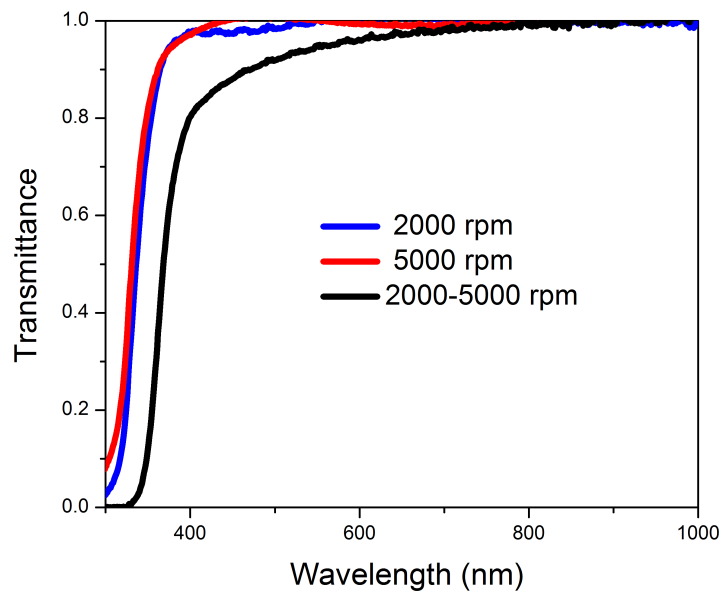


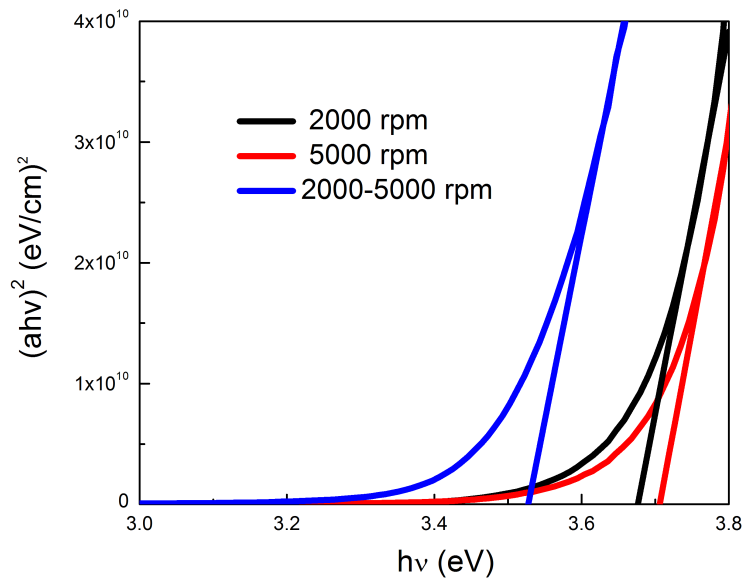
**Figure 3. 10** AFM images of spin coated TiO<sub>2</sub> films deposited with the spin coating speeds of (1) 2000, (2) 5000 and (3) (2000-5000) rpm

### 3.1.2.2 Optical Properties

The room temperature transmittance measurements were performed for the optical characterization of the films deposited on glass substrates at different spin rates. The comparative transmittance spectra and Tauc plots for the one and two successive different spin rates are shown in Figure 3.11. Transmittance versus  $\lambda$  (wavelength) variations show that the films transmits the light more than 90% at the wavelength interval of around 375-600 nm, which indicates a good transmittance of visible light to be chosen as window layer. All the films deposited on glass substrates exhibited direct band gap energy values of around  $E_g=3.5$ - $3.6$  eV, which are in consistent with those reported values [7,8].



(a)



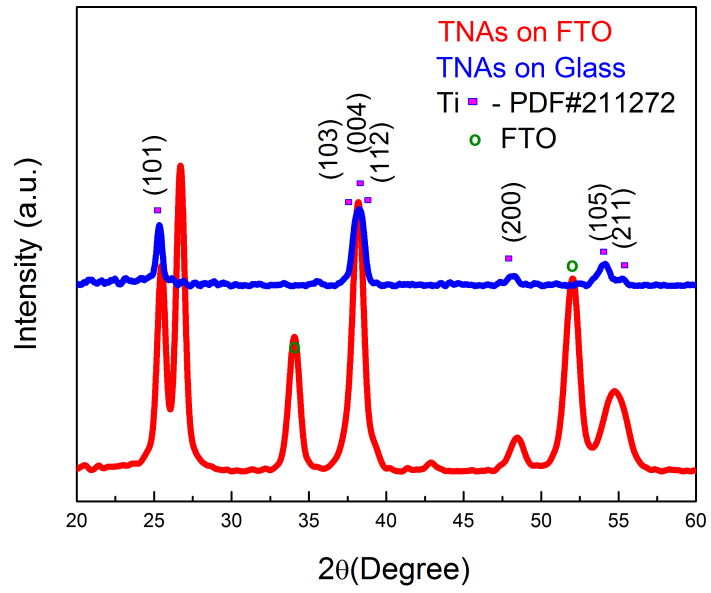
(b)

**Figure 3. 11** (a) Comparative transmittance spectra and (b) Tauc plot of spin coated  $\text{TiO}_2$  films with one and two successive different spin rates

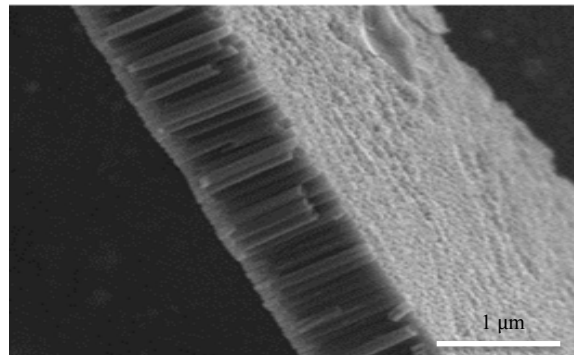
### **3.1.3 Electrochemically Anodized TiO<sub>2</sub> Nanotube Arrays (NTAs)**

#### **3.1.3.1 Structural and Morphological Properties**

XRD measurements were used to determine the diffraction patterns and the present phases of the deposited NTAs on glass and FTO coated glass substrates. The XRD analysis given in Figure 3.12 (a) show that the fabricated anatase phase nanotubes have polycrystalline nature. The as-grown nanotubes were amorphous and changed to be crystallized by annealing (heat-treatment) process. The cross-sectional SEM image of NTAs in Figure 3.12 (b) show the highly ordered and closely packed generated TiO<sub>2</sub> nanotubes [9].



(a)



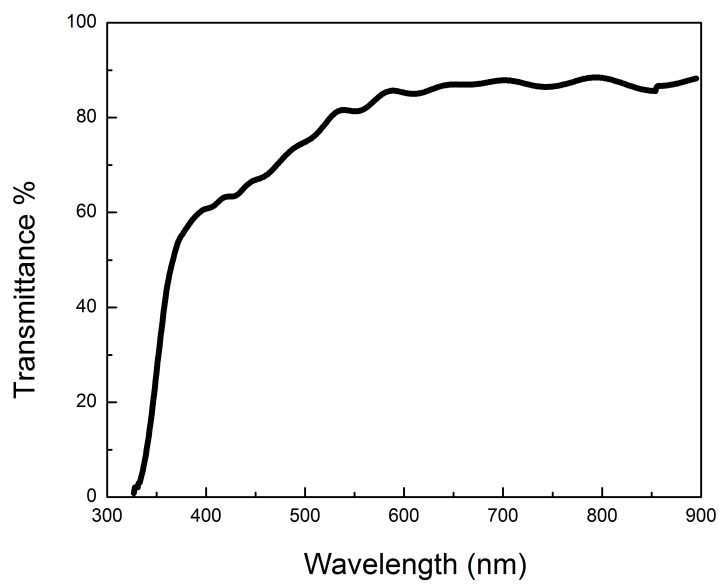
(b)

**Figure 3. 12** (a) XRD pattern (b) SEM image of the TiO<sub>2</sub> NTAs

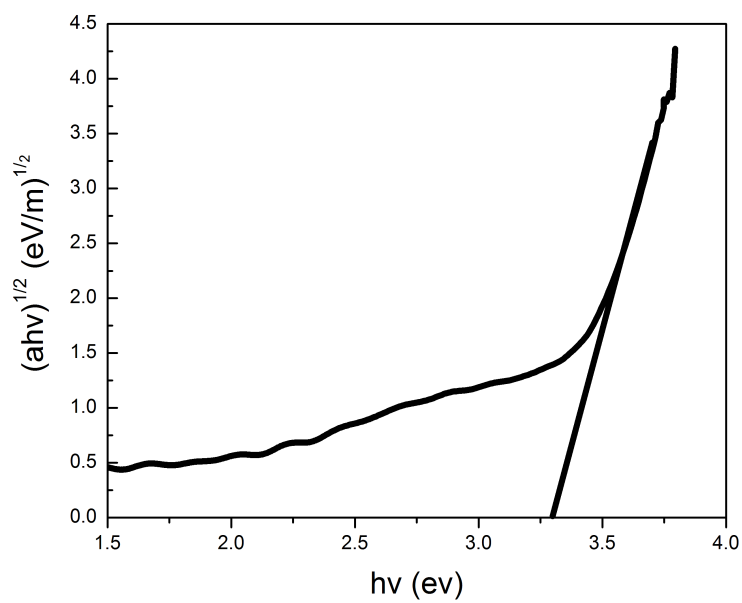
### 3.1.3.2 Optical Properties

Figure 3.13 (a) and (b) show the Transmittance% versus  $\lambda$  (wavelength) variation and Tauc plot for TiO<sub>2</sub> nanotubes respectively. The measurements show that the TiO<sub>2</sub> nanotube films have transmittance of about 60-90% at the wavelength interval of around 400-700 nm. These n-type transparent films have band gap energy of around  $E_g=3.25$  eV. Both the transmittance and band gap values are suitable parameters for the n-type wide band gap window semiconductor.





(a)



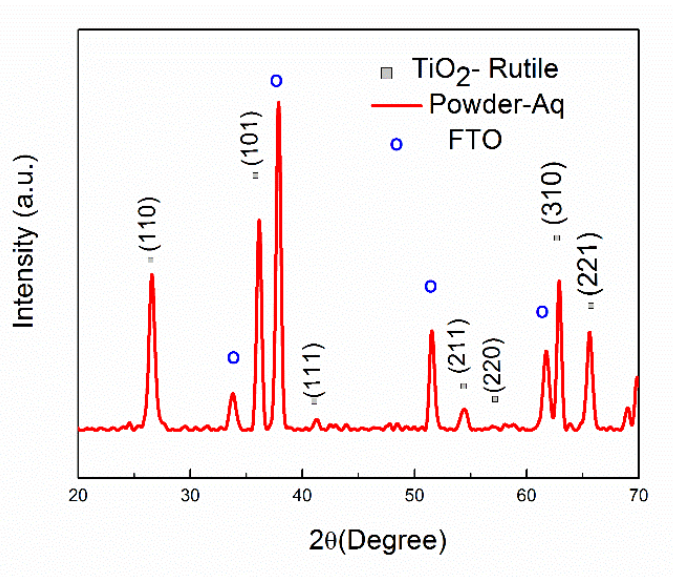
(b)

**Figure 3. 13** (a) Transmittance spectrum and (b) Tauc plot of the TiO<sub>2</sub> NTAs

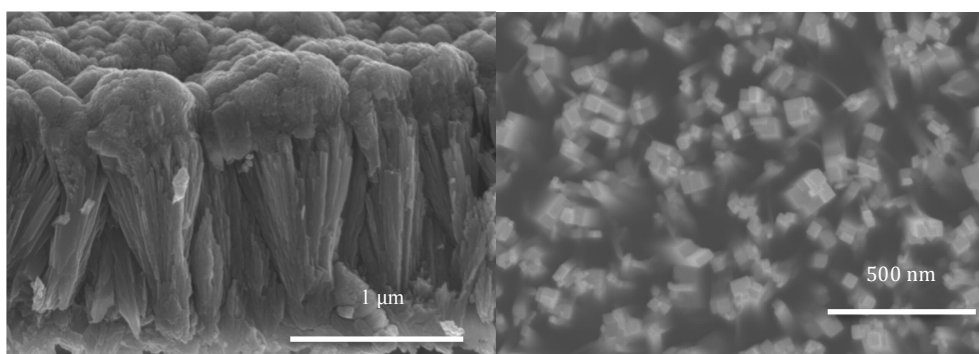
### **3.1.4 Hydrothermally Grown TiO<sub>2</sub> Nanowires**

#### **3.1.4.1 Structural, Morphological and Optical Properties**

XRD measurements of the deposited nanowires on FTO coated glass substrates with aqueous recipes explained in Section 2.3.2.4 illustrated in Figure 3.14 (a) show the formation of rutile phase nanowires with polycrystalline nature. The cross-sectional SEM images of NTAs given in Figure 3.14 (b) and (c) show the highly compact, vertically oriented TiO<sub>2</sub> nanowires with rectangular cross-section with the width around 20 nm, where the distance between the NWAs vary between 50-200 nm. The films have the band gap energy of around 2.6 eV as shown in Figure 3.14 (d) [9].

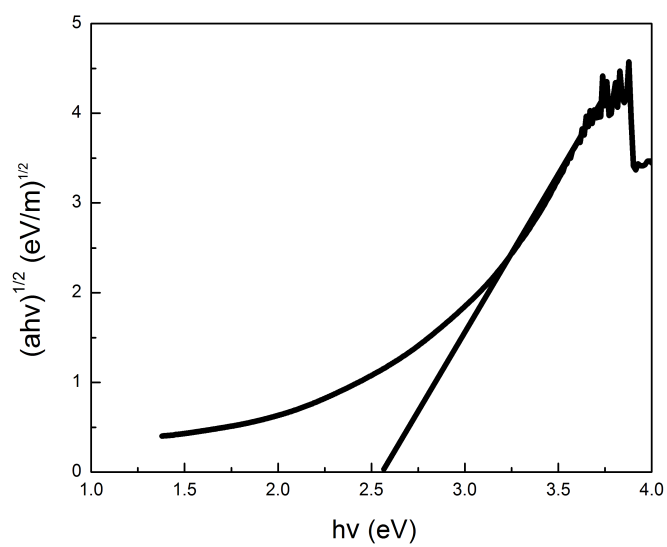


(a)



(b)

(c)



(d)

**Figure 3. 14** (a) XRD pattern (b) and (c) SEM images (d) Tauc plot of NWAs of TiO<sub>2</sub>

## **3.2 Characterization of CdTe Thin Film Absorber Layer**

### **3.2.1 Sputtered CdTe Thin Film**

#### **3.2.1.1 Structural and Morphological Properties**

CdTe thin films were sputtered onto glass substrates by varying the deposition parameters such as substrate temperature and deposition time to optimize the deposition parameters, which lead the realization of the suitable material properties of CdTe absorber material for ETA solar cell applications. The results of the XRD measurements for the CdTe thin films with different thickness values is given in Figure 3.15. Using Scherrer's formula, the average crystallite size calculated from the XRD patterns of sputtered CdTe is about 40 nm. The XRD result implies that the increase in the thickness of the film and also annealing temperature, improve the crystallinity. Upon searching in database cards, as illustrated in Figure 3.15, the (111) main peak of sputtered CdTe were detected at  $2\theta$  around 24 degree with JCPDS card no 15-0770 [10].

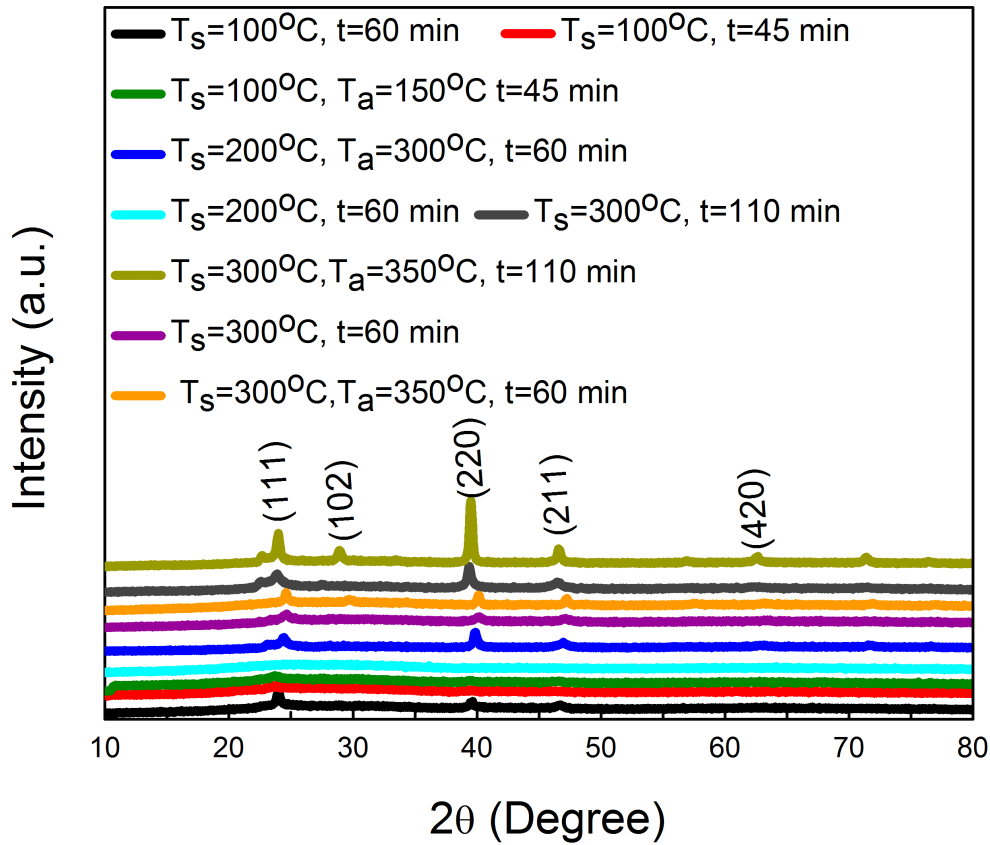


**Figure 3. 15** XRD patterns of the sputtered CdTe films deposited with different substrate/annealing temperatures and deposition time (RF=70 W)

High-resolution SEM images of sputtered CdTe films deposited on glass substrates with deposition parameters of RF=70 W,  $t=60$  min,  $T_s=300^\circ\text{C}$ ,  $T_a=350^\circ\text{C}$  are given in Figure 3.16. The images show the presence of crack and pore free films with thickness value around 250 nm.

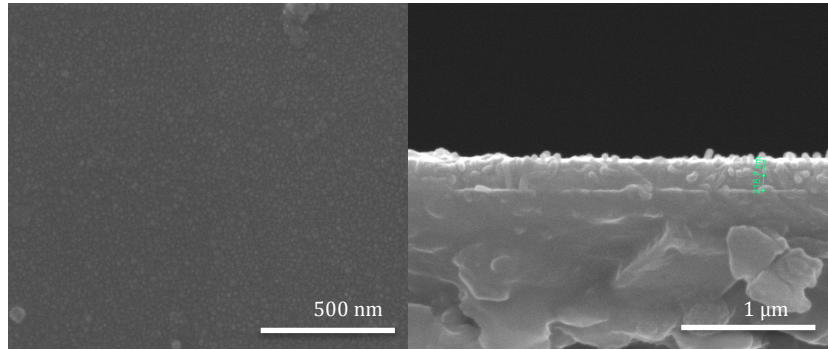


**Figure 3. 16** SEM images of the sputtered CdTe film (RF=70 W, t=60 min,  $T_s=300\text{ }^{\circ}\text{C}$ ,  $T_a=350\text{ }^{\circ}\text{C}$ )

The AFM image of CdTe film presented in Figure 3.17 reveals that the film has uniform morphology and structure with an average roughness of 3.7 nm, which implies the good uniformity of the CdTe absorber layer [10]. This low value of roughness shows that the CdTe films fills the pores, wires and tubes of nano structured  $\text{TiO}_2$  films, which predicates the good adhesion between n-type  $\text{TiO}_2$  window layer and extremely thin absorber CdTe layer. In this study the sputtered CdTe layer with t=10 min and t=60 min deposition time with RF=70 W and  $T=300\text{ }^{\circ}\text{C}$  were used as ETA layer for two- and three-component cells respectively.

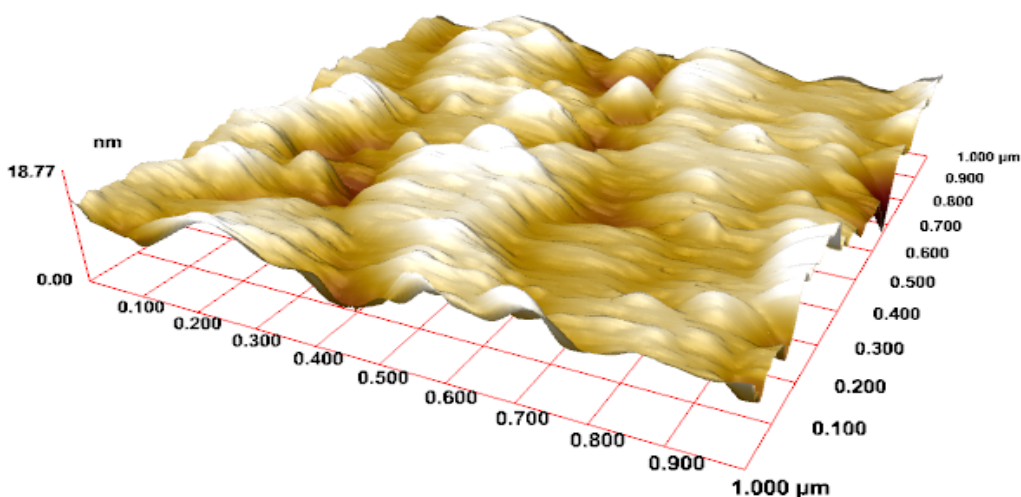
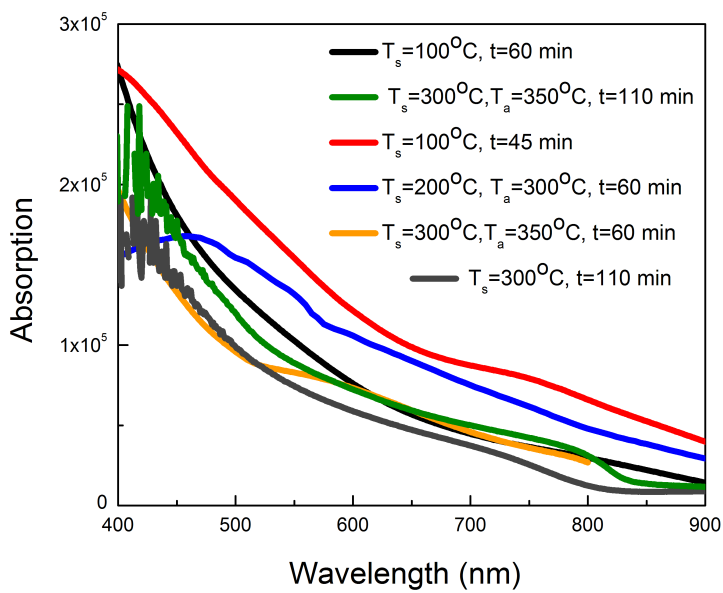


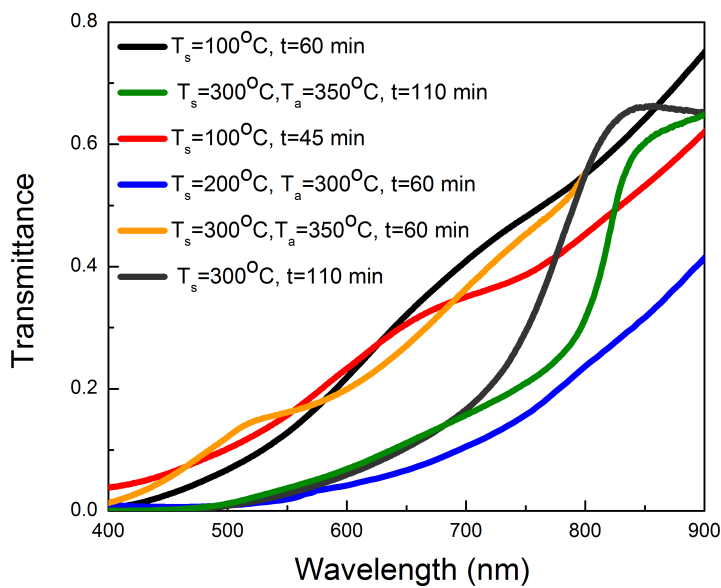
**Figure 3. 17** AFM image of the sputtered CdTe film (RF=70 W, t=60 min,  $T_s=300\text{ }^{\circ}\text{C}$ ,  $T_a=350\text{ }^{\circ}\text{C}$ )

### 3.2.1.2 Optical Properties

The absorption and transmittance spectra of the sputtered CdTe films on glass substrates are given in Figure 3.18. According to figure, the films have maximum transmittance of about 30% and the films show a high absorption values at the wavelength interval of around 375-700 nm. The Tauc plot of the CdTe film deposited on glass substrate (RF=70 W, t=60 min,  $T_s=300\text{ }^{\circ}\text{C}$ ,  $T_a=350\text{ }^{\circ}\text{C}$ ) is presented in Figure 3.19. The films show  $E_g$  around 1.6 eV [10], which annealing the substrates causes a small increase in  $E_g$  values of the films compared to as-grown.



(a)



(b)

**Figure 3. 18** (a) Absorption and (b) Transmittance spectra of the sputtered CdTe thin films



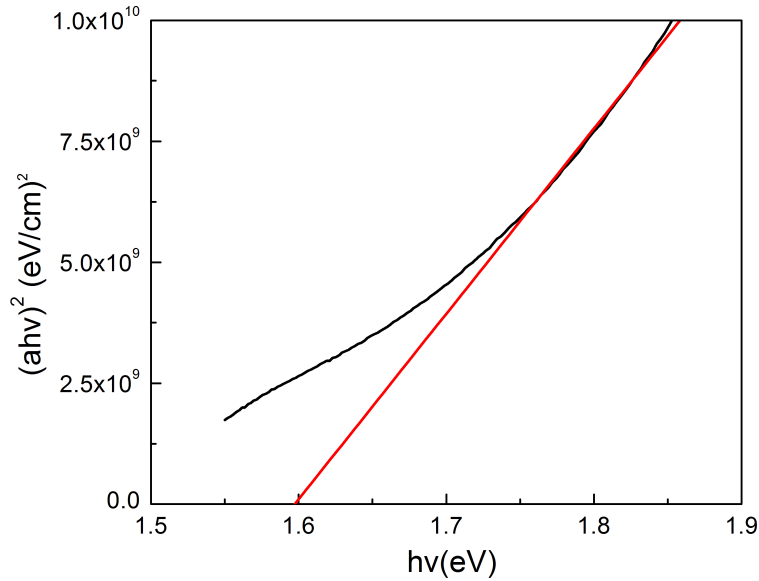


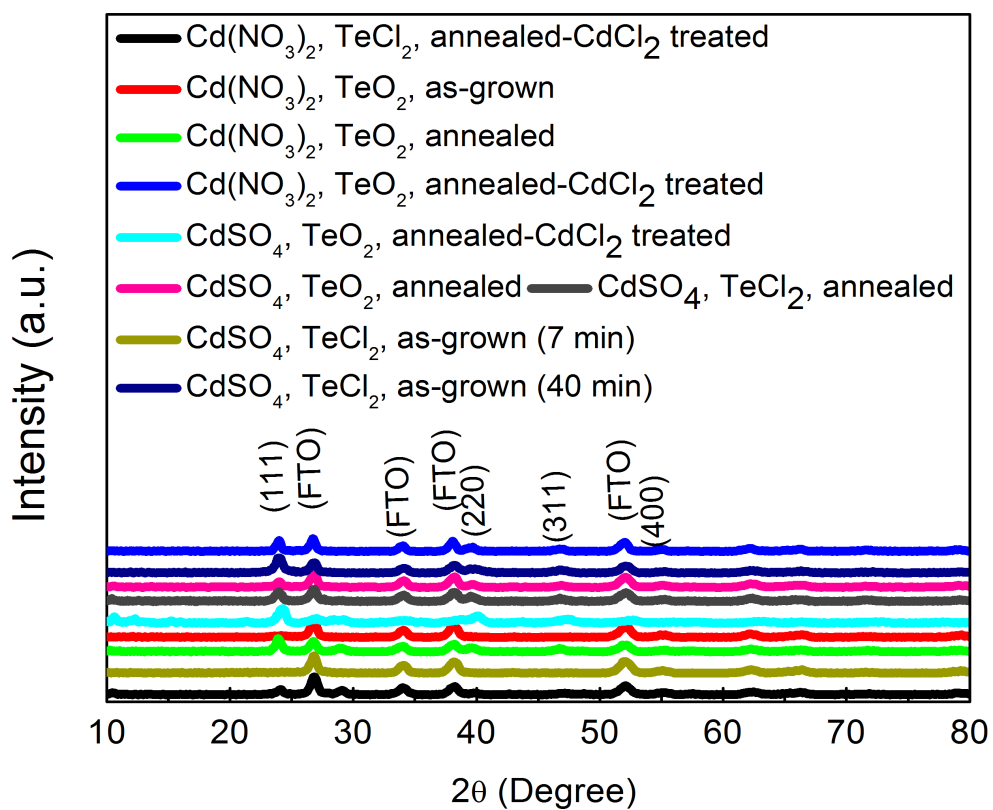
**Figure 3. 19** Tauc plot of the sputtered CdTe film (RF=70 W, t=60 min,  $T_s=300\text{ }^{\circ}\text{C}$ ,  $T_a=350\text{ }^{\circ}\text{C}$ )

### 3.2.2 Structural, Morphological and Optical Properties of Electrodeposited CdTe Layer

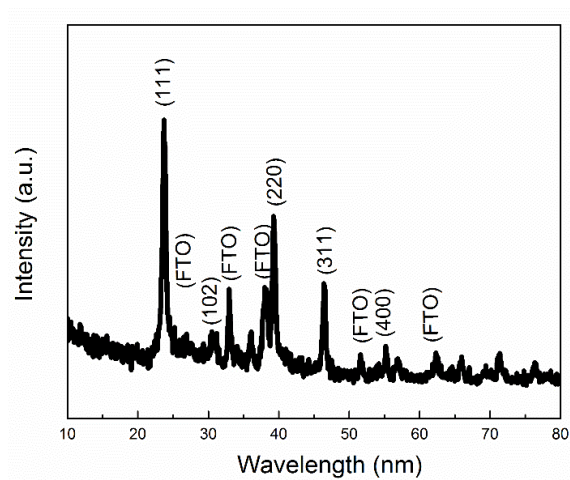
The XRD analysis of different CdTe films coated with different recipes by two- and three-electrode deposition methods are given in Figure 3.20. These analysis show the successful growth of CdTe layer on FTO substrates with the (111) main peak detected at  $2\Theta$  around  $24^{\circ}$  [11,12]. As it is observed from Figure 3.20 (a), the CdTe layer prepared with recipe 2 by three-electrode method show the best obtained crystallinity. Due to the mentioned reasons in part 2.3.3.2 the CdTe prepared by two-electrode electrodeposition method was characterized and used for device fabrication. In fact the non-aqueous solution was prepared by solving Cadmium Sulphate (0.5 M) and  $\text{TeO}_2$  (0.02 M) in ethylene glycol using magnetic stirrer in two-electrode ED method, where FTO/ $\text{TiO}_2$  and platinum are respectively working and counter electrodes. Figure 3.20 (b) shows the XRD patterns of the CdTe film deposited on FTO coated glass substrate prepared with two-electrode ED method, which shows a good crystalline behaviour.

High-resolution SEM image of two-electrode electrodeposited CdTe film is given in Figure 3.21 (a). The CdTe coating was homogeneously distributed on FTO substrate in the form of a

dens packing network of inter-connected non uniformity. The transmittance% and photoluminescence (PL) measurements are given in Figure 3.21 (b) and (c). The transmittance% spectrum shows that the film transmits less than 30% of light at the wavelength interval of around 375-800 nm, which is a good parameter for absorber p-type layer. From the PL measurements it was observed that the band edge for electrodeposited CdTe layer was around 1.45 eV, which is comparable with the reported study [11].

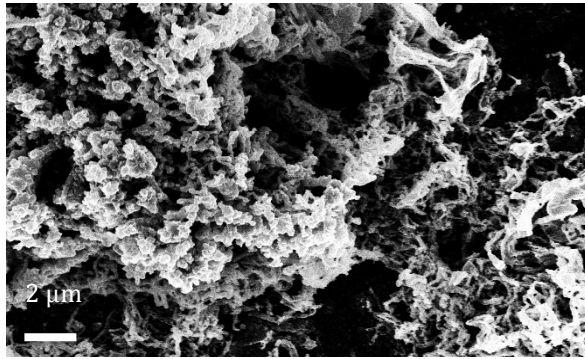


(a)

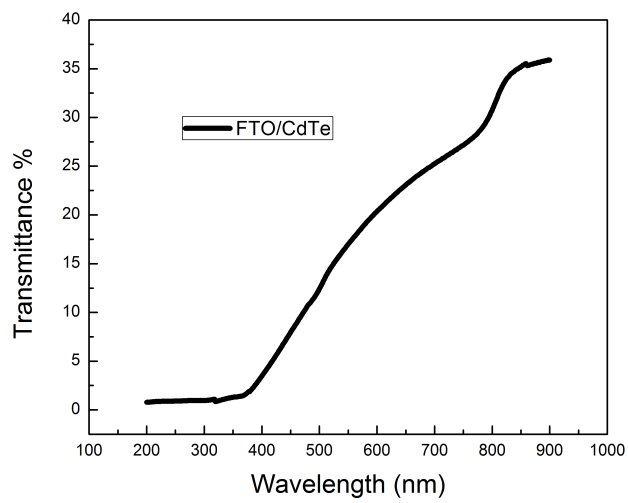


(b)

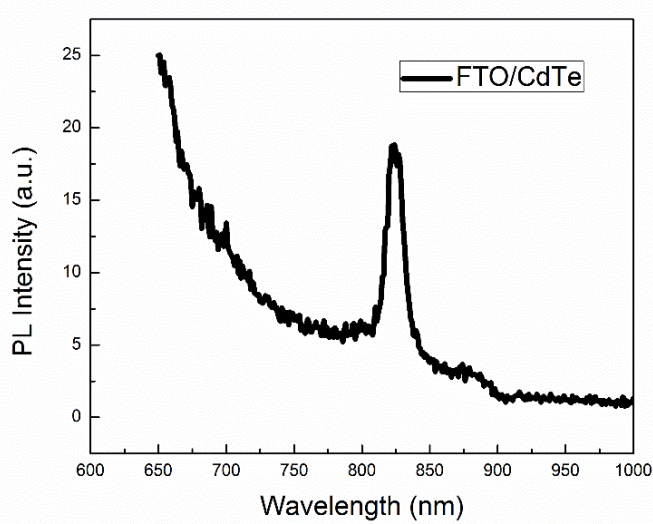
**Figure 3. 20** XRD patterns of the CdTe films deposited on FTO coated glass substrates prepared with (a) Three-electrode (b) Two-electrode method



(a)



(b)



(c)

**Figure 3. 21** (a) SEM image (b) Transmittance (c) Photoluminescence of CdTe film deposited on FTO coated glass substrates prepared with two-electrode method

### 3.3 Characterization of p-Type ZnTe and ZnSnTe Layers

#### 3.3.1 Structural and Morphological Properties

In this section ZnTe and ZnSnTe semiconductors were characterized. As it was mentioned in Sections 1.4.3 and 2.3.4 in order to enhance the conductivity of ZnTe, it was doped with SnTe and consequently low resistance ZnSnTe material was fabricated as the suitable p-type material for ETA solar cell applications.

The XRD measurement results of the as-grown and annealed ZnTe thin films are given in Figure 3.22. These XRD patterns showed that ZnTe films have polycrystalline nature with high intensity reflection peak along (111) plane with diffraction angle  $2\theta$  about  $25.25^\circ$  [13]. The crystalline size of ZnTe films were calculated from the XRD pattern using the Scherrer's formula for annealed and as-grown films having almost the same value of 5 nm.

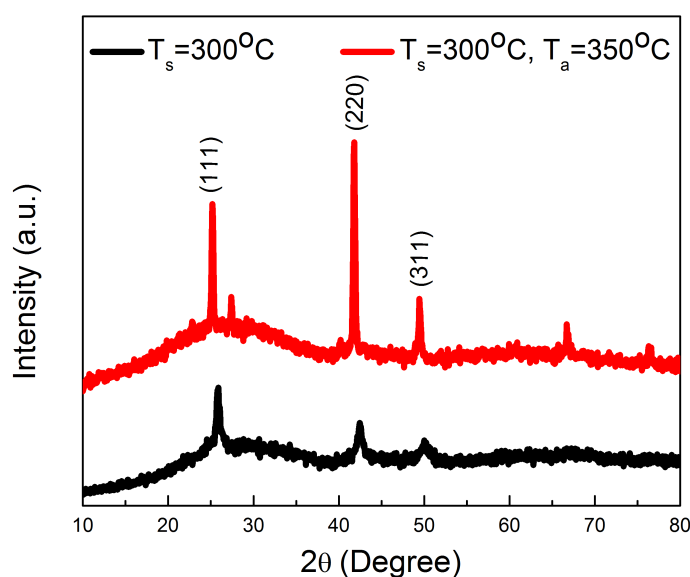


**Figure 3. 22** XRD patterns of the ZnTe films

In order to determine the diffraction patterns also the phases and orientations of different sets of ZnSnTe thin films, XRD measurements were performed and the results are given in Figure 3.23. The XRD patterns showed that the films have polycrystalline nature. The high intensity

reflection was obtained with preferred orientation along (111) plane with diffraction angle  $2\theta$  about  $25.25^\circ$  with ZnTe phase [13], where different peaks associated with SnTe and Te were also observed. The crystallinity is improved by heat-treating the films for 5 minutes, where annealing for 30 minutes cause the films crystallinity to decrease. This may be attributed to the degradation of the films.

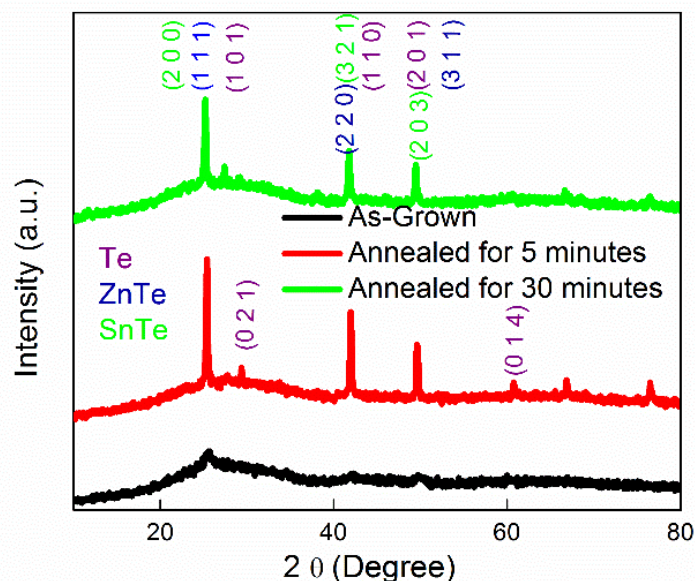


**Figure 3. 23** XRD patterns of the ZnSnTe films

To determine the composition of films energy dispersive X-ray analysis (EDXA) was used, which the percentage of atomic ratios were found as about Zn:Sn:Te = 41: 3.98 :54.83 % , Zn:Sn:Te = 43.38 : 4.10 : 52.5 % , Zn:Sn:Te = 29.56: 4.26 :25.13 % for the as-grown, annealed for 5 and 30 minutes respectively. As it is given in Table 3.2, the resistance values of the films were  $16 \times 10^6$  ( $\Omega$ ),  $4.2 \times 10^6$  ( $\Omega$ ) and  $3 \times 10^{10}$  ( $\Omega$ ) for the as-grown and annealed films for five and 30 minutes respectively. Due to the presented resistivity values, the samples annealed for five minutes at  $350^\circ\text{C}$  were used in the device fabrication.

**Table 3. 2** Zn:Sn:Te ratios and resistance values of different ZnSnTe samples

	Zn%	Sn%	Te%	R ( $\Omega$ )
(As-grown)	41	3.98	54.83	$16 \times 10^6$
(Annealed for 5 min)	43.38	4.10	52.5	$4.2 \times 10^6$
(Annealed for 30 min)	29.56	4.26	25.13	$3 \times 10^{10}$

The SEM images of both as-grown and annealed ZnTe films are presented in Figure 3.24. The homogeneous and uniform ZnTe layer thickness is measured as about 340 nm for the as-grown film. The SEM images of different ZnSnTe films as an alternative low resistance p-type material are given in Figure 3.25. The images show that the films annealed for 30 minute have some voids, which may cause shunt in the structure, also no agglomeration was observed on the surface dedicated the presence of homogeneous films. These SEM images of ZnSnTe films are in consistent with XRD results.

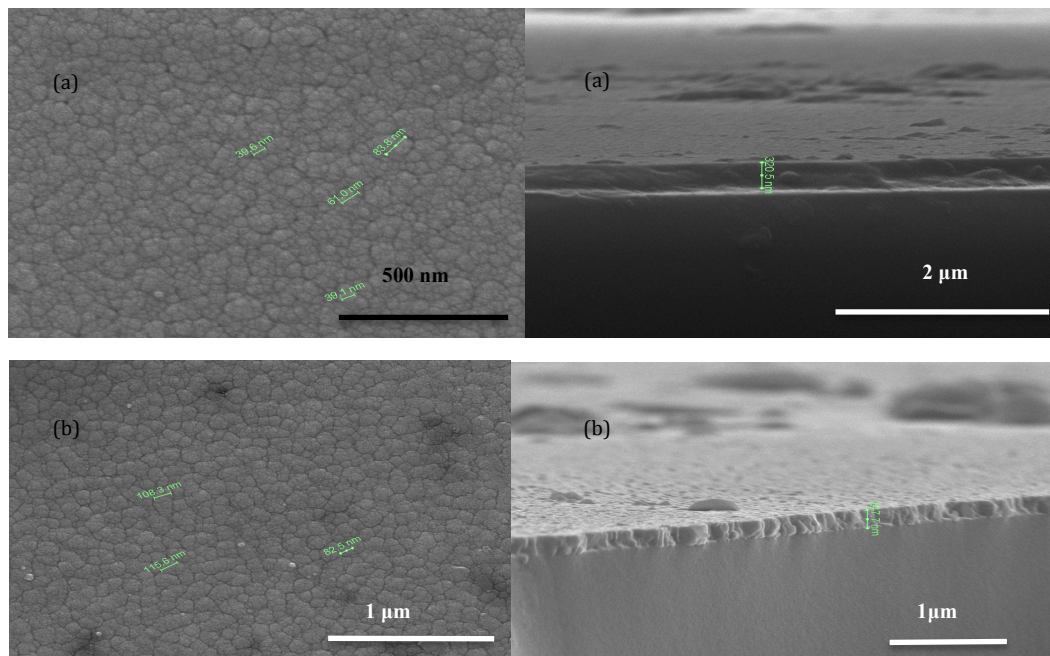


**Figure 3. 24** SEM images of sputtered ZnTe films (a) As-grown ( $T_S=300$  °C) (b) Annealed ( $T_S=300$  °C annealed at  $T_a=350$  °C)



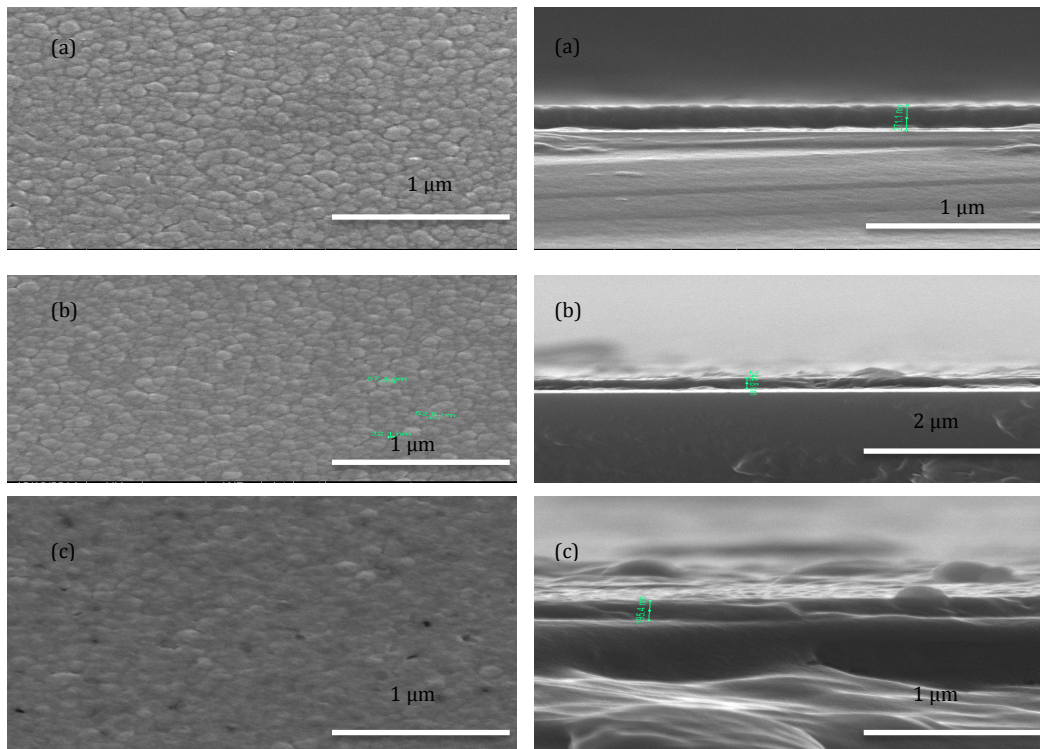


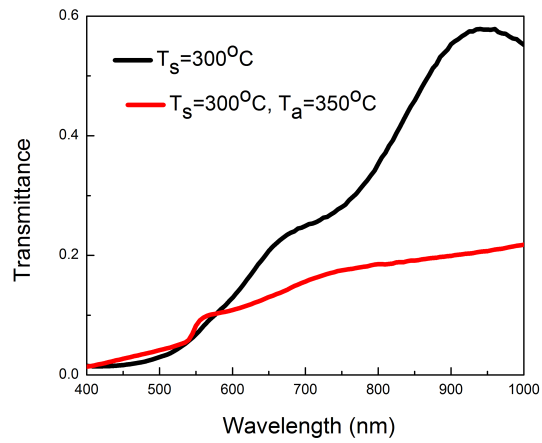
**Figure 3. 25** SEM images of the ZnSnTe films (a) As-grown and (b) Annealed for 5 minutes (c) Annealed for 30 minutes

### 3.3.2 Optical Properties

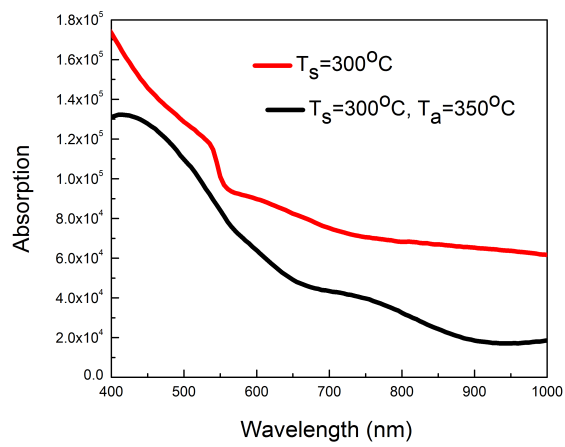
ZnTe is a material with high absorption coefficient and shows p-type behaviour. It has direct transition of wide band gap of 1.7 to 2.4 eV at room temperature. ZnTe films deposited on glass substrate in this study show  $E_g$  value between 2-2.1 eV. According to Figure 3.26 for both as-grown and annealed ZnTe the absorption value was in the range of  $10^5 \text{ (cm)}^{-1}$ , which implies that ZnTe is a good p-type material to absorb the highest possible value of the light.

The absorption, transmittance spectra and Tauc plots of different ZnSnTe films are given in Figure 3.27 and 3.28. The room temperature optical measurements of ZnSnTe films exhibited direct band gap around  $E_g=1.8\text{-}2.3$  eV. The transmittance and reflection values of ZnSnTe films are lower than 30% and 40% respectively, which shows that sputtered ZnSnTe film is a good candidate for p-type layer in ETA solar cell applications. It is observed that ZnSnTe film with five minutes annealing time is the best suitable layer as p-type wide band gap material.

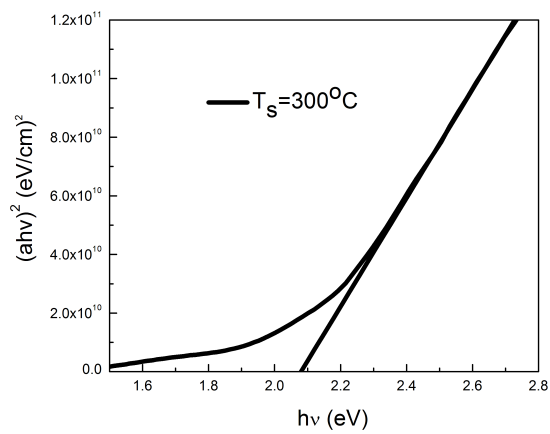




(a)

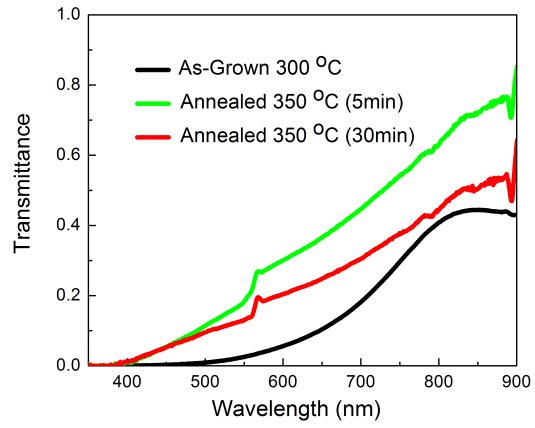


(b)

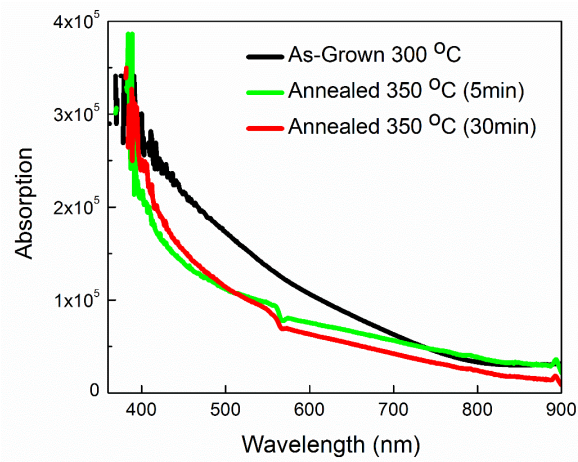


(c)

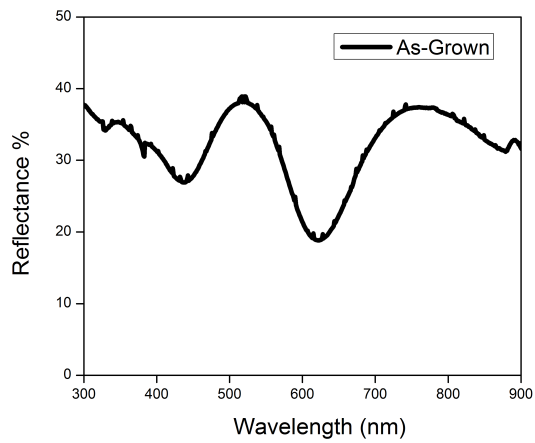
**Figure 3. 26** (a) Transmittance spectra (b) Absorption spectra and (c) Tauc plot of sputtered ZnTe films



(a)



(b)



(c)

**Figure 3. 27** (a) Transmittance spectra (b) Absorption spectra and (c) Reflection spectrum and Tauc plot of sputtered ZnSnTe films

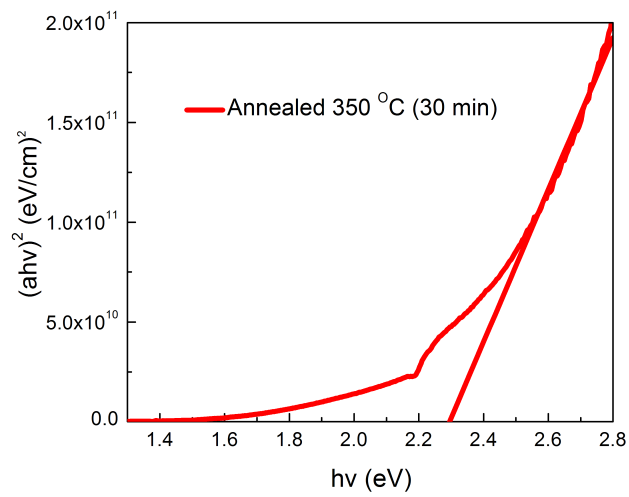
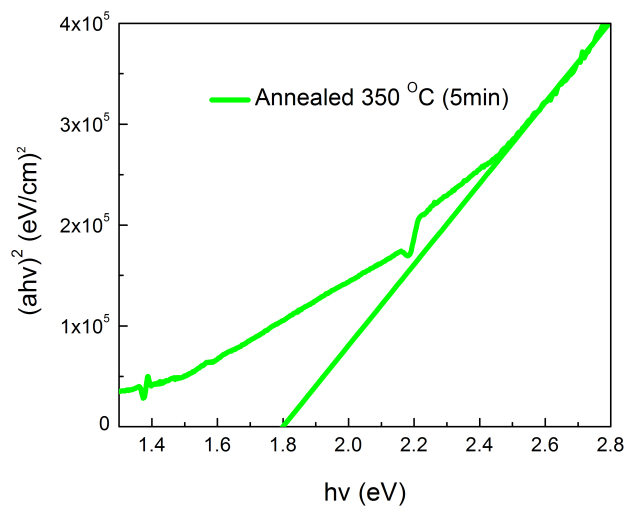
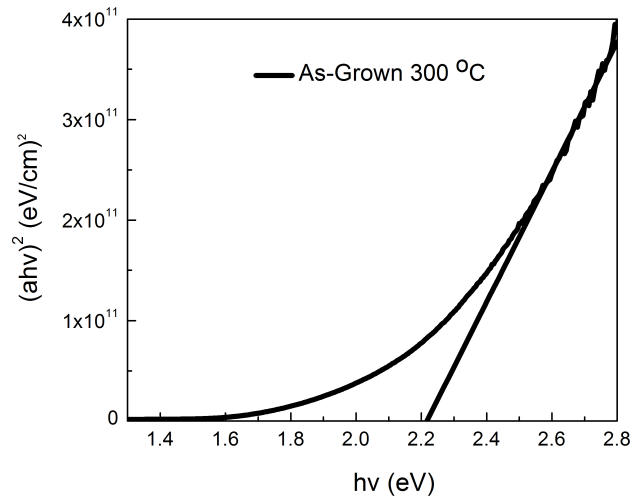


**Figure 3. 28** Tauc plots of sputtered ZnSnTe films

### 3.4 Conclusion

As the n-type wide band gap material, rutile phase hydrothermally grown nanowire and anatase phase electrochemically anodized nanotube  $\text{TiO}_2$  layers were studied. It is observed that for the spin coated nano-porous  $\text{TiO}_2$  the presence of thin and compact layer of sputtered  $\text{TiO}_2$  layer is demanded in order to prevent the shunting between FTO and CdTe absorber layer through the pores of nano-porous  $\text{TiO}_2$ . The band gap and transmittance values for all layers were found to be suitable to be used as the window layer. The suitable n-type  $\text{TiO}_2$  material to be used for ETA solar cell structure was found to be rutile phase hydrothermally grown nanowires since it was highly crystalline in nature, compared to other  $\text{TiO}_2$  layers studied in this thesis.

Both sputtered and electrodeposited CdTe layers were studied. It is observed that the electrodeposited CdTe layer showed the best crystallinity and also the band gap of electrodeposited CdTe layer was closer to the optimum band gap as the absorber layer.

As the p-type material ZnTe and ZnSnTe were studied, due to the high resistance values of ZnTe, low resistance ZnSnTe material observed to be the wide band gap p-type layer.

### 3.5 References

- [1] E.V. Buta, P. Pascariu, F. Prihor et al, Scientific Annals of “Alexandru Ioan Cuza DIN Iasi” University, (2008), p.5
- [2] M. Selmi, F. Chaabouni, M. Abaab, and B. Rezig, *hys. stat. sol. (c)*. 5 (10) (2008), p. 3368
- [3] A. Ashour, *Surf. Rev. Lett.* 13 (2006), p. 87
- [4] K. Tennakone, G.R.R.A. Kumara, I.R.M.Kottega, V.P.S. Perera, G.M.L.P. Aponsu, *J. Phys. D: Appl. Phys.: Appl Phys.*, 31 (1998), p. 2326
- [5] A. Hosseini, K.Ç. İçli, M. Özenbaş, Ç. Erçelebi, *Energy Procedia*, 60 (2014), p. 191
- [6] T. Brock, M. Groteklaes, P. Mischke, *European coatings handbook*, Vincentz Network GmbH & Co KG Vince.
- [7] A. E. Jiménez González, S. G. Santiago, *Semicond. Sci. Technol.* 22 (2007), p. 709
- [8] M. Singh, D. Pathak, A. Mahajan, R. K. Bedi, *J. Optoelectron Adv M.* 14 (2012), p. 624
- [9] A. Mohammadpour, *Synthesis and Characterization of TiO<sub>2</sub> Nanowire and Nanotube Arrays for Increased Optoelectronic Functionality*, Ph.D. Thesis, University of Alberta, 2014
- [10] M.A. Islam et al, *Current Applied Physics*, 13 (2) (2013), p. S115
- [11] M. Rami, E. Benamar, M. Fahoume, F. Chraibi, and A. Ennaoui, *M.J. Condensed Matter*, 3(1) (2000), p. 66
- [12] R.K. Pandey, S. Mafi, L. Peraldo Bicelli, *Materials Chemistry and Physics*, 37 (1994), p. 141
- [13] H. Bellakhder, A. Outzourhit, E.L. Ameziane, *Thin Solid Films*, 382 (1–2) (2001), p. 30



## CHAPTER 4

### DEVICE CHARACTERIZATION AND FUTURE WORK

#### 4.1 ETA Solar Cell Characterization

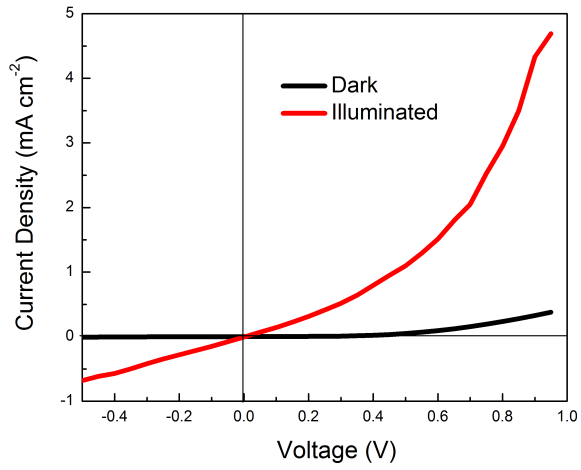
In this thesis, different two- and three-component ETA solar cells were fabricated and characterized. The spin coated nano-porous, sputtered thin film, hydrothermally grown nanowire and electrochemically anodized nanotube TiO<sub>2</sub> layers were used as the n-type wide band gap TiO<sub>2</sub> layer. The n-type nano structured TiO<sub>2</sub> layer was covered by the sputtered or electrodeposited CdTe material for two-component ETA solar cell structures. The thickness of CdTe layer was around 50 nm or less and between 150-250 nm for three- and two- component ETA solar cells respectively. The sputtered CdTe layer was followed by the void-filling hole-conducting p-type sputtered ZnTe or ZnSnTe layers for three-component ETA solar cell structures. The two- and three-component ETA solar cell structures were fullfilled with thermal evaporation of Au and In as the metallic contact. It should be mentioned that, for some of two-component devices a 10 nanometer Cu metal was evaporated prior to the Au evaporation for better adhesion of Au to the absorber material. In this chapter complete device structures, Glass/FTO/TiO<sub>2</sub>/Sputtered CdTe/Au, Glass/FTO/TiO<sub>2</sub>/Electrodeposited CdTe/Au and Glass/FTO/TiO<sub>2</sub>/Sputtered CdTe/ZnSnTe/In will be discussed in details to find the best working ETA solar cell structure. The illumination contact area for all the device structures in this study is 0.031 cm<sup>2</sup>.

##### 4.1.1 Devices with Sputtered CdTe Absorber Layer

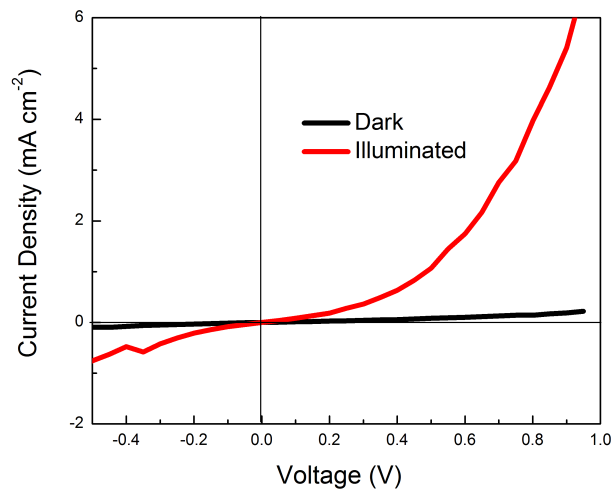
Two- and three-component ETA solar cells were fabricated with deposition of different n-type, p-type and absorber materials as explained in Chapter 3 and the characterization results will be presented in this chapter. TCO (FTO) coated glass slides covered by the nano structured TiO<sub>2</sub> films were used as the substrates for the

device structure. The CdTe films were coated using sputtering technique onto these substrates and Au contacts were evaporated thermally on the CdTe film for two-component ETA solar cells. As the p-type material for three-component ETA solar cells, ZnSnTe thin film was sputtered onto sputtered CdTe thin film absorber layer followed by the In metal evaporation. These steps were followed by annealing the Au and In contacts at 150 °C in nitrogen flow for 30 min. The typical J-V measurement results for two- and three-component ETA solar cells with sputtered CdTe layer, Glass/FTO/TiO<sub>2</sub>/Sputtered CdTe/Au and Glass/FTO/TiO<sub>2</sub>/Sputtered CdTe/ZnSnTe/In devices, for different nano structured TiO<sub>2</sub> layers in dark and under illumination are given in Figures 4.1 and 4.2. The J-V variations of both two- and three-component ETA solar cell structures show weak diode behaviour with small rectification ratio, which might be due to the interface recombination taking place in TiO<sub>2</sub>/CdTe interface resulting the loss of charge carriers at the junction. For both two- and three-component ETA solar cell structures, no light induced current was observed under the illumination, but they were all sensitive to the light. Figure 4.3 and 4.4 illustrate the J-V variations of Glass/FTO/TiO<sub>2</sub>/Sputtered CdTe(CdCl<sub>2</sub> treated)/Cu-Au and Glass/FTO/TiO<sub>2</sub>/Sputtered CdTe(CdCl<sub>2</sub> treated)/ZnSnTe/In devices with the sputtered+spin coated, nanotube and nanowire arrays of TiO<sub>2</sub> layers. For the samples presented in Figure 4.3 and 4.4 for two- and three-component ETA solar cell structures with sputtered CdTe absorber layer, CdCl<sub>2</sub> treatment was applied to the surface of CdTe thin film before annealing and 10 nm Cu was deposited onto the surface prior to the Au deposition for better adhesion and the formation of ohmic contact. As observed from the figure, light induced short circuit current and open circuit voltage appears with low values for device structures with the sputtered+spin coated and NTAs TiO<sub>2</sub> layers which might be due to the presence of the compact TiO<sub>2</sub> layer [1]; CdCl<sub>2</sub> treatment of the CdTe surface and Cu metal evaporation prior to Au evaporation which resulted a higher degree of crystallization for CdTe layer and better Au contact formation and adhesion. For the samples in Figure 4.4, the J-V curves show very similar behaviour observed for two-component ETA solar cells. Low photocurrent and photovoltage values were observed for the device structures with the buffer sputtered TiO<sub>2</sub> layer, NTAs and NWAs of TiO<sub>2</sub> layers after the CdTe surface was CdCl<sub>2</sub> treated.

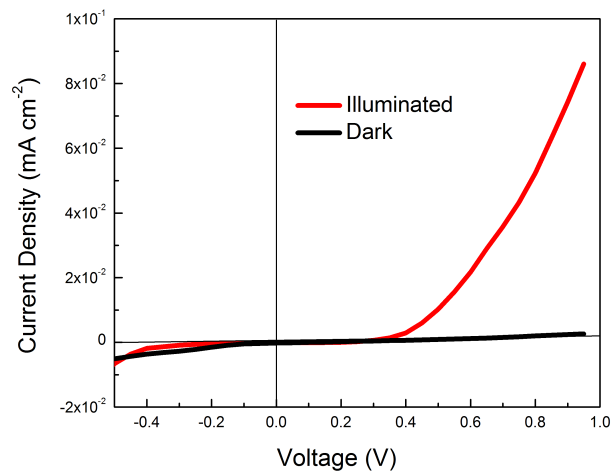




(a)

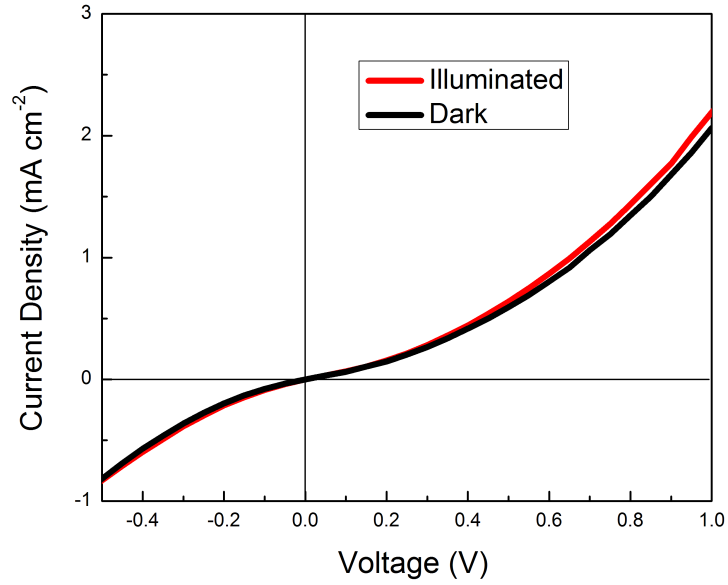


(b)

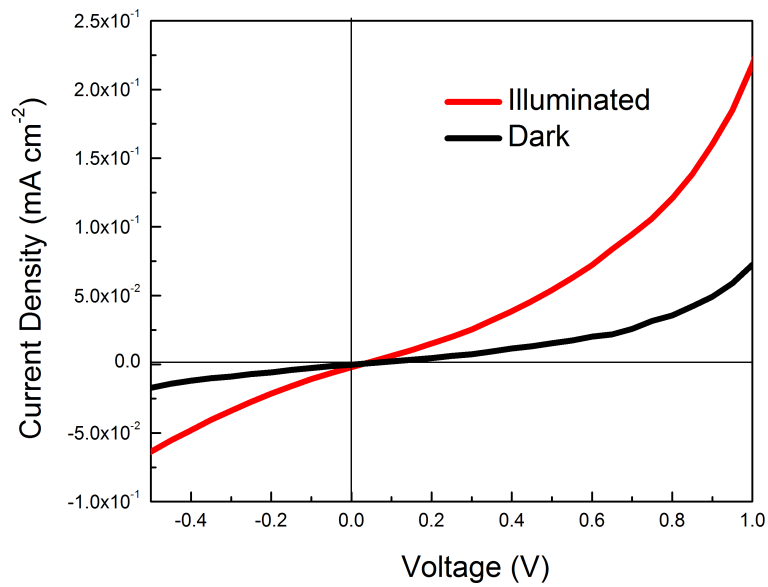


(c)

**Figure 4. 1** J–V characteristics of Glass/FTO/TiO<sub>2</sub>/Sputtered CdTe/Au devices with (a) Sputtered TiO<sub>2</sub> (b) Spin coated TiO<sub>2</sub> at 5000 rpm spin rate (c) Spin coated TiO<sub>2</sub> at successive spin rates of 2000-5000 rpm

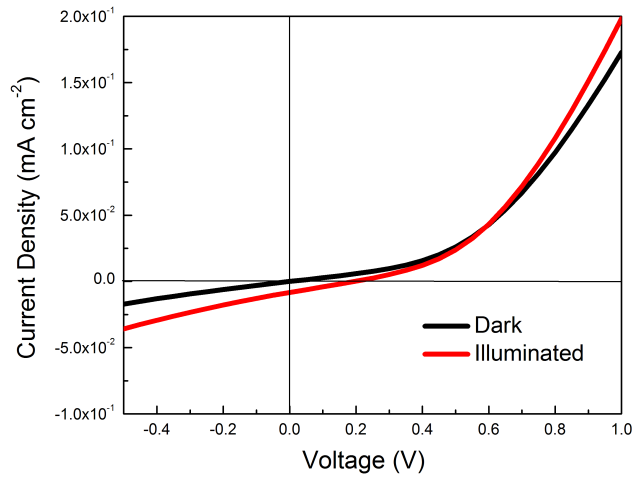


(a)

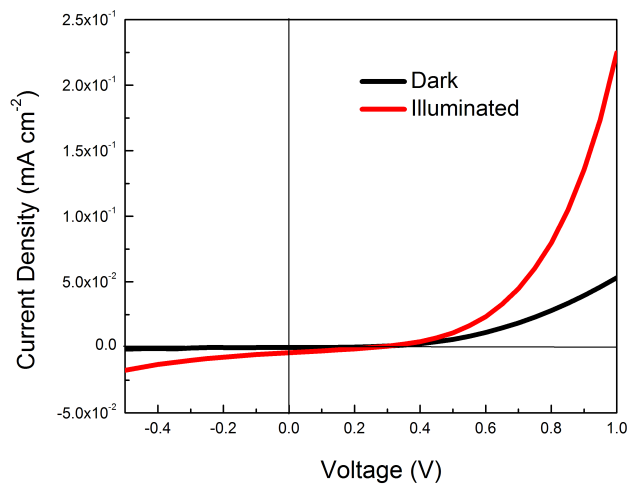


(b)

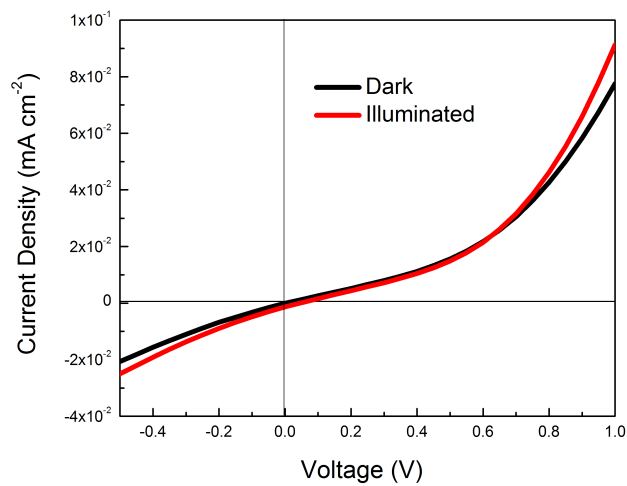
**Figure 4. 2** J–V characteristics of Glass/FTO/TiO<sub>2</sub> /Sputtered CdTe/ZnSnTe/In devices with (a) Spin coated TiO<sub>2</sub> at successive spin rates of 2000-5000 rpm (b) Sputtered TiO<sub>2</sub>+spin coated TiO<sub>2</sub> at successive spin rates of 2000-5000 rpm



(a)

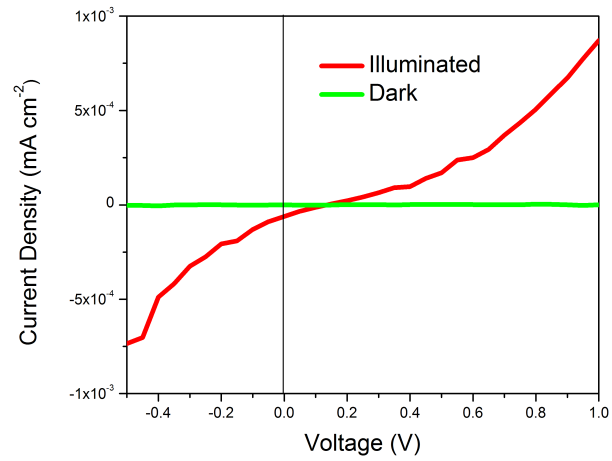


(b)

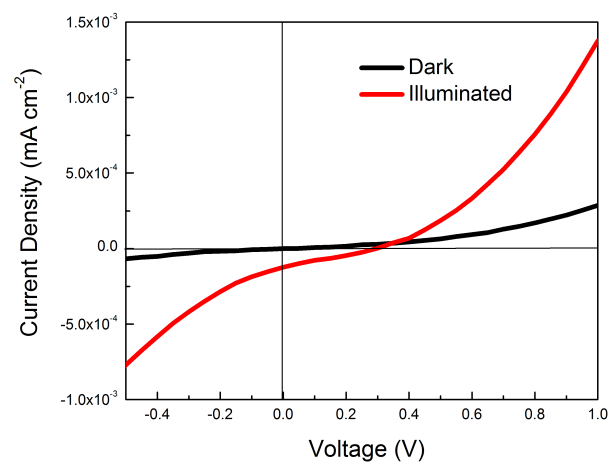


(c)

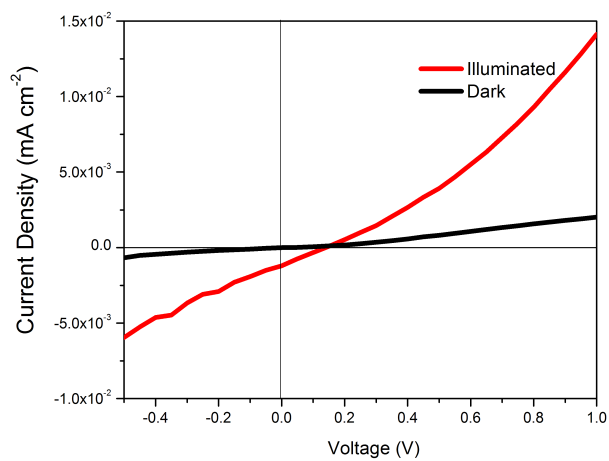
**Figure 4. 3** J–V characteristics of Glass/FTO/TiO<sub>2</sub>/Sputtered CdTe/Au devices with  
 (a) Sputtered TiO<sub>2</sub>+spin coated TiO<sub>2</sub> at successive spin rates of 2000-5000 rpm  
 (b) NTAs of TiO<sub>2</sub> (c) NWAs of TiO<sub>2</sub>



(a)



(b)

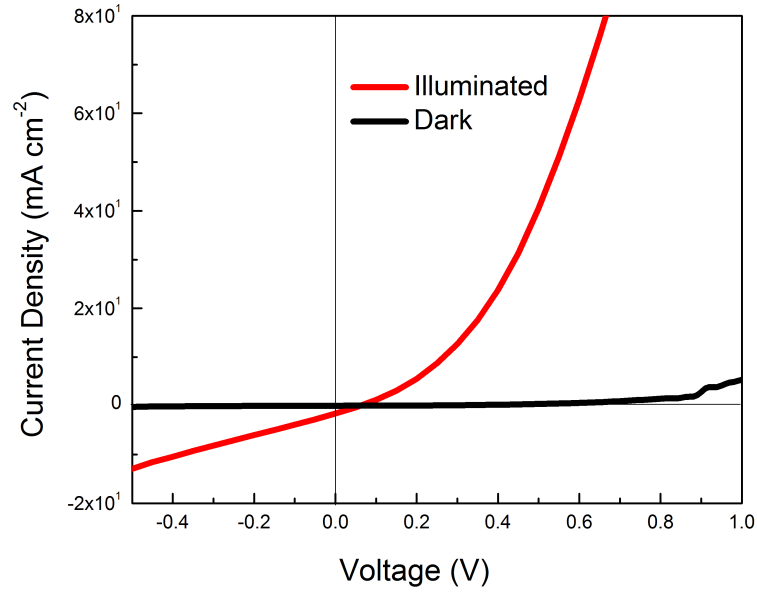


(c)

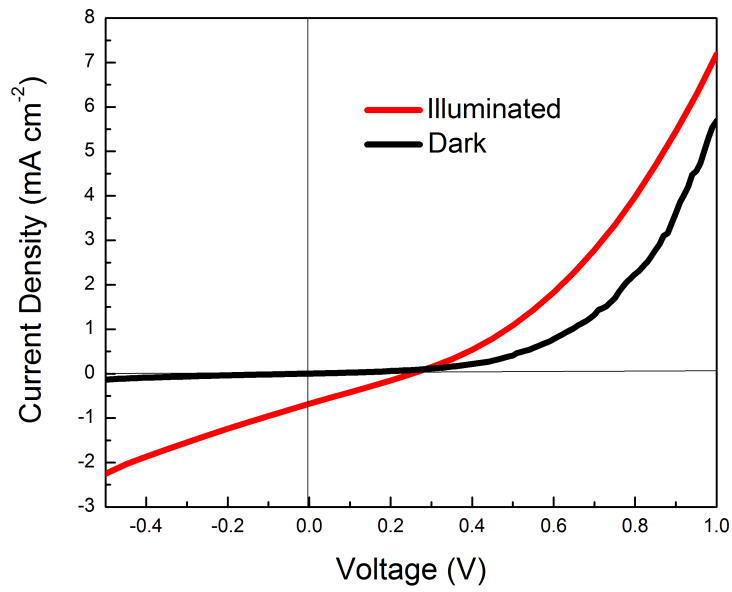
**Figure 4. 4** J–V characteristics of Glass/FTO/TiO<sub>2</sub> /Sputtered CdTe/ZnSnTe/In devices with (a) Sputtered TiO<sub>2</sub>+spin coated TiO<sub>2</sub> at successive spin rates of 2000- 5000 rpm (b) NTAs of TiO<sub>2</sub> (c) NWAs of TiO<sub>2</sub>

#### 4.1.2 Devices with Electrodeposited CdTe Layer

Some of the solar cell structures given in Section 4.1.1 were also studied with the CdTe thin absorber layer, which was coated by using electrodeposition technique. The current density-voltage characteristics of the solar cell structures with NWAs and NTAs of TiO<sub>2</sub> layers coated with electrodeposited CdTe followed by 10 nm Cu/ 40 nm Au metal contact evaporation, both in dark and under illumination are illustrated in Figure 4.5. It should be mentioned that for all solar cell structures with electrodeposited CdTe layer, CdCl<sub>2</sub> treatment was applied to the surface of the CdTe and all the devices without treatment, the same as for two- and three-component ETA solar cell structures with sputtered CdTe, no light induced current or voltage was observed. The samples presented in Figure 4.5 were annealed for 45 minutes under air ambient on hot plate at 350 °C after CdCl<sub>2</sub> treatment and prior to the contact evaporation. The solar cell structures of Glass/FTO/NWAs (NTAs) of TiO<sub>2</sub>/Electrodeposited CdTe /Cu-Au illustrated in Figure 4.5 show typical diode behaviour with low light induced current and voltage when compared to the devices with sputtered CdTe. The open circuit voltage ( $V_{oc}$ ), short circuit current density ( $J_{sc}$ ), fill factor (FF) and power conversion efficiency ( $\eta$ ) are about 60 mV, 1.60 mA cm<sup>-2</sup>, 0.14%, 0.014% and 260 mV, 0.68 mA cm<sup>-2</sup>, 0.24% , 0.042% for the devices with NTAs and NWAs of TiO<sub>2</sub> layers respectively. In order to improve the obtained results, the two-component ETA solar cell structures with NWAs TiO<sub>2</sub> and electrodeposited CdTe absorber layers were subjected to further study regarding the annealing temperature and time. Figure 4.6 illustrates the J-V variation of the same solar cell structure for NWAs TiO<sub>2</sub> of Figure 4.5 when subjected to annealing at 350 °C for 15 minutes, followed by annealing at 400 °C for 15 minutes. The device showed the  $V_{oc}$ ,  $J_{sc}$ , FF and EF to be 200 mV, 0.4 mA cm<sup>-2</sup>, 0.28% and 0.02% respectively. The samples showed better fill factor but lower efficiency when compared to that for the sample annealed at 350 C<sup>0</sup> for 45 minutes presented in Figure 4.5, which may be due to the higher degree of crystallinity for the samples annealed at 350 °C for 45 minutes.



(a)



(b)

**Figure 4. 5** J–V characteristics of (a) FTO/NTAs of  $\text{TiO}_2$ /Electrodeposited CdTe/ Cu-Au (b) FTO/ NWAs of  $\text{TiO}_2$ /Electrodeposited CdTe/Cu-Au solar cells annealed at  $350^\circ\text{C}$  for 45 minutes

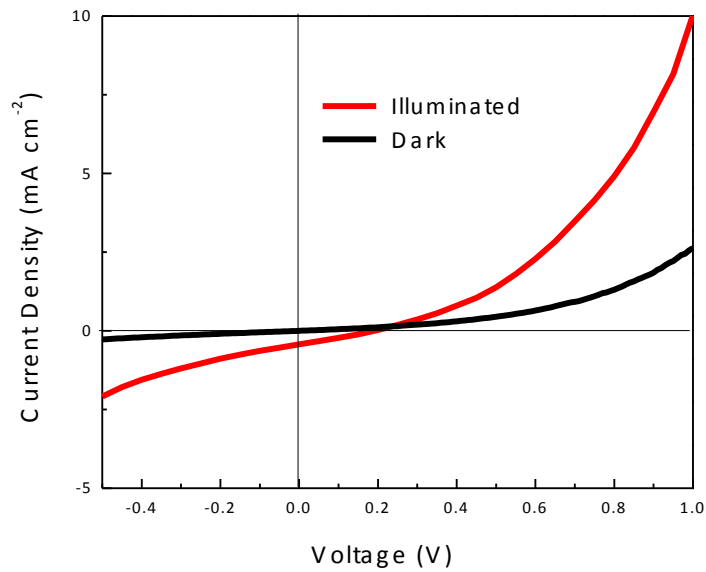


**Figure 4. 6** J–V characteristics of FTO/ NWAs of TiO<sub>2</sub>/Electrodeposited CdTe/ Cu- Au solar cell annealed at 350 °C for 15 minutes, followed by annealing at 400 °C for 15 minutes

The J-V variation of the samples, after being annealed at 350 °C for 60 minutes followed by annealing at 400 °C for 30 minutes, are given in Figure 4.7. As observed in figure, J-V variations both in dark and under illumination had typical photovoltaic diode behaviour with better rectification. The  $V_{oc}$ ,  $J_{sc}$ , FF and EF were extracted from illuminated J-V curve to be about 0.6 V, 3.57 mA cm<sup>-2</sup>, 0.44%, and 0.96% respectively. As mentioned before this result might be due to the formation of better crystallinity of the electrodeposited CdTe layer and the formation of the better ohmic contact between CdTe and Au after being annealed for longer time.

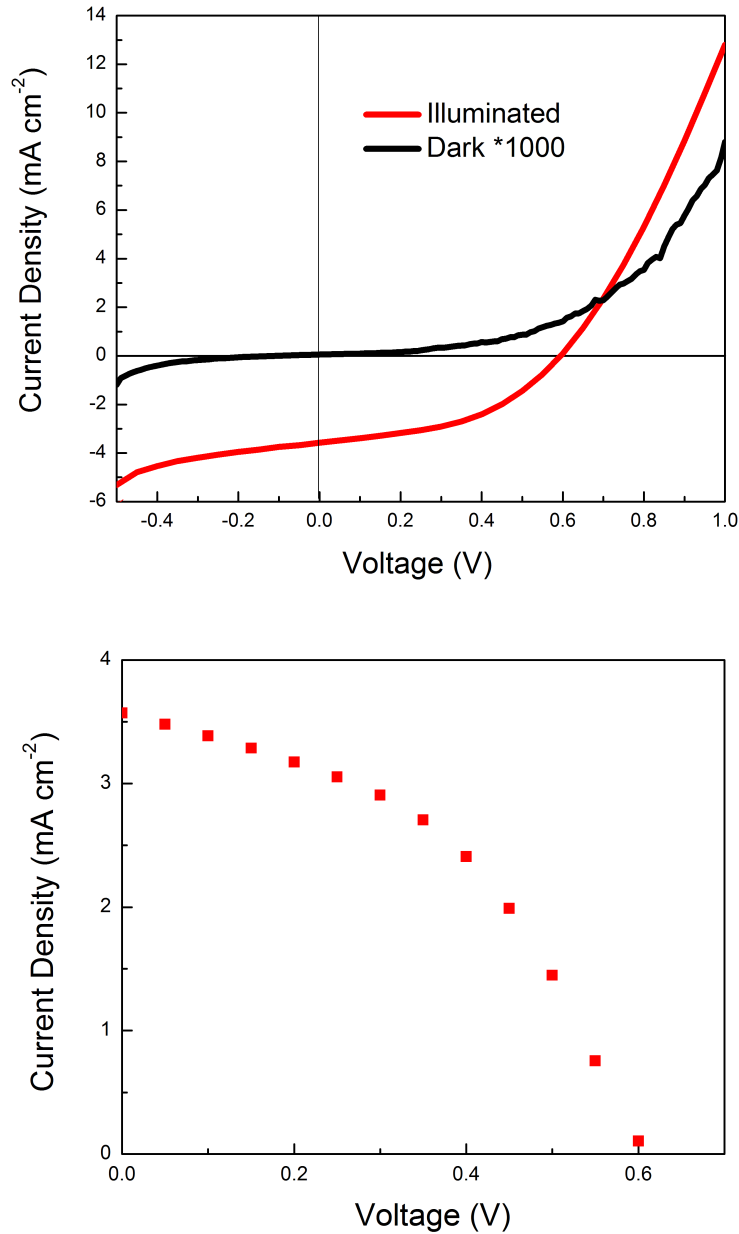


**Figure 4. 7** Dark and illuminated J–V characteristics of FTO/NWAs of TiO<sub>2</sub>/Electrodeposited CdTe/Cu-Au solar cell annealed at 350 °C for 60 minutes followed by annealing at 400 °C for 30 minutes

The  $R_s$  and  $R_{sh}$  values, determined from the slope of I-V curve at  $V_{OC}$  and  $I_{SC}$  were found as  $58 \Omega \text{cm}^2$  and  $548 \Omega \text{cm}^2$ . Both  $R_s$  and  $R_{sh}$  have high values, where the  $R_s$  and  $R_{sh}$  are respectively 0 and  $\infty$  for the ideal cell to have the maximum fill factor and efficiency. As it is mentioned in Section 2.4.6.3,  $R_s$  is due to both bulk material and



contacts of the device, where  $R_{sh}$  is due to leakage in the cell such as presence of pinholes. In order to improve the 1% efficiency, the  $TiO_2/CdTe$  interface should be engineered, CdTe layer thickness can be decreased, the  $CdCl_2$  and annealing treatments should be optimized and finally for the contact improvement, the contacts can be subjected to further annealing study. Both  $CdCl_2$  treatment and annealing are important factors for high efficiency cells and should be optimized.

To the best of our knowledge; there are limited studies on nanostructured  $TiO_2/CdTe$  solar cell structure and this is the first time that rutile phase of  $TiO_2$  NWAs is coated with electrodeposited CdTe layer. Konenkamp et al. proposed the two-component porous anatase phase  $TiO_2$  coated with 150-250 nm electrodeposited ETA CdTe layer [2]. Mengyao et al. worked on core-shell structure of anatase phase  $TiO_2$  nanotubes coated with a electrodeposited CdTe and they obtained 0.1% efficiency [3] Karaagac et al. studied  $CdTe/TiO_2$  heterojunction core-shell solar cell by sputtering CdTe on nano-rod  $TiO_2$  layer and they obtained efficiency about 0.12% [4]. The obtained efficiency for this novel structure is 0.96%, which can be increased by improving the quality of both layers such as morphology of  $TiO_2$  nanowires and electrical properties of CdTe and also optimizing the  $CdCl_2$  treatment, which increases the grain size and as the result the recombination probability decrease. This two-component ETA solar cell structure should be optimized by decreasing the CdTe layer thickness to less than 50 nm down to 20 nm to be best suitable for ETA solar cell structure. Also the incorporation of CuSCN and ZnSnTe as the p-type layer on this structure can be a target for the three-component ETA solar cell structure. Since the NWAs  $TiO_2$ /electrodeposited CdTe/Cu-Au ETA solar cell device structure resulted the best device parameters with the highest efficiency, the structural, morphological and optical characterizations of NWAs  $TiO_2$ /Electrodeposited CdTe junction were studied in detail and results are introduced in the following section.

#### **4.2 Structural, Morphological and Optical Characterizations of NWAs $TiO_2$ /Electrodeposited CdTe Junction**

Figure 4.8 show the cross-sectional and top SEM images of NWAs  $TiO_2$ /Electrodeposited CdTe solar cell device. Images show the successful growth of

homogenous CdTe layer on NWAs of TiO<sub>2</sub>. The 1 μm length and 80 nm width TiO<sub>2</sub> NWAs were coated with electrodeposited CdTe with thickness between 125-250 nm. The CdTe coating was homogeneously distributed onto the TiO<sub>2</sub> NWAs on the surface (Figure 4.8 b and c). The solar cell structure mentioned here can be optimized by decreasing the thickness of CdTe absorber layer.

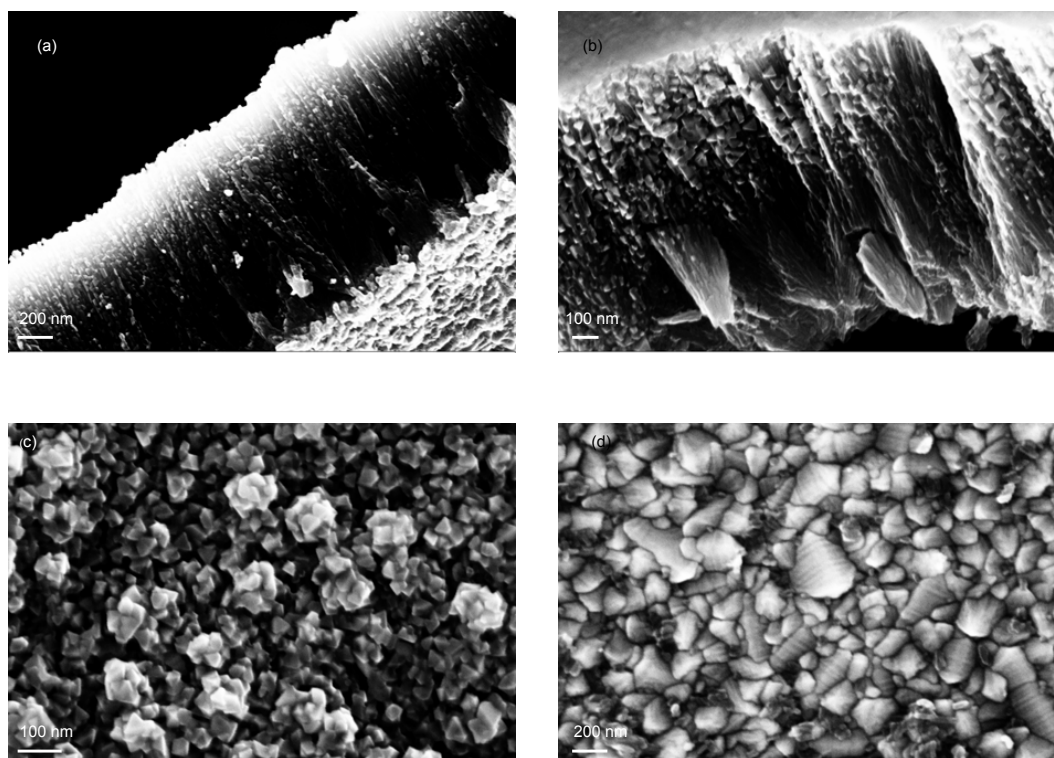


**Figure 4. 8** SEM images of the (a),(b) Cross-sectional view of NWAs of TiO<sub>2</sub>/Electrodeposited CdTe solar cell (c), (d) Top images of NWAs of TiO<sub>2</sub>/Electrodeposited CdTe solar cell

XRD measurement was performed to identify the existing phases in FTO/NWAs TiO<sub>2</sub>/Electrodeposited CdTe structure. Figure 4.9 shows the XRD plot for electrodeposited CdTe on TiO<sub>2</sub> NW layer. The XRD result is in consistent with SEM images and shows that CdTe is deposited on TiO<sub>2</sub> NWAs with rutile phase. The observed peaks are associated with FTO, TiO<sub>2</sub> NW and CdTe whereas TiO<sub>2</sub> and CdTe [5] have rutile and cubic crystal structure respectively.

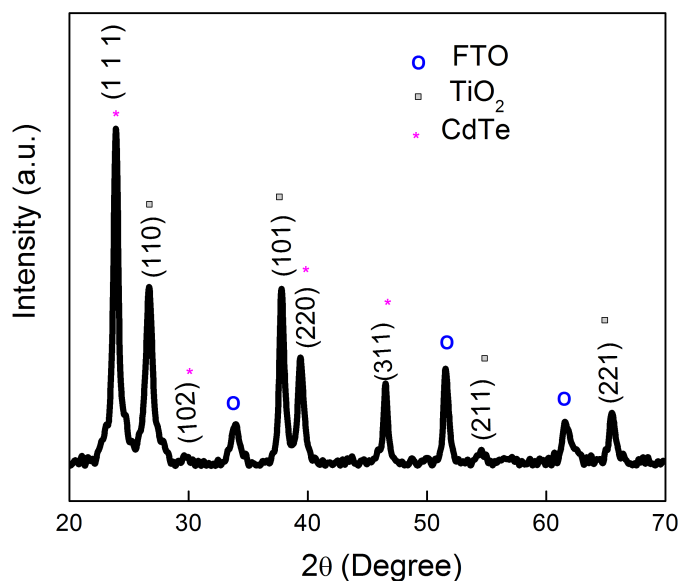
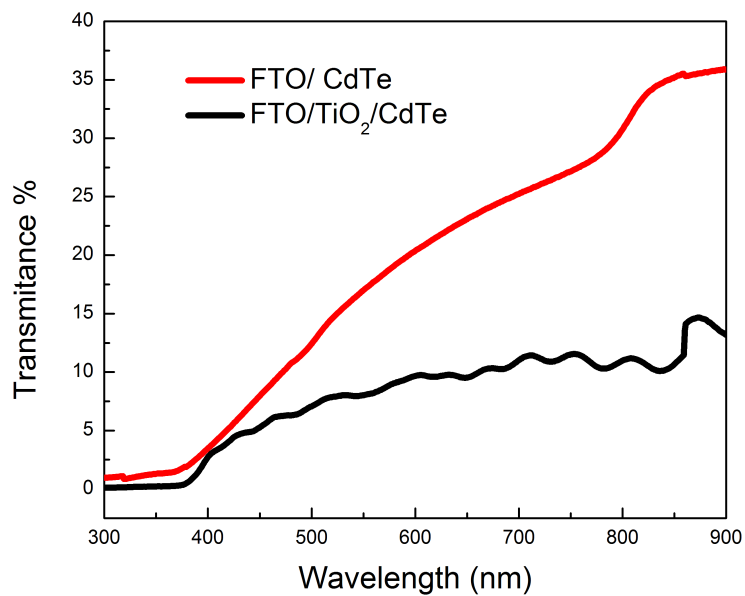


**Figure 4. 9** XRD pattern for electrodeposited CdTe on NWAs of TiO<sub>2</sub>

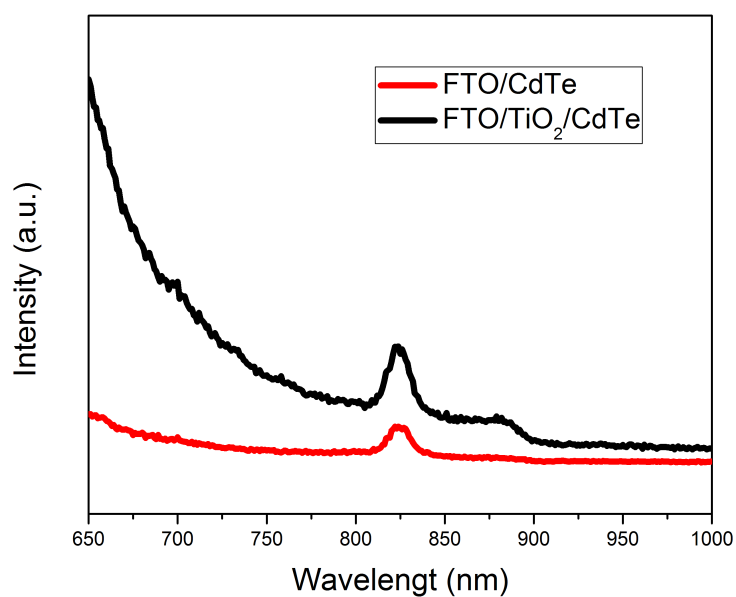
The transmittance spectra for FTO/CdTe and FTO/TiO<sub>2</sub>/CdTe structures are given in Figure 4.10 (a) for ultraviolet–visible near-infrared (UV-VIS-NIR) range in the 300–900 nm wavelength range. The FTO/CdTe structure transmits the light up to 35%, where the structure with a TiO<sub>2</sub> NWAs as the wide band gap n-type material transmits less than 13% for the mentioned wavelength region. The observed results show the role of TiO<sub>2</sub> NW in the structure. Because of the presence of nano structured rutile phase TiO<sub>2</sub> NWAs in the structure, an extra light absorption occurs in the FTO/TiO<sub>2</sub>/CdTe, which is called light trapping. The use of nano structured TiO<sub>2</sub> improves the photovoltaic behaviour, this should be due to the larger surface area of TiO<sub>2</sub> and better light harvesting in the TiO<sub>2</sub>/CdTe junction for nanostructured cell compared to planar layer based solar cells.

The band gap of the CdTe absorber layer was obtained from PL spectra as shown in Figure 4.10 (b). A narrow full-width-at-half maximum (FWHM) in the PL spectra confirms the narrow size distribution of CdTe molecules. The observed peak at ~825 nm corresponds to the CdTe band gap of 1.5 eV [6] which is close to the optimum value for photovoltaic performance (1.4 eV) and will result higher efficiencies. This

combination of n-type wide band gap  $\text{TiO}_2$  and low band gap CdTe absorber layer structure can absorb a wide range of solar spectrum.



(a)



(b)

**Figure 4. 10** (a) Transmittance spectra (b) Room temperature PL curves for FTO/Electrodeposited CdTe and FTO/NWAs  $\text{TiO}_2$ /Electrodeposited CdTe structures

### 4.3 Future Work

As the future work we propose the investigation of the thickness optimization of electrodeposited CdTe layer. For this purpose, the finite element method (using COMSOL) was used for optical simulations in this thesis study. We calculate the optical absorption of Glass/FTO/NWAs TiO<sub>2</sub>/Electrodeposited CdTe/Au structure under AM 1.5 illumination, where the light passes the structure through the FTO layer. For the ease of simulation, EQE is considered as 1. This method calculates all the absorptions including parasitic absorption from all the materials used for fabrication of this structure. Optical and electronic properties of the materials used in simulations are taken from literature [7-9]. In order to get rid of the parasitic absorption we calculated only the short circuit current flux of CdTe layer. In our simulation the design was used with 200 nm FTO, 500 nm bulk TiO<sub>2</sub> layer with 1 μm and 2.5 μm TiO<sub>2</sub> NWAs where the separation distances between wires was 50 nm and 100 nm of Au layer. The CdTe layer thicknesses used for simulation in this study are 10, 20, 30, 40, 50, 100, 150, 200, 250 nm. The wavelength range is taken between 300-900 nm, which covers the band edges of all materials in this structure

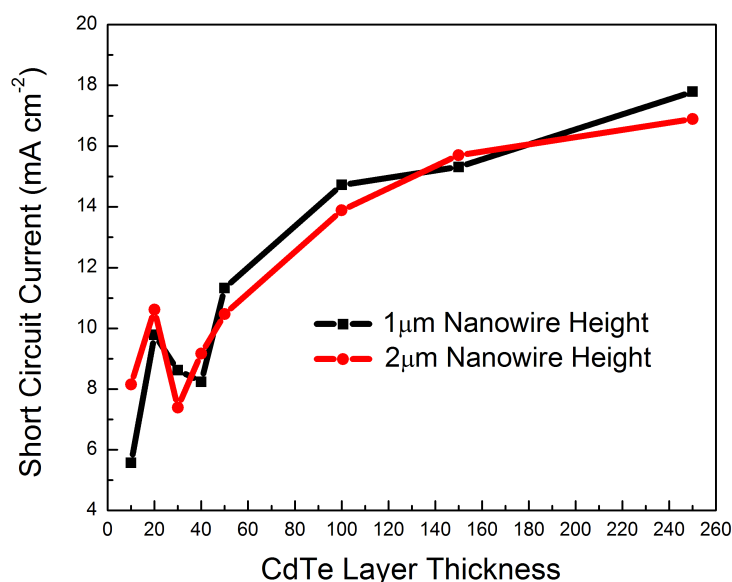


**Figure 4. 11** Short circuit values versus CdTe layer thickness obtained using simulation of Glass/FTO/NWAs TiO<sub>2</sub>/Electrodeposited CdTe/ Au structure

In Figure 4.11, the short circuit current values obtained using simulation of Glass/FTO/NWAs TiO<sub>2</sub>/Electrodeposited CdTe/ Au structure for different CdTe thicknesses and TiO<sub>2</sub> wire lengths are presented. The simulations showed that for CdTe layer with thicknesses less than 50 nm, the 20 nm, ETA cell structure showed the best J<sub>sc</sub> while the J<sub>sc</sub> value was low compared to 250 nm thick CdTe layer. The increase of J<sub>sc</sub> values for CdTe thickness above 50 nm showed a monolithic trend for both TiO<sub>2</sub> wire length of 1 and 2.5 μm. We suggest the presence of extremely thin 20 nm CdTe layer as the absorber for nanowire TiO<sub>2</sub> based solar cells and incorporation of CuSCN or ZnSnTe as the p-type layer on FTO/NWAs TiO<sub>2</sub>/Electrodeposited CdTe solar cell structure. Figure 4.12 shows the absorption profile of the Glass/FTO/NWAs TiO<sub>2</sub>/Electrodeposited CdTe/Au structure. Even if we expect higher values of light absorption for higher NWAs of TiO<sub>2</sub>, it is observed the majority of light is absorbed in CdTe layer near to CdTe/TiO<sub>2</sub> interface, where the absorption wavelength of light corresponds to CdTe layer bandgap.

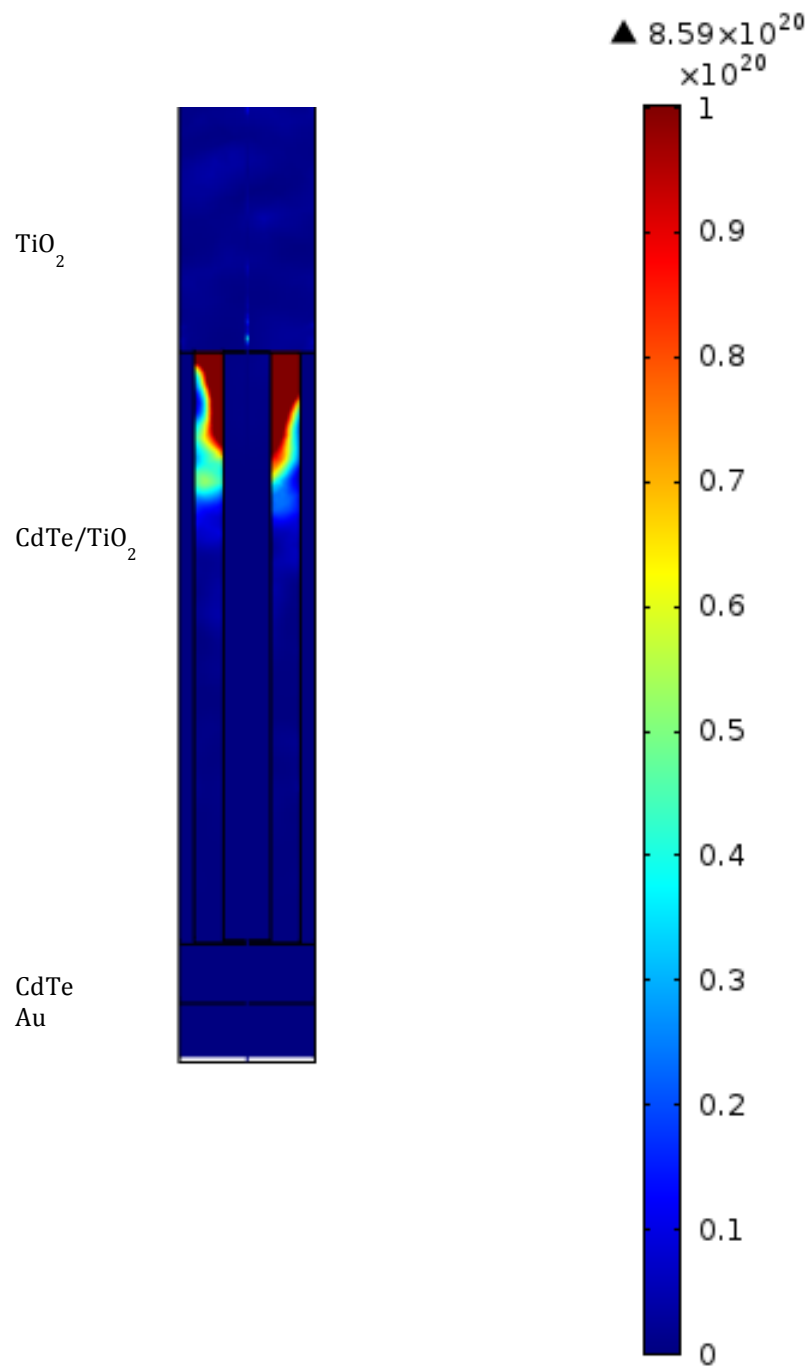


**Figure 4. 12** Absorption profile in Glass/FTO/NWAs  $\text{TiO}_2$ /Electrodeposited CdTe/Au structure as a function of  $\lambda$  for 300-900 nm

#### 4.4 References

- [1] M. Lux-Steiner et al, International Journal of Energy Engineering 3(3) (2013), p. 183
- [2] A. Belaïdi, R. Bayon, L. Dloczik, K. Ernst, M.C. Lux Steiner, R. Könenkamp, Thin Solid Films, 431–432 (2003), p. 488
- [3] M. Zhang et al, J. Mater. Chem., 22 (2012), p. 10441
- [4] H. Karaagac, M. Parlak, L.E. Aygun, M. Ghaffari, N. Biyikli, A.K. Okyay, Scripta Materialia, 69 (2013), p. 323
- [5] K. R. Murali, B. Jayasutha, Mater. Sci. Semicond. Process, 10 (2007), p. 36
- [6] A. Y. Shenouda, M. El Sayed, Ain Shams Engineering Journal, 6(1) (2015), p. 341
- [7] J. M. Ball et al, Energy Environ. Sci., 8 (2015), p. 602
- [8] Ch. W. Chen et al, J. Mater. Chem. A, 3 (2015), p.9152
- [9] A.D. Rakic, A. B. Djuricic, M. L. Majewski, Appl. Opt., 37 (1998), p.5271



## CHAPTER 5

### CONCLUSIONS

In this study two- and three-component ETA solar cell structures with CdTe absorber layer were prepared and characterized. The band alignment of the ETA solar cell structure, which was described theoretically in Chapter 1, was such that the visible light is absorbed by CdTe layer and the excited electrons and holes are conducted to the n-type TiO<sub>2</sub> layer and to the electrode through CdTe and ZnSnTe for two-component and three-component ETA solar cells respectively to contribute to the photo generated current.

As the n-type window layer the spin coated nano-porous, sputtered thin film, hydrothermally grown nanowire and electrochemically anodized nanotube TiO<sub>2</sub> layers were used. The wide band gap TiO<sub>2</sub> layer was covered by sputtered or electrodeposited CdTe layer. It was followed by the void-filling hole-conducting p-type sputtered ZnTe or ZnSnTe layers. All these layers were individually characterized structurally, morphologicaly, optically and electrically in detail to identify the optimum fabrication conditions for different layers to be used in ETA solar cell structures, which lead the high device efficiency. The complete two- and three-component device structure were fulfilled by thermal evaporation of Au and In metal contact onto the structures respectively. The complete laboratory scale ETA solar cell devices of Glass/FTO/TiO<sub>2</sub>/CdTe/Au and Glass/FTO/TiO<sub>2</sub>/CdTe/ZnSnTe/In were produced and characterized to investigate the efficient ETA solar cell structures. For some of two-component devices a 10 nanometer Cu metal was evaporated prior to the Au evaporation due to better formation and adhesion of contact.

For two- and three-component Glass/FTO/TiO<sub>2</sub>/Sputtered CdTe/Au and Glass/FTO/TiO<sub>2</sub>/Sputtered CdTe/ZnSnTe/In structures with CdCl<sub>2</sub> treatment of the CdTe surface and Cu metal evaporation prior to Au evaporation, the films show weak diode behavior with small rectification ratios. Also low values of light induced short circuit current and open circuit voltage appears. It should be mentioned that, for both

two- and three-component ETA structures without CdCl<sub>2</sub> treatment and Cu evaporation, no photocurrent or photovoltage values were obtained.

The two-component Glass/FTO/TiO<sub>2</sub>/Electrodeposited CdTe/Cu-Au solar cell structures, with electrodeposited, CdCl<sub>2</sub> treated CdTe layer and nano structured NWAs and NTAs of TiO<sub>2</sub> layer, showed typical diode behaviour with low light induced current and voltage values. The samples which were annealed for 45 minutes under air ambient on a hot plate at 350 °C showed FF and  $\eta$  about 0.14%, 0.02 % and 0.24% , 0.04% for the devices with NTAs and NWAs of TiO<sub>2</sub> layers respectively. The two-component ETA solar cell structure with NWAs TiO<sub>2</sub> and electrodeposited CdTe absorber layers with higher efficiency value was subjected further study regarding the annealing temperature and time to improve the photovoltaic behaviour and optimize the structure. It was observed that for CdTe layer which was annealed at 350 °C for 60 minutes followed by annealing at 400 °C for 30 minutes, both dark and under illumination behaviour showed typical photovoltaic diode behaviour with better rectification with V<sub>oc</sub>, J<sub>sc</sub>, FF and  $\eta$  values as 0.6 V, 3.57 mA cm<sup>-2</sup>, 0.44%, and 0.96% respectively. The annealing provided the formation of better crystallinity of the electrodeposited CdTe layer. For the two-component ETA structures without CdCl<sub>2</sub> treatment and Cu evaporation, photoconductivity was observed for the structure and but no photocurrent and photovoltage values were obtained.

The ETA solar cell structures with electrodeposited CdTe layers, were found to have the highest efficiency of 0.96%. In fact, it was the first time which rutile phase NWAs TiO<sub>2</sub> with high crystallinity was used as n-type wide band gap material in ETA structures. It was observed that, the CdTe thin film grown by the electrodeposition method showed better crystallinity. Also, it is worth to mention that, the solution based CdTe layer fills the pores of nano structured TiO<sub>2</sub> substrates in a better way compared to the sputtered CdTe, resulting better light harvesting in the TiO<sub>2</sub>/CdTe junction for nanostructured cell. It should be mentioned that CdCl<sub>2</sub> treatment of CdTe layer is crucial to fabricate efficient solar cells.

The obtained 0.96 % efficiency for this novel structure can be increased by improving the quality of both layers such as morphology of TiO<sub>2</sub> nanowires, electrical properties of CdTe, optimizing the CdCl<sub>2</sub> treatment, ohmicity of the Au contact and decreasing the thickness of CdTe layer. For the future work, as shown by simulation the CdTe layer thicknesses will be decreased upto less than 20 nm, to have the best suitable thickness value for for ETA solar cell structures. Also the incorporation of CuSCN

and ZnSnTe as the p-type layer on this structure will be ultimate target for the three-component ETA solar cell structure.



## CURRICULUM VITAE

AREZOO HOSSEINI

---

Date of birth: 12.09.1985

Email: Hosseiniarezu1364@gmail.com

Cell: (+90)507-798-5085

### Education

Islamic Azad University, Iran

Sept. 2003

B.S. in Physics, GPA: 17.19 / 20

– Jul. 2007

Islamic Azad University, Iran

Sept. 2007

M.S. in Physics, GPA: 16.89 / 20

– Sept. 2009

Study of the Two-level atom interacting with a single mode quantum field using quantum averaging method

Middle East Technical University (METU), Ankara,  
Turkey

Feb. 2010

– Present

Ph.D. Candidate, (Expected graduation: Jan. 2016),

GPA: 3.38 / 4.0

Fabrication and Investigation of Extremely Thin CdTe  
Absorber Layer Solar Cells

### Professional Experience

- More than 3 year of cleanroom experience, Film Deposition (Sputtering, Spin-Coating, Thermal, Hydrothermal, Electrodeposition, Electrochemical Anodization), SEM Imaging, AFM Imaging, UV-Vis Spectroscopy, X-ray crystallography, I-V measurements experience, (Middle East Technical University, Turkey)

### Professional Affiliations:

- Teaching assistant, Azad University
- Researcher, Young Researchers Club, Azad University

### Awards and Honors

- The Selected Candidate in Turkey to Receive the 1002 - Short Term R&D Funding Program of The Scientific and Technological Research Council of Turkey.
- The Selected Candidate in Turkey to Receive the 2215 Graduate Scholarship Program For International Students of The Scientific and Technological Research Council of Turkey.
- Ranked between first 7, among Physics B.Sc. Students of Azad University.

### Major Research Projects

- 1002 Short Term R&D Funding Program of The Scientific and Technological Research Council of Turkey “Fabrication and investigation of Extremely Thin Absorber layer-ETA solar cells”
- A Scientific and Technological Research Council of Turkey (TUBITAK) project between Turkey and Africa, “Design and Production of High Efficiency and Low Cost Tandem Perovskite/Si Solar Cells”
- CMC project, “Fabrication of Extremely Thin Absorber (ETA) solar cells”, Alberta, Canada.

### Courses Attended

- Having certificate on Scanning Electron Microscope (METU)
- First workshop of essay writing for department of Basic Science, Young Researchers Club, Azad University
- Powder Diffraction Course for Ms/Phd Students (Hacettepe)
- EMRS SHORT COURSE Thin Films Growth by PVD Techniques (E-MRS 2014 Spring Meeting, France)

### Summer School

- The Exchange Program, Department of Electrical and Computer Engineering, Alberta, Canada, 22th June-22th October 2015

### Publications

#### Papers

- Hosseini. A, Icli. KC, Güllü. HH. “Preparation and characterization of porous TiO<sub>2</sub> thin films by sol- gel method for Extremely Thin Absorber-ETA solar cell applications”. J TJST 2013; 8(2): 69-79.
- Hosseini. A, Icli. KC, Ozenbas. M, Ercelebi. C, “Fabrication and Characterization of Spin-coated TiO<sub>2</sub> Films”. Proceedings of the E-MRS 2014 Spring Meeting, Energy Procedia. 2014; 60: 191–198.
- Hosseini. A, Güllü. HH, Coşkun. E, Parlak. M, Ercelebi. C. “Fabrication and Characterization of TiO<sub>2</sub> Thin Film for Device Applications”.
- Also as the result of my exchange program study at Alberta University, we will publish a paper on p-type electrodeposited CdTe absorber layer for solar cell application.

#### Posters

- “Device characterization of ITO/TiO<sub>2</sub>/CdTe/Au thin film heterojunction”, Yoğun Madde Fiziği, Izmir (Türkiye), 5 April 2013.

- “Saçtırma yöntemi kullanılarak üretilen TiO<sub>2</sub> ince filmlerde üretim süresinin yapı ve optik özelliklere etkisi”, 19.Yoğun Madde Fiziği, Ankara (Türkiye), 20 December 2013.
- “Fabrication and Characterization of TiO<sub>2</sub>Thin Films for Device Applications” E-MRS 2014 Spring Meeting, Lille (France), 26-30 May 2014.
- “Fabrication and characterization of spin-coated TiO<sub>2</sub> films”, E-MRS 2014 Spring Meeting, Lille (France), 26-30 May 2014.
- “Fabrication and Characterization of sputtered Zn-Sn-Te Thin Films for Extremely Thin Absorber-ETA Solar Cell Applications”, 29<sup>th</sup> EU PV Solar Energy Conference and Exhibition, Amsterdam (Netherlands), 22-26 September 2014.
- “Investigation of Si/ZnSnTe Hetero-junction Growth and Device Properties”, Science & Applications of Thin Films, Conference & Exhibition (SATF), Izmir (Turkey), 15-19 September 2014.
- “Fabrication and Characterization of Sputtered TiO<sub>2</sub> Thin Films”, 2014 MRS Fall Meeting & Exhibit (Boston, Massachusetts), November 30 - December 5, 2014
- “Fabrication and Characterization of TiO<sub>2</sub>/CdTe/ZnSnTe ETA Solar Cell”, Solar TR-3, Ankara (Türkiye), 27-29 May 2015.
- “Fabrication and Characterization of TiO<sub>2</sub>/CdTe/ZnSnTe ETA Solar Cell”, 31<sup>th</sup>. EU
- PV Solar Energy Conference and Exhibition, Hamburg (Germany), 14-18 September 2015.